MASS SELECTIVE LASER PHOTOIONISATION SPECTROSCOPY OF COPPER DIMER

By

Peter C. Cartwright

A Thesis presented for the Degree of Doctor of Philosopy
in the
Faculty of Science
at the
University of Edinburgh, 1989

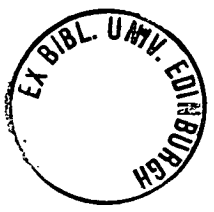

Abstract

An experimental apparatus for the study of naked transition metal clusters has been constructed, consisting of three differentially pumped chambers and a time-of-flight mass spectrometer. Clusters were generated using the technique of laser vaporisation of a solid target within the throat of a supersonic nozzle and were detected by mass-selective resonant two-photon ionisation. The factors affecting the resolution of the time-of-flight mass spectrometer used for mass-selective detection are considered and the experimental performance is compared to the predicted performance.

High resolution spectroscopy was performed on the A-X, B-X and C-X systems of Cu_2. Rotational constants were extracted for all three upper states. The uncertainty regarding the electronic symmetry of the A-state has been removed and it has conclusively been shown to be of $^1\Sigma_u^+$ (0_u^+) symmetry. The electronic symmetry of the C-state, $^1\Pi_u$ (1_u), and the rotational constants presented in this thesis have not previously been reported.

Collision-free lifetimes have been measured for selected vibrational levels of the A-, B- and C-states of Cu_2. The lifetimes were found to be in agreement with the literature values. An explanation of the electronic structure of Cu_2 is presented in the light of the results presented in this work and previous experimental and theoretical results.

Acknowledgements

There are many people who deserve my thanks and acknowledgements for their contribution to this work. Firstly, I must thank the SERC for the award of a postgraduate studentship and for their funding of the project. Moving away from the abstract, I also thank my supervisor, Dr Patrick Langridge-Smith, for his enthusiasm throughout the project, his great attention to detail and his seemingly never-ending supply of ideas.

Running these experiments alone was not easy and I was very fortunate to work alongside two people who made the experiments more manageable. I would like to thank Mr Andrew Butler for providing and maintaining the computer software that made the experiments feasible and Mr Andrew James for his great enthusiasm in the laboratory which made the experiments tolerable.

In the construction of the experimental apparatus, we had to draw on the skills of those employed in the departmental Mechanical and Electronic workshops. I would like to thank them for their work and their tolerance to the occasional late change in specification.

Latterly, I am also indebted to Dr Kenneth Lawley for his time and constructive comments on the interpretation of the experimental results.

I would also like to thank the people who have patiently supported and encouraged me during course of this work. I thank my parents for their generous and open support and I thank my wife, Cielo. Not only did she type the bulk of this thesis, her constant support, understanding and encouragement was a great inspiration when most needed.

DECLARATION

I declare that this thesis has been composed by me and that the work described in it is my own, except where due acknowledgement is made, and was carried out at the University of Edinburgh.

Signed :

Date : 25th October 1989.

To Cielo,

TABLE OF CONTENTS

LIST OF FIGURES

LIST OF TABLES

CHAPTER ONE

Introduction

Clusters have been described as entities containing between two or three atoms or molecules to up to several thousand [1]. As such they occupy a unique position amongst chemical structures, spanning the range from small isolated molecules towards the bulk phase.

Ligand-free transition metal clusters are a class in which there is a great deal of interest [1-4]. It is thought that they may provide models of processes such as catalysis and, more fundamentally, they offer the opportunity to study the chemical bonding and electronic structure of metals as they change from the molecular orbital description of small molecules to the band theory description of the bulk phase.

Until recently, however, both theoretical and experimental studies on transition metal clusters have been limited. They have been difficult to treat theoretically because the presence of d-electrons increases the number of electrons which must be considered in calculations. The d-electrons also introduce significant electron correlation and exchange effects, further complicating the calculations [3]. Experimentally, it has been difficult to generate sufficient quantities of clusters of (refractory) transition metals to permit experimental investigation. The last decade has seen a tremendous growth in studies on transition metal clusters due to the advent of new experimental techniques and theoretical methods, concurrent with better instrumentation and faster computers. The following section, 1.1, discusses the techniques by which clusters can be generated. Section 1.2 describes the techniques by which the previously generated clusters can be studied.

1.1 Techniques of Cluster Generation

1.1.1 Sputtering

This is a technique whereby a highly energetic beam of atoms or ions, generally of the noble gas group, is fired at a surface causing ablation. Even though sputtering produces mainly neutral clusters with only a small fraction charged [5], most of the work performed on clusters generated by this technique has been on ionic clusters. This is because sputtering produces translationally [6] and internally hot [7] clusters which are ejected with a wide angular distribution and it is much easier to contain and direct charged species than neutrals. The high, and generally unknown, temperature of the clusters precludes many of the experiments we wish to perform on clusters, such as the measurement of ionisation potentials and dissociation energies, and the study of the cluster reactivity or spectroscopy. The technique therefore remains best suited to the study of hot, or at best thermalised [8], cluster ions. In contrast to cluster ions, neutral clusters cannot be readily collimated, slowed down, thermalised nor mass or energy selected without first being ionised, an inefficient process on account of the high energy of ejection. The technique, therefore, has limited usefulness.

1.1.2 Ligand Stripping

Ligand stripping is a technique whereby a volatile derivative of a refractory metal is vaporised and then the ligands are removed leaving behind a bare metal core. The various methods used to remove the ligands include the use of metastable atoms, electron impact, multiphoton dissociation / ionisation and flash photolysis. The major attraction of the technique is the promise it holds in being able to produce clusters of a specific size by maintaining the metal framework of the precursor. Indeed, Leopold *et al* [9] have reported the generation of $FeRu^+$ from

$Fe_2Ru(CO)_{12}$ without any detectable generation of Fe_2^+ or Ru_2^+. The technique has been most successful in the generation of neutral and charged atomic and dimeric species [10][11] and with the exception of the report of Duncan *et al* [12], the technique does not generate bare metal clusters significantly larger than the number of metal atoms in the precursor. The maximum cluster size is therefore limited by available precursors. Another problem with the technique is the presence of the former ligands which can complicate the interpretation of results [12].

1.1.3 Direct Heating

In this technique, metal clusters are usually generated in an oven which they leave through a small nozzle. The technique is very successful for producing clusters of low boiling materials and clusters as large 500 atoms have readily been attained [13]. However, it has been less useful with refractory metals since, for example, even at a temperature of 4000 K, the vapour pressure of tungsten is still less than 1 torr. The design of an oven capable of vaporising refractory materials is critical because, at the high temperatures required, reactions between the oven materials and the charge can occur [14] and elaborate precautions must be taken to prevent metal vapour supersaturating and clogging the nozzle [15]. Clusters are also produced at approximately the same temperature as the oven and oven sources therefore produce a very convenient sample for emission studies. A substantial amount of spectroscopic data has been collected on metal dimers using ovens. The large number of lines from the hot sample permits extraction of accurate constants [16] but, on the other hand, can lead to spectral congestion and consequent misinterpretation [17]. Techniques exist to cool the clusters [18] but, unfortunately, cooling usually involves flow of an inert gas either through or near to the oven, which is therefore also cooled.

1.1.4 Laser Vaporisation

It is the technique of laser vaporisation, coupled to a supersonic molecular beam, that has largely been responsible for the recent growth in the number of experimental studies on transition metal clusters. This technique solves many of the problems associated with other techniques of cluster generation, namely, the difficulty vaporising refractory materials, the need for intense sources and the difficulty in obtaining cold, or at least cooled, clusters.

The species generated by laser vaporisation, like those from sputtering, suffer from high internal and translational temperatures [19]. However, as was first demonstrated by Smalley in 1981 [20], vaporising the metal within the throat of a supersonic nozzle quenched the plasma generated by the laser, promoted aggregation and clustering and, on expansion of the beam, cooled the clusters.

Other advantages of the technique are that the laser heating is localised on the target and it is not necessary to go to elaborate lengths to maintain the whole apparatus at a high temperature. Also, the laser vaporisation / molecular beam source produces non-equilibrium cluster distributions which are shifted in favour of larger clusters [21] and produces neutral, cationic and anionic clusters directly and in sufficient numbers that all can be studied.

The major disadvantages of the technique are firstly that it generates a distribution of clusters of different sizes over which there is only limited control and secondly, shot-to-shot reproducibility of the cluster intensity is quite poor due to instabilities in the lasers and molecular beams.

The technique has become universal and it is often the only way to prepare clusters of refractory materials.

1.2 Techniques for studying clusters

1.2.1 Matrix Isolation

Clusters trapped in inert gas matrices are only amenable to spectroscopic investigation. The major advantage of matrix isolation is its ability to keep clusters for a relatively long time, thus permitting study with less sensitive techniques than are required in the gas phase. For example, clusters have been studied by ESR [22] and Raman spectroscopies [23] in inert gas matrices. This is not possible in the gas phase due to the short lifetime of gas phase clusters.

The obvious objection to matrix isolation is that the clusters under study are not naked clusters but are species subjected to interactions with the host matrix. The interactions introduce perturbations and there have been reports where the ground state in the matrix is different than that in the gas phase [24]. Interactions with matrix phonons can also broaden spectral transitions and the presence of several different trapping sites can split the transitions, further complicating spectra. It is also not possible to obtain rotational spectra of matrix isolated clusters, with the resultant loss of the ability to measure accurate bondlengths and assign state symmetries.

The other major problem associated with studies of matrix isolated clusters is the difficulty encountered in assigning a spectral feature to a carrier. Assignment relies heavily on control experiments to estimate the clusters present in the matrix and to determine the effect of possible contaminants [22].

1.2.2 Gas Phase Studies

The major problems in studying the clusters in the gas phase are the low concentrations and the short timescale in which experiments must be performed. Detection of the clusters is limited to sensitive techniques such as laser-induced fluorescence (LIF) and ionisation. However, once these problems have been overcome, studies in the gas phase yield data on unperturbed clusters.

Through the use of mass-selective detection, signal can be unambiguously attributed to a particular carrier. Many studies have been performed using mass-selective photoionisation.

Through these new experimental techniques, several properties of clusters have been studied. Ionisation potentials [25][26], electron affinities [27] and magnetic moments [28] have all been measured as functions of cluster size. The photoelectron spectroscopy [29][30] and chemical reactivity [31][32] of clusters have also been studied as a function of cluster size. The results from all these studies suggest that the change in properties is not a smooth monotonic function of size.

Spectroscopic techniques offer the opportunity to directly study the electronic structure of the clusters. Many such studies have been performed on transition metal dimers [33][34] and a few on larger clusters [35]. These studies have illustrated the difficulties, due to perturbations and predissociations, associated with the electronic spectroscopy of species with dense manifolds of molecular states.

In this respect, a spectroscopic study of the group IB metal dimers, particularly Cu_2, should offer one of the least perturbed systems. The closed d-shell and large separation of atomic terms make it a focus for theoretical and experimental studies.

1.3 Experimental Objectives

There were two objectives to the work described in this thesis. Firstly, a molecular beam apparatus, based round the laser vaporisation / supersonic molecular beam cluster source with mass-selective photoionisation detection, was to be constructed with the capability to perform several types of experiments on transition metal clusters. This also involved the development of suitable software for the control of these complex experiments. Secondly, a study of the high resolution electronic spectroscopy of Cu_2 was seen as an ideal means of both testing the new apparatus and software whilst at the same time offering the opportunity to perform new studies on systems that were not particularly well characterised.

Chapter II describes the molecular beam apparatus, the laser vaporisation / supersonic molecular beam cluster source and the time-of-flight mass spectrometer used to achieve mass-selective detection. Also discussed are the laser systems, the electronic modules, the experimental techniques used and, briefly, how the computer controlled the experiments. More details on the latter can be found in reference [36].

Chapter III discusses time-of-flight mass spectrometry in more detail and describes the important factors affecting its resolution and transmission. Chapter IV presents the results of high resolution studies on the electronic spectroscopy of the A-X, B-X and C-X systems of Cu_2 performed using the technique of resonant two-photon ionisation (R2PI). Finally, chapter V discusses the electronic structure of the excited states of Cu_2 in the light of this work and previous experimental and theoretical studies.

REFERENCES

1. A.W. Castleman Jr. and R.G. Keesee, Ann. Rev. Phys. Chem., **37**, 525 (1986)

2. W. Weltner Jr. and R.J. Van Zee, Ann. Rev. Phys. Chem., **35**, 291 (1984)

3. M.D. Morse, Chem. Rev., **86**, 1049 (1986)

4. G.A. Ozin and S.A. Mitchell, Angew. Chem., **22**, 674 (1983)

5. P. Fayet, J.P. Wolf, and L. Woste, Phys. Rev. B, **33**, 6792 (1986)

6. T.R. Lundquist, J. Vac. Sci. Technol., **15**, 684 (1978)

7. W. Begemann, K.H. Meiwes-Broer, and H.O. Lutz, Phys. Rev. Lett., **56**, 2248, (1986)

8. L.H. Hanley, and S.L. Anderson, Chem. Phys. Lett., **122**, 410 (1985)

9. D.G. Leopold and V. Vaida, J. Am. Chem. Soc., **105**, 6809 (1983)

10. Yu.M. Efremov, A.N. Samoilava, V.B. Kozhurhovsky, and L.V. Gurvich, J. Mol. Spectrosc., **73**, 430 (1978)

11. D.G. Leopold and W.C. Lineberger, J. Chem. Phys., **85**, 51 (1986)

12. M.A. Duncan, T.G. Dietz, and R.E. Smalley, J. Am. Chem. Soc., **103**, 5245 (1981)

13. K. Saltler, J. Muhlbach, and E. Recknagel, Phys. Rev. Lett., **45**, 821 (1980)

14. D.S. Ginter, M.L. Ginter, and K.K. Innes, Astrophys. J., **139**, 365 (1964)

15. D.R. Preuss, S.A. Pace, and J.L. Gole, J. Chem. Phys., **71**, 3553 (1979)

16. N. Aslund, R.F. Barrow, W.G. Richards, and D.N. Travis, Ark. Fys., **30**, 171, (1965)

17. D.S. Pesic, and S. Weniger, Comptes. Rendus. Ser. B **273**, 602 (1971)

18. S.J. Riley, E.K. Parks, C.R. Mao, L.G. Pobo, and S. Wexler, J. Phys. Chem., **86**, 3911 (1982)

19. A.W. Ehler, J. Appl. Phys., **37**, 4962 (1966)

20. T.G. Dietz, M.A. Duncan, D.E. Powers, and R.E. Smalley, J. Chem. Phys., **74**, 6511 (1981)

21. L.A. Heimbrook, M. Rasaneu, and V.E. Bondybey, J. Phys. Chem., **91**, 2468 (1987)

22. R.J. Van Zee, R.F. Ferrante, K.J. Zerigue, W. Weltner, and D.W. Ewing, J. Chem. Phys., **88**, 3465 (1988)

23. M. Moskovits, D.P. DiLella, and W. Limm, J. Chem. Phys., **80**, 626 (1984)

24. W. Schrittenlacher, W. Schroeder, H.H. Rotermund, and D. M. Kolb, J. Phys. Lett., **109**, 7 (1984)

25. E.A. Rohlfing, D.M. Cox, A. Kaldor, and K.H.J. Johnson, J. Chem. Phys., **81**, 3846 (1984)

26. E.A. Rohlfing, D.M. Cox, and A. Kaldor, J. Phys. Chem., **88**, 4497 (1984)

27. L.S. Zheng, C.M. Karner, P.J. Brucat, S.M. Yang, C.L. Pettiette, M.J. Craycraft, and R.E. Smalley, J. Chem. Phys., **85**, 1681 (1986)

28. D.M. Cox, D.J. Trevor, R.L. Whetten, E.A. Rohlfing, and A. Kaldor, Phys. Rev. B, **32**, 7290 (1985)

29. D.G. Leopold, J. Ho, and W.C. Lineberger, J. Chem. Phys., **86**, 1715 (1987)

30. A.D. Sappey, J.E. Harrington, and J.C. Weisshaar, J. Chem. Phys., **88**, 5243 (1988)

31. S.C. Richtsmeier, E.K. Parks, K. Lim, L.G. Pobo, and S.J. Riley, J. Chem. Phys., **82**, 3659 (1985)

32. R.J. St. Pierre, and M.A. El-Sayed, J. Phys. Chem., **91**, 763 (1987)

33. S.J. Riley, E.K. Parks, L.G. Pobo, and S. Wexler, J. Chem. Phys., **79**, 2577 (1983)

34. P.R.R. Langridge-Smith, M.D. Morse, G.P. Hansen, and R.E. Smalley, J. Chem. Phys., **80**, 593 (1984)

35. E.A. Rohlfing and J.J. Valentini, Chem. Phys. Lett., **126**, 113 (1986)

36. A.M. Butler, Ph.D. Thesis, Edinburgh University (1989)

CHAPTER TWO

Experimental Apparatus and Techniques

2.1 Introduction

The previous chapter outlined the various methods used to generate clusters and the different techniques by which they can be studied. The experiments described in this thesis were all performed using a laser vaporisation / supersonic molecular beam source to generate the clusters and resonantly-enhanced or non-resonant laser photoionisation time-of-flight mass spectrometry for detection.

A schematic elevation and plan of the experimental apparatus are shown in Figures 2.1 and 2.2 respectively. Clusters were generated within the main (M-) chamber and were carried by the molecular beam to the A-chamber, which housed the time-of-flight mass spectrometer (TOFMS). Cluster generation required a high gas density to ensure there were sufficient collisions both to cool the plasma produced by the vaporisation laser and to ensure efficient nucleation [1]. It was therefore not uncommon to operate with more than 8 atmospheres backing pressure behind the nozzle and to reduce the demands placed on the pumping system, the nozzle was operated in a pulsed mode. The opposing constraints of high pressure for cluster generation and low pressure for collision-free detection in the TOFMS were satisfied by differentially pumping the M- and A-chambers and linking them only through the aperture of a small skimmer. Before describing the apparatus in more detail, it is instructive to give a flavour of the experiment. This is most easily done by describing an experimental cycle.

Figure 2.1 : Schematic elevation of the cluster apparatus

Abbreviations used in the figure :

RTM : Rod translation mechansism.
PGV : Pneumatic Gate Valves.
MBA : Molecular beam axis.
MCP : Microchannel plate detector.

Figure 2.1 : Schematic Elevation of the Experimental Apparatus

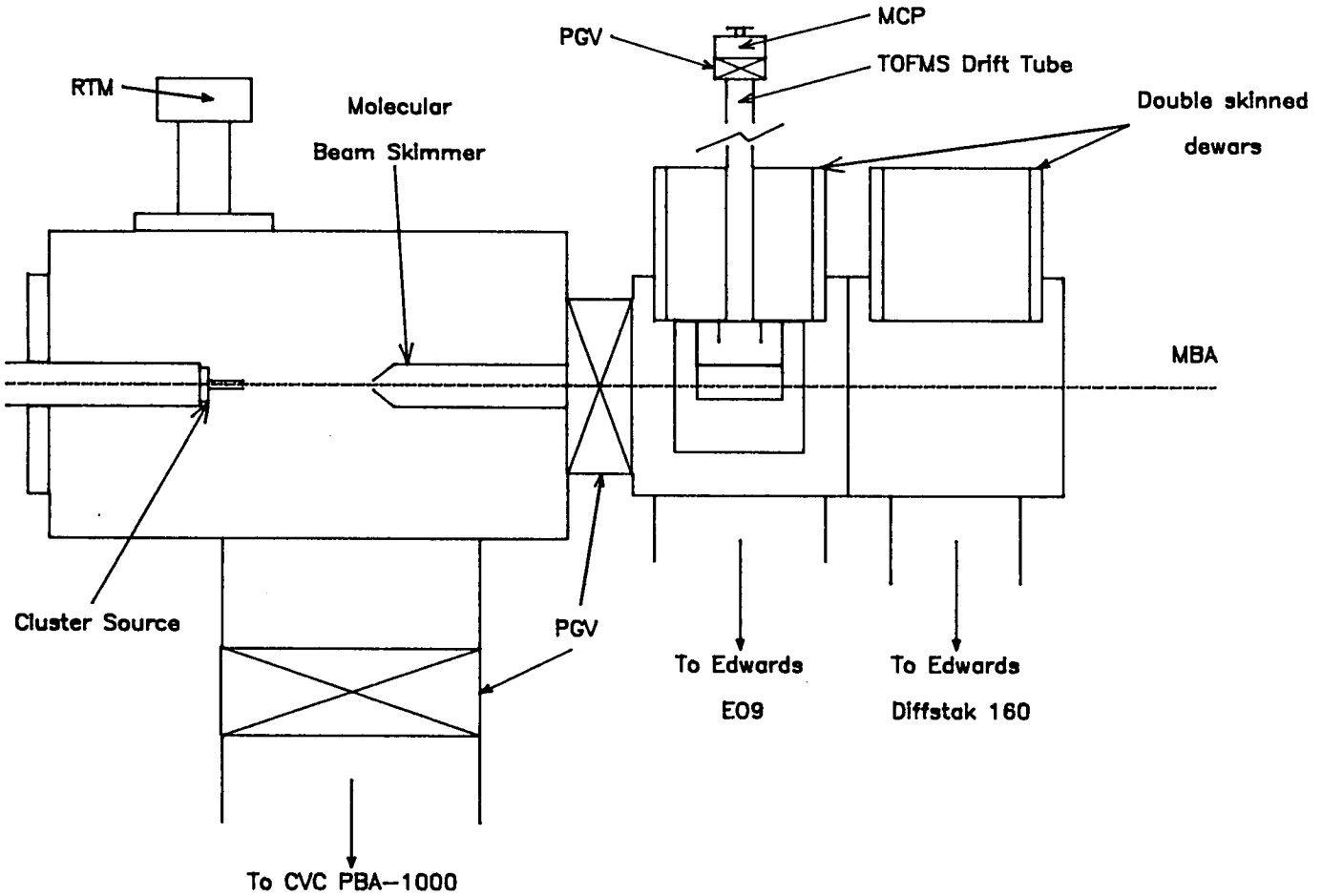

Figure 2.2 : Schematic plan of the experimental apparatus

Figure 2.2 : Schematic Plan View of the Experimental Apparatus

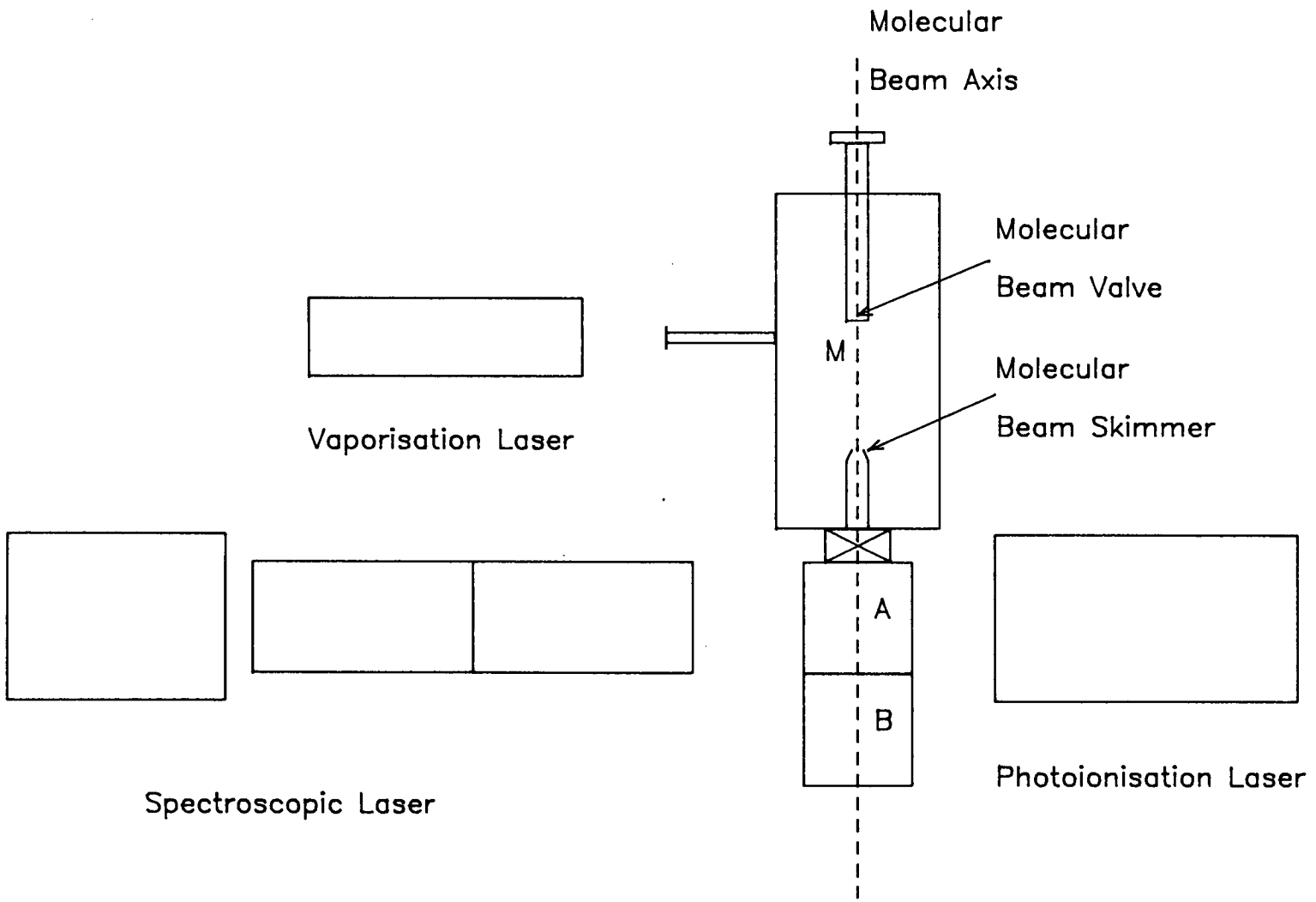

2.2 Experimental Cycle

The heart, or rather brain, of the experimental system was an IBM PC-AT computer. Through a CAMAC interface, it controlled the experiment and acquired the data. The computer performed these two tasks by running a program which toggled, at a rate of 20 Hz, between routines for controlling the experimental apparatus, known as the "tic" routines, and routines for storing and processing the data, known as the "toc" routines. The overall repetition rate for the experiments was therefore 10 Hz. The computer software was developed in-house and more details may be found in reference [2].

On a "tic", the computer sent data to the CAMAC crate to prime the transient digitiser and the two pulse generators. The pulse generators delivered pulses in the time sequence appropriate for the items of equipment in use. The first item of equipment triggered was the pulsed molecular beam valve. After an experimentally determined delay, the Nd:YAG laser used for vaporisation was triggered. This time delay was chosen empirically to maximise the number of clusters generated and, in practice, it meant that the Q-switch of the laser was triggered at the time the maximum gas density delivered by the molecular valve was above the target rod [3]. After another experimentally determined time delay to allow the plug of gas containing the clusters to traverse the distance between the nozzle and the ion extraction optics of the TOFMS, the interrogation lasers were triggered to photoionise the clusters.

The photoion signal was detected and amplified at the end of the TOFMS drift tube by a microchannel plate (MCP) detector. At an appropriate time, chosen to allow for the mass dependent ion flight times within the TOFMS, the transient digitiser received a stop pulse. It continued to digitise the signal from the MCP detector one last time before scanning was ceased. This completed the work of the

"tic" routines.

On a "toc", the data from the transient digitiser together with signals from monitor photodiodes acquired through an analogue-to-digital converter (ADC) unit were transferred to the computer. The computer was able to process the data until the next "tic" pulse when the experimental cycle was repeated.

All the experiments described in this thesis have been based around this cycle. A detailed description of the experimental apparatus is given in the following section which should be read in conjunction with Figures 2.1 and 2.2 .

2.3 Molecular Beam Apparatus

The whole vacuum system, with the exception of aluminium side flanges on the main-chamber, was constructed from 304 stainless steel. Vacuum sealing between flanges was achieved with viton O-rings. The apparatus consisted principally of three chambers, each pumped by independent, baffled diffusion pumps. Pressures in the main-chamber were measured by an Edwards Pirani gauge PRL 010 covering the range 10 to 10^{-4} mbar and an Edwards Penning gauge CP25-K for the range 10^{-2} to 10^{-7} mbar. In the A- and B-chambers, Balzers Pirani gauge TPR 010 (range 100 to 5.6×10^{-4} mbar) and Balzers cold cathode ionisation gauge IKR 020 (range 5×10^{-3} to 4×10^{-10} mbar) were used. The cold cathode ionisation gauges were factory calibrated for operation with nitrogen. A reasonable assumption was that the major background gases in the chambers were helium from the molecular beam and hydrogen liberated from the breakdown of the diffusion pump fluids. The pressures registered by the gauges therefore had to be corrected to give accurate pressure readings. Using the correction factors supplied with the gauges [4], the ultimate pressures obtained with no gas load in the M-, A- and B-chambers were 5.0×10^{-7} mbar, 5.0×10^{-8} mbar and 3.0×10^{-8} mbar respectively. Typically, during operation, these pressures rose to the values 2.0×10^{-4} mbar, 2.0×10^{-6} mbar and 1.0×10^{-6} mbar respectively. The pressure in the A-chamber was low enough to ensure that the ions formed in the extraction region of the TOFMS experienced collision-free conditions during their flight along the 1.32 m drift tube.

2.3.1 The Main Chamber

The main-chamber had a capacity of 68 l and was pumped by a 16" diameter diffusion pump (CVC PBA-1000) with an unbaffled pumping speed for air of 5300 l s^{-1} up to a pressure of 1 × 10^{-3} mbar. The diffusion pump was charged with Convoil-20 pump fluid and was baffled with a water-cooled, half-chevron, 12" diameter baffle, which reduced the pumping speed to 2690 l s^{-1}.

It is possible to estimate the molecular beam valve throughput from the equilibrium pressure in the chamber and the speed of the pump. The pressure was measured as 2 × 10^{-4} mbar and since the loss of gas through the skimmer was insignificant, the valve throughput can therefore be estimated as 0.53 mbar l s^{-1}.

The M-chamber had to handle high gas loads since its function was to couple a high pressure cluster source to a TOFMS, the latter device requiring as low a pressure as possible to prevent collisions within the drift tube. To cope with the high throughput , the diffusion pump was backed by a mechanical booster / rotary pump combination (Edwards EH250 / E2M40) capable of handling up to 8.5 mbar l s^{-1} at the typical foreline pressure of 0.1 mbar.

Since it was often necessary to work on equipment housed within the M-chamber, the ability to isolate this chamber from the A-chamber and from the the diffusion pump was essential. This was accomplished using pneumatic gate valves. The gate valves were interlocked to the pressure gauges in the A-chamber to prevent malfunctioning of the molecular beam valve choking the pumps or contaminating the microchannel plate detector.

The main chamber housed the cluster source and the molecular beam skimmer.

2.3.1.1 Cluster Source

Molecular Beam Valve

The molecular beam valve was mounted on an xyz-translator. Flexibility of movement was essential for the alignment of the molecular beam with respect to the skimmer and for the alignment of the vaporisation laser on to the target rod.

Two pulsed molecular beam valves were used during the course of this work , either an NRC BV-100 or a General Valves Series 9. Generation of clusters required a high density of buffer gas and both nozzles were designed for operation at high pressures.

The NRC BV-100 was a double solenoid pulsed valve with a soft iron actuator with a viton tip which sealed against a 0.5 mm diameter orifice. It followed the design reported by Adams *et al* [5]. One solenoid, the "close" coil, was used to hold the actuator firmly against the orifice sealing the nozzle. The second solenoid, the "open" coil, was used to pull the actuator away from the orifice, opening the valve and permitting gas flow. In normal operation, a continuous current flowed through the close coil until a trigger was received to open the valve. The current to the close coil was then removed and simultaneously an electrical pulse applied to the open coil. The width of this electrical pulse determined the stroke of the actuator and, approximately, the intensity of the gas pulse delivered. After a delay corresponding to the desired time duration of the gas pulse, a second, larger electrical pulse was sent to the close coil to shut the valve. In principle, the valve should have been able to deliver pulses from as short as 100 μs up to 1 ms in duration, the upper limit being set by the driver unit. In practice, seldom was successful operation achieved at high backing pressures with gas pulses shorter than 900 μs since, for settings shorter than this time, valve sealing became

extremely unreliable.

The General Valves Series 9 was a single solenoid pulsed valve with a teflon plunger sealing against a 0.5 mm diameter orifice. Sealing of the valve was achieved through a spring pushing the plunger against the orifice and the valve was opened by the application of an electrical pulse to the solenoid coil which attracted the soft iron actuator to which the teflon plunger was attached. The valve remained open for as long as the electrical pulse was supplied. Good operation depended on balancing the spring tension against the width of the electrical pulse sent to the solenoid for the backing pressure in use. In principle, the valve could deliver pulses from as short as 10 μs to pulses as long as one week. In practice, reliable operation was obtained for pulses as short as 200 - 250 μs (the upper limit was not tested !). Unfortunately, the gas throughput delivered by this valve was less than that from the NRC nozzle and, although it was more reliable, cluster generation was experimentally more difficult with this nozzle.

Cluster Source Faceplate

The purpose of the faceplate was to locate the target rod sufficiently close to the molecular beam axis so that the plasma generated by the laser beam striking the rod could be picked up by the molecular beam. It also constrained the buffer gas from free expansion until after it had passed the rod, ensuring a high gas density above the rod at the time of laser vaporisation.

Figures 2.3a and 2.3b show, respectively, an elevation and plan view of a typical cluster source faceplate. The target rod, molecular beam, and vaporisation laser beam were mutually perpendicular and three channels were drilled into the faceplate to accommodate them.

Figure 2.3 : Schematic plan and elevation of the cluster source faceplate. The scale is approximately 1:2.

Figure 2.3 : Schematic Plan and Elevation of the Cluster Source Faceplate

a) Elevation

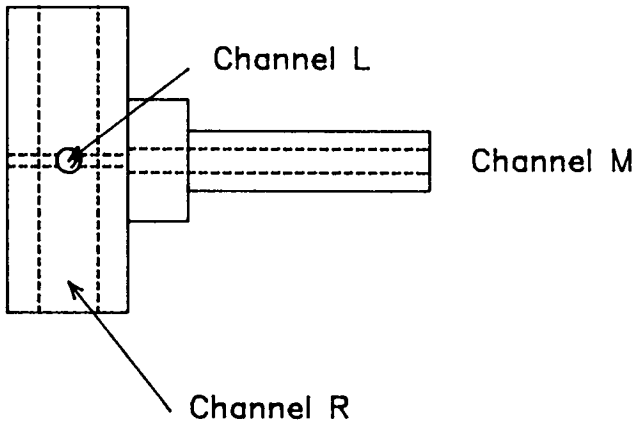

b) Plan

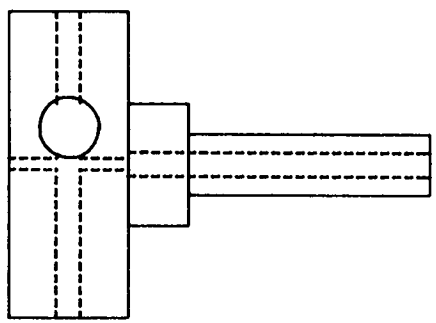

With reference to Figure 2.3, the target rods were located in channel R. The rods purchased were nominally 5 mm in diameter and were slightly oversized for the channel. They were turned down until they slip-fitted into the channel and were slack enough to permit free movement of the rod but tight enough to prevent the escape of a significant proportion of gas from around the rod.

Channel L allowed passage of the laser beam to the target rod. To reduce the amount of carrier gas escaping down this channel, it was desired to keep it as narrow as possible. On the other hand, to relax the severity of the constraints on the alignment between the vaporisation laser and the target rod, and to reduce the sensitivity of this alignment to vibration, it was desired to use as wide a channel as possible. A practical compromise was reached by using a 1 mm diameter channel with the General Valves molecular beam valve, and a 2 mm diameter channel with the more powerful NRC molecular beam valve.

Channel M, orthogonal to channels R and L, was located over the valve orifice. By constraining the gas within the channel, a sufficiently high density of gas was guaranteed above the rod to quench the plasma generated by laser vaporisation and to promote clustering. The channel diameter on the valve side of the target rod matched the valve orifice but after the target rod it increased to approximately 1 mm.

To further increase the number of collisions occurring, and hence the degree of clustering, a variable length extender channel, E, was located at the end of channel M [6]. The diameter of the extender channel was approximately 2 mm and the length used varied between 8 - 50 mm, depending on the propensity of the target element to cluster and the cluster size distribution required. For most of the spectroscopic work on copper dimer, an extender channel length of 33 mm was found to be satisfactory.

Rod Translation Mechanism

Above the faceplate, and mounted on an xy-translator, was a mechanical vacuum feedthrough which allowed continuous translation and rotation of the rod via a stepper motor driven screw mechanism (McLennan 34 HS-106 motor driving a 8-32 UNF rod). Exposure of fresh target surface to the vaporisation laser greatly enhanced the stability of cluster generation. This is illustrated in Figure 2.4.

Figure 2.4 shows the spectrum obtained by scanning the trigger to the Q-switch of the Nd:YAG vaporisation laser with respect to the nozzle trigger, that is vaporising the rod into different parts of the helium carrier gas pulse. The copper target rod was rotated at 1 Hz. It is readily seen that the cluster signal generated increases markedly on every tenth shot of the laser, corresponding the movement of the target rod. The cause of the drop in intensity if the rod is not moved is thought to be due to the laser digging a pit in the target rod from which the plasma has difficulty escaping [7].

2.3.1.2 Molecular Beam Skimmer

Also housed in the M-chamber was a molecular beam skimmer (Beam Dynamics, 3 mm diameter, 50° included angle) which for the gas loads used (0.53 mbar l s^{-1}), maintained a pressure differential of approximately 100 between the M- and A-chambers. The skimmer was mounted off the end wall of the M-chamber to reduce the disturbance to the molecular beam caused by skimmed gas reflected back from the wall [8].

Figure 2.4 : Illustration of the importance of rotating the target rod. The spectrum was taken by altering the time delay between triggering the molecular beam valve and triggering the vaporisation laser Q-switch. The target rod was rotated at 1 Hz and the sharp peaks in intensity correspond to movement of the target rod. The underlying background in the spectrum maps the dependence of the cluster intensity on the position within the carrier gas pulse at which vaporisation occurred.

Figure 2.4 : Movement of the target rod at 1 Hz

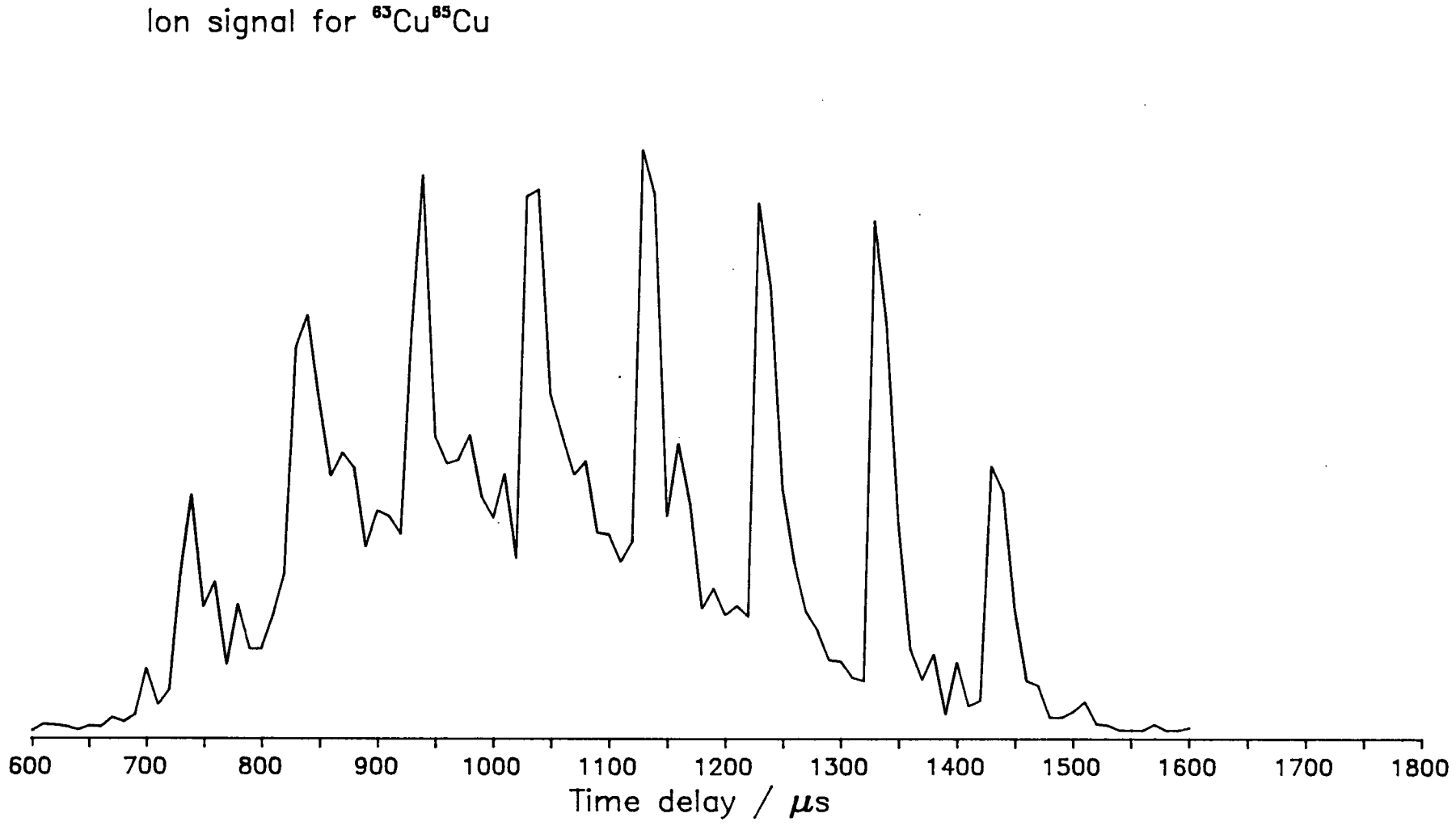

2.3.2 A-Chamber

The A-chamber was a 17 l stainless steel cube pumped by an Edwards EO9 diffusion pump equipped with a water cooled, full chevron baffle. The unbaffled pumping speed on hydrogen was quoted as 3300 l s^{-1}. The pump foreline was connected to that of the diffusion pump on the B-chamber and the pumps were backed by a combination of two rotary pumps (Edwards E2M18) connected in parallel. This chamber was the part of the apparatus where the clusters were investigated and for this purpose, it was equipped with two 50 mm diameter Spectrosil-B windows, one on each side flange, to permit the passage of the counter propagating interrogation lasers.

The drift tube of the TOFMS was mounted on the top flange of the chamber. It was 1.32 m long with an internal diameter of 40 mm. The MCP detector was located at the top of the drift tube, separated from the main vacuum system by a pneumatic gate valve. The lower 66 cm of the drift tube was surrounded by a liquid nitrogen dewar, the bottom of which penetrated into the vacuum chamber to a depth of 2.5 inches. The ion extraction optics were supported from the bottom of the dewar and were surrounded by a copper box which was in good thermal contact with the dewar and which was completely closed except for four 40 mm diameter apertures, one on each side, to permit the passage of the molecular beam and the interrogation laser beams. The cryopumping was effective in reducing the base pressure within the A-chamber by an order of magnitude.

2.3.2.1 TOFMS Ion Extraction Optics

A diagram of the ion extraction optics for the TOFMS is shown in Figure 2.5. The design followed that first described by Wiley and McLaren in 1955 [9] and consisted of two electric fields defined, in Figure 2.5, by grids R and D, and by D

and F, respectively, followed by a field-free drift tube. Due to the perpendicular orientation of the molecular beam and drift tube axes, electrical deflection plates had to be placed above grid F to counteract the velocity in the direction of the molecular beam acquired by the clusters during supersonic expansion. The ion extraction optics were built in-house. All the plates, with the exception of the deflection plates, were constructed from 0.5 mm thick stainless steel sheet and were 72 mm square. The deflection plates were constructed from aluminium and were 0.25" thick. The repeller plate was complete but the draw-out plate and the flight-tube plate were punctured axially by holes 40 mm in diameter to permit the passage of the ions. To prevent excessive field penetration, both apertures were covered by 90 % transmitting nickel mesh (Buckbee-Mears), which was tagged on to the plates using electrically conducting silver paint. The plates were held apart using Delrin spacers. Relevant dimensions are given in the legend to Figure 2.5.

A small tag was spot welded on to each of the plates to enable electrical connections to be made. The voltage to the repeller plate (3,015 V) was supplied by a CAMAC based LeCroy 2415 power supply. The voltages to the draw-out grid (2,555 V) and the deflection plates (0 - 650 V) were provided by Power Designs Model 1570 and 2K20A power supplies, respectively.

2.3.3 B-chamber

This chamber was similar to the A-chamber except that the liquid nitrogen dewar mounted on the top flange did not contain a drift tube and pumping was provided by an Edwards Diffstak 160 / 700C, with a pumping speed of 1300 l s^{-1} on hydrogen. For all of the experiments described in this work, the B-chamber was used merely as a dump chamber for the molecular beam.

Figure 2.5 : Schematic elevation of the TOFMS ion extraction optics. The separation between the repeller plate, R, and the draw-out grid, D, was 32 mm. The separation between the draw-out grid and the flight-grid, F, was 6 mm. The deflection plates were located 17 mm above the flight grid, were 19 mm long, and were separated by 38 mm.

Figure 2.5 : Schematic Elevation of the TOFMS Ion Extraction Optics

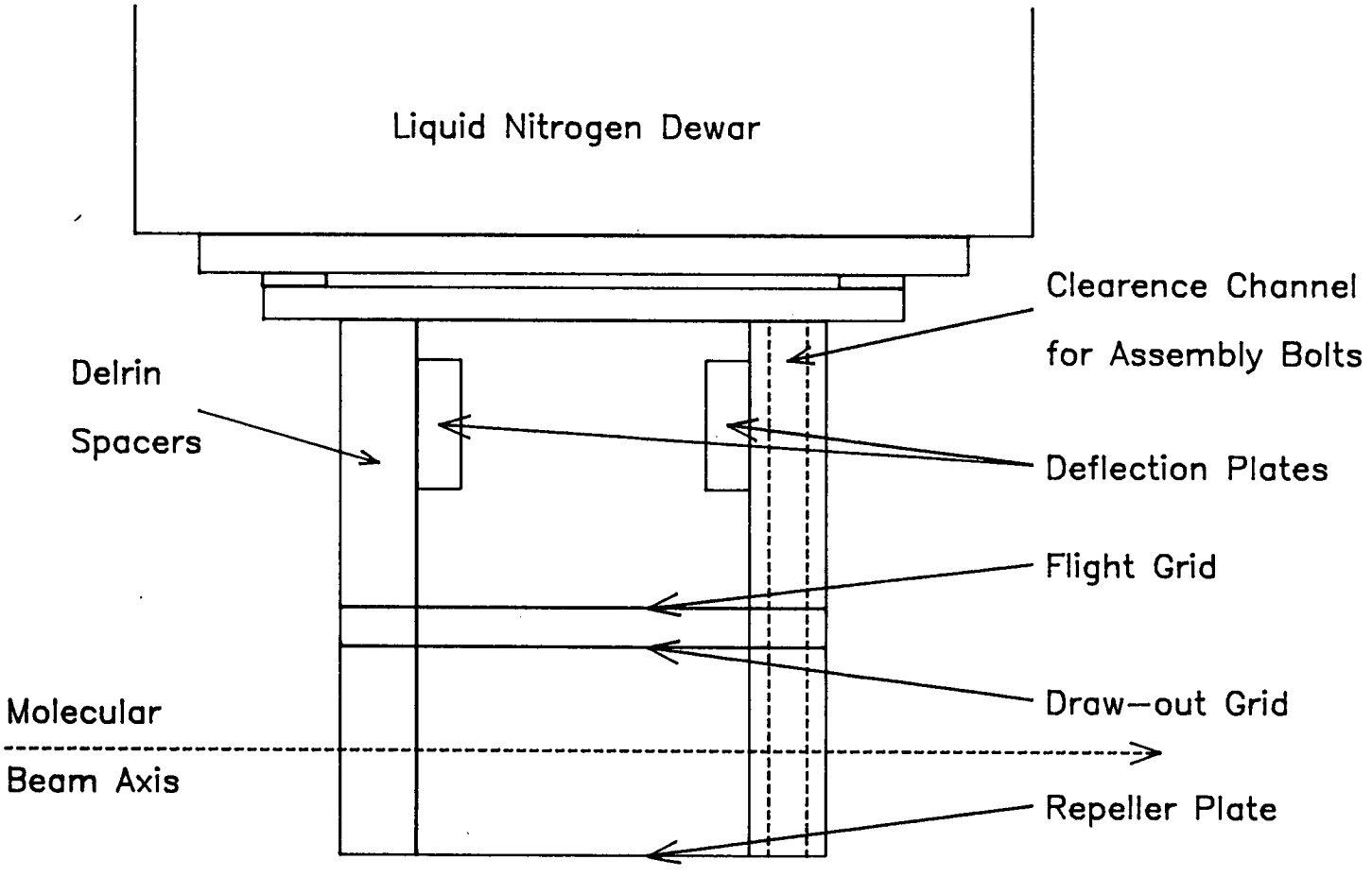

2.4 Laser Systems

The experiments described in this thesis routinely required the use of three laser systems and always required a minimum of two. The tasks required of the laser systems were to vaporise the metal target rod and to photoionise the clusters either resonantly or non-resonantly (See Section 2.7). Non-resonant photoionisation used only one laser, whereas resonantly-enhanced photoionisation generally required two lasers. The first was a tunable dye laser and the second, if required, was a fixed frequency laser. There were four laser systems available in the laboratory.

2.4.1 HyperYAG HY750

The HY750 was an oscillator-amplifier Nd:YAG laser capable of delivering 800 mJ per pulse at its fundamental wavelength of 1064 nm. It was designed to operate at a repetition rate of 10 Hz and it was equipped with crystals for generation of both the second and third harmonics of the fundamental wavelength (crystals CD*A and KD*P). Specified, and achieved, output energies for the second and third harmonics were 320 and 170 mJ per pulse, respectively. The three harmonics could be spatially separated by passing them through a prism harmonic separator assembly. Both Q-switched and fixed-Q output could be produced.

External control of this laser required two trigger pulses. The first pulse triggered the flashlamps and the second pulse, delayed by approximately 180 μs from the first pulse, triggered the Q-switch.

The laser was used to vaporise the target rod and was operated on its second harmonic at 532 nm. The energy needed for optimum vaporisation of a target rod depended on the material and was in the range 20 - 50 mJ per pulse. The second harmonic output was focused on to the target rod with a 1 m focal length lens to

a spot roughly 0.5 mm in diameter, yielding power densities on the order of 2 - 5 $\times 10^8$ Wcm^{-2}.

2.4.2 Quanta-Ray System

The Quanta-Ray laser system consisted of a DCR-2A Nd:YAG laser, a PDL-2 dye laser and a unit for extending the wavelength range of the dye laser through frequency doubling and mixing, the WEX-1c.

The DCR-2A had similar specifications to the JK HY750. It was capable of delivering 800 mJ per pulse at 1064 nm at a repetition rate of 10 Hz. It was also equipped with crystals for second and third harmonic generation (KD*P), had a prism harmonic separator assembly, the PHS-1, for spatially separating the three harmonics and it could also deliver Q-switched and fixed-Q output.

The PDL-2 dye laser was designed to be pumped by the DCR-2A Nd:YAG laser. It consisted of an oscillator, an optional preamplifier and an amplifier which could be pumped either longitudinally or transversely. The laser was also fitted with an optional delay line which introduced a 2.5 ns delay between the oscillator pump pulse and that of the preamplifier and amplifier. The function of the delay line was to reduce the amount of amplified spontaneous emission (ASE) produced and was used when pumping low gain dyes. Movement of the dye laser grating was controlled by the IBM PC-AT via a stepper motor driver unit.

The WEX-1c extended the tuning range of the PDL-2 into the ultraviolet, covering the range 432 - 217 nm. The unit consisted of two modules containing crystals. The first set of crystals covered the wavelength range 432 - 259 nm by either mixing the fundamental output of the Nd:YAG laser with the fundamental dye output or by frequency doubling the dye laser output. The second set of crystals mixed the frequency doubled dye laser output with the Nd:YAG fundamental

wavelength to cover the range 265 - 217 nm.

Correct angle tuning of the crystals as the dye laser wavelength was scanned was maintained by constant monitoring of the output beam profile by a biphotodiode linked to servo-motors. Any asymmetry in the profile of the doubled (mixed) output beam was detected by the biphotodiode and compensated for by angle tuning. A prerequisite for reliable operation was the attainment of a good dye laser beam profile. Unfortunately, this was not trivial when the amplifier was transversely pumped.

External control of this laser system was quite complex and required a modification to the laser trigger circuit board. Three trigger pulses were required to operate the Nd:YAG laser and a further pulse was required if the WEX-1c module was used. The first pulse to the Nd:YAG laser activated the relays to the Q-switch high-voltage supply. Approximately 3 ms later, a second pulse triggered the flashlamps. Between 140 - 210 μs later, a third pulse triggered the Q-switch releasing the laser output. The actual time delay between the second and third pulses was adjusted to control the energy of the laser output. A fourth pulse, simultaneous with the third pulse, was used to refresh the logic circuits of the photodiodes in the WEX-1c unit, if it was in use.

The Quanta Ray laser system was very versatile and had a variety of uses. Tunable radiation from the dye laser was used for low resolution spectroscopic investigations of metal species as, for example, with the Nb and NbO spectra shown in Figure 2.8. If the second harmonic from the Nd:YAG laser was not required for pumping the dye laser, then it could be frequency doubled in the WEX-1c unit to provide an alternative lower energy photon to the ArF photon for photionisation of the clusters. This was required for the spectroscopic investigation on species with ionisation potentials below the 6.4 eV energy of the ArF photon.

For example, studies on Mo_2 were performed using the 266 nm photon for photoionisation. Finally, the Nd:YAG laser was sometimes used alone as an alternative to the JK HY750 laser for cluster generation. When used in this mode, it was operated to produce identical output to the JK laser.

2.4.3 Lumonics TE-861T-4

The TE-861T-4 excimer laser was capable of operating on both chloride and fluoride gas mixes, but was passivated for the latter. It was always operated on an argon fluoride mix producing radiation at 193 nm. It was capable of producing approximately 100 mJ per pulse at 10 Hz with a specified pulse duration of 8 - 10 ns full-width-half-maximum (FWHM) [10].

The laser was operated in a "charge-on-demand" mode. In this mode, two trigger pulses were required. The first pulse activated the circuit for charging the capacitor banks and had to be delivered approximately 12 ms before the second trigger pulse. The second pulse triggered the thyratron, generating the laser output.

2.4.4 Lambda Physik System

The Lambda Physik system consisted of an EMG 201 MSC excimer laser, operating on a xenon chloride gas mix lasing at 308 nm, which pumped a FL3002EC dye laser. The excimer was able to deliver 400 mJ per pulse at 1 Hz. The excimer energy used at 10 Hz was typically 200 mJ $pulse^{-1}$.

The FL3002EC dye laser consisted of an oscillator / preamplifier cuvette followed by two further stages of amplification. The pump beam was appropriately delayed between each stage of amplification to reduce ASE. The dye laser could also be fitted with an intracavity etalon to produce line-narrowed output (the laser spectral bandwidth was reduced from 0.4 cm^{-1} to less than 0.04 cm^{-1}) and with a range of frequency doubling crystals to extend the laser output into the ultraviolet. Initial alignment and calibration of both the intracavity etalon and the frequency doubling crystals was required. However, tracking of both the etalon and the crystal as the dye laser grating was scanned was performed automatically by an inbuilt microprocessor.

Control of the timing of this laser system required one pulse to trigger the excimer laser. A further trigger pulse was required by the microprocessor in the dye laser to initiate movement of the etalon and / or grating.

The Lambda Physik system was used exclusively for spectroscopic investigations of the metal dimers. Due to the small rotational constants of the transition metal dimers, all work at rotational resolution had to be performed with this system and using the intracavity etalon.

2.5 Data Acquisition and Control Electronics

The electronic modules were mounted in either a CAMAC crate (WES) or in a NIM bin. The CAMAC modules were interfaced to the computer through a crate controller (DSP 6002) and an IBM interface card (DSP PC004). The NIM modules were not interfaced to the computer and the function of the bin was solely to provide the necessary power rails.

The modules either controlled the experiment or acquired data. The first group consisted of two pulse generators (Kinetic Systems 3655 and LeCroy 4222), the digital-to-analogue converter (DAC) unit (BiRa 5408DAC) and the stepper motor controller (Hytec SMC 1604). The second group consisted of the transient digitiser (DSP 2001) and the ADC unit (BiRa 5303ADC).

2.5.1 Control Modules

These units were essentially triggering devices for firing the pulsed molecular beam valve and the lasers. They were also used to control the movement of the dye laser grating and the target rod.

2.5.1.1 Kinetic Systems 3655 Pulse Generator

This was an eight channel pulse generator capable of delivering 200 ns wide TTL pulses with microsecond accuracy. Each channel had its own 16 bit register to store the set time delay for the pulse with respect to an external trigger pulse. The module compared a counter with the registers sequentially and for correct operation, each successive channel had to be programmed with a larger time delay than the previous one. This meant that two channels could not be triggered simultaneously and the channels had to be used sequentially with at least 1 μs between adjacent channels.

The pulses provided by the device were too narrow to trigger the external systems and were sent to a NIM based line driver module which lengthened the pulses and boosted their power.

2.5.1.2 LeCroy 4222 Pulse Generator

This was a four channel pulse generator with sub-nanosecond accuracy which could be programmed to nanosecond precision. Pulses from this module were used to trigger devices for which timing was critical. For example, in spectroscopic experiments (See Section 2.6.3) both lasers were triggered from this device.

Each channel had its own 24 bit register, in which was stored the time delay, and a 21 bit counter. On receiving a trigger pulse, the counters were loaded with the 21 most significant bits from the registers and were then decremented at 125 MHz (every 8 ns). Nanosecond accuracy of the output was obtained by feeding the three least significant bits from the register into a digital-to-analogue converter which in turn generated a threshold level for a fast ECL comparator. The channels were independent and could be used in any order or even simultaneously. The pulses had sharp rising edges, risetime faster than 1 ns, and suffered from a jitter of less than 600 ps for delays as long as 10 ms. The pulses were also too narrow to trigger the external devices (100 ns, 5 V into 50 Ω) and had to be sent via the line driver box.

In operation the unit had to be "enabled" to receive a trigger pulse and it had to be triggered. It was enabled on each "tic" by the computer and triggered from one of the channels of the KS-3655.

2.5.1.3 Line Driver Box

This was a custom-built unit, based around the dual monostable multivibrator chip, the 74221, and its function was to take the narrow pulses from the pulse generators, lengthen them and increase their power. The unit was capable of delivering outputs at either 5 or 15 V. It was housed in the NIM bin.

The unit had twelve input channels and each channel could output either a 10 μs long 5 V pulse or a 50 μs long 15 V pulse (switch selectable). The input was fed into one of two parallel circuits depending on which output pulse was required. For 5 V output, the input was directed to a 74221 chip with the appropriate external resistor and capacitor (15 KΩ and 0.001 μF, respectively) to generate a pulse of width 10 μs. This 10 μs pulse was sent to a 7417 driver chip to provide a 10 μs wide 5 V pulse powerful enough to drive a 50 Ω load. The 50 μs wide pulse (3.3 KΩ external resistor and 0.023 μF capacitor) was sent to a CMOS 40107 driver to provide a 50 μs wide 15 V pulse capable of driving 50 Ω.

2.5.1.4 Hytec SMC 1604 Stepper Motor Controller

This CAMAC based stepper motor controller was capable of controlling up to four independent stepper motors. It was used to control the stepper motor which translated and rotated the target rod (McLennan 34 HS-106) and the motor which stepped the grating on the PDL-2 dye laser.

The SMC 1604 was programmed to deliver single step commands at a speed of 50 steps per second. For control of the movement of the target rod, one such command was issued on each "tic". Control of the PDL-2 grating was a little more complicated. As described in Section 2.6.3, spectroscopic experiments involved running "N" experimental cycles at a particular wavelength and commands had only to be issued on every "N^{th} tic". Thus, on each "N^{th} tic" the SMC 1604

delivered "p" single step commands to the grating, where "p" was the number of single steps required to move the grating by the desired wavelength step. Scanning of the PDL-2 grating was under full computer control.

Each channel from the SMC 1604 was linked to one of four McLennan TM162C driver cards which were mounted in a standard 19" rack unit. The driver cards were designed to drive up to 2 A per phase (more than adequate for the motors in use) and could produce either full- or half-steps (1.8° or 0.9°).

2.5.1.5 BiRa 5408 Digital-to-Analogue Converter (DAC)

This was an eight channel DAC able to deliver 5 mA at between 0 and 10 V. Each channel had a 12 bit register and hence a resolution of 2.5 mV in the output voltage. The voltage required less than 4 μs to settle. In the present work, the function of the DAC was merely to provide an external trigger pulse to the grating on the FL3002EC dye laser. Unlike the PDL-2 laser which was only provided with a stepper motor on the grating, the FL3002EC had its own microprocessor for controlling the direction of motion, step-size, and speed of the stepper motors used to drive the grating and etalon. Since the microprocessor was also responsible for the synchronised tracking of the intracavity etalon and the grating, it was felt best to leave the package alone. The only external input required by the microprocessor was a trigger pulse and this was provided by the DAC every "N^{th} tic". The reason for using the DAC rather than a pulse from one of the pulse generators was that the pulse generators produced pulses on every "tic" whereas the spectroscopic experiments (See Section 2.6.3) required a pulse on only every "N^{th} tic". It was technically simpler to program the DAC to do this than to send a pulse from the pulse generator to a counter which would only transmit every N^{th} pulse.

2.5.2 Data Acquisition Modules

The data acquisition units converted the analogue voltage outputs of the various detectors into digital form for subsequent processing by the IBM PC-AT. The essential unit for any of the experiments was the DSP 2001 transient digitiser.

2.5.2.1 DSP 2001 Transient Digitiser

The DSP 2001 was a 100 MHz transient digitiser with 8 bit resolution and 32 K of memory. It could digitise signals from 0 to -512 mV and was used to record the output voltage waveform from the microchannel plate detector.

The DSP 2001 could sample at a selection of frequencies (from 100 MHz down to 1 MHz) and only a fraction of its memory could be used if desired. The fraction of memory used could be further divided into "pre-trigger" and "post-trigger" samples, as described below.

The mode of operation was straightforward. The module received a "start-scanning" signal from the computer initiating digitisation at the selected frequency. When all of the fraction of memory in use had been written to, the digitiser started to overwrite the memory with new samples. Overwriting started with the oldest datum and continued until a stop trigger was received. Experimentally, this stop pulse was usually synchronised to the trigger pulse to the laser used to photoionise the clusters. On receipt of the stop pulse, the digitiser continued to sample until it had overwritten the fraction of memory selected as post-trigger samples (experimentally this was mostly 1). The digitiser memory thus contained the pre-trigger fraction of samples taken before the stop-pulse, providing a baseline, if required, and the post-trigger fraction taken afterwards.

After a short settling time (1.2 μs), the data from the memory was available for

transfer across to the computer. Transfer occurred via the direct-memory access (DMA) chip. Due to the limiting speed of data transmission through the CAMAC data bus, all the experiments used only 2 K of memory from the transient digitiser.

To circumvent the limited time range that could be stored in 2 K of data sampled at 100 MHz (a range of 20 μs), two approaches were adopted. Firstly, if a total mass spectrum was required and it extended over a greater range than 20 μs, the simple solution was to reduce the sampling frequency to 50, 20 or, occasionally, 10 MHz. This degraded the observed time resolution of the signal. However, if it was desired to retain the highest resolution for a cluster with a flight time longer than 20 μs, then the stop pulse was delayed with respect to the trigger to the laser used to photoionise the clusters. The stop pulse was always provided by one of the channels from the LeCroy 4222 for accuracy.

2.5.2.2 Pacific Instruments Video Amplifier 2A50

The signal to the digitiser did not come directly from the microchannel plate detector but via a direct-coupled non-inverting amplifier with a gain of approximately 100. Both input and output impedances were 50 Ω, ideally suited for linking the 50 Ω anode of the microchannel plate detector to the 50 Ω input of the transient digitiser. The amplifier operated at a constant gain to about 150 MHz. The amplifier was mounted directly above the microchannel detector and hence the signal was amplified before picking up any noise along the cable linking the detector to the digitiser.

2.5.2.3 Microchannel Plate Detector (R.M. Jordan)

Although not an electronic module, the microchannel plate detector was so intimately involved with the electronics of data acquisition that it is now discussed. The microchannel plate (MCP) detector was of a dual chevron design [11] using two Galileo MCP-18B plates, which had an active diameter of 18 mm. Each plate had a gain of 1000 when biased by 1 kV, resulting in a total gain of 10^6.

There are two ways of coupling a MCP detector to observe ions [11]. Firstly, the front plate can be grounded and the anode held at a high positive potential. This method does not interfere with the ion flight times since the earthed front plate defines the end of the field-free drift tube. The major disadvantage of this coupling is that signal from the anode must be capacitively coupled to remove the large positive bias. The other way of coupling the MCP involves applying a large negative potential to the front plate and holding the anode at earth potential. To prevent the potential of the front plate from penetrating into the supposedly field-free drift tube and perturbing the flight times, an earthed grid must be placed in front of the plate with a consequent reduction in ion transmission. The presence of the large negative potential on the front plate also precludes the detection of negative ions. However, this form of coupling means that the anode can be directly linked to other equipment (i.e. amplifier and digitiser) and it has an unexpected bonus for the detection of positive ions in that the presence of approximately -2 kV on the front plate accelerates the positive ions which results in a greater gain at the MCP (the gain increases with ion impact energy) [12].

The R.M. Jordan MCP used the second coupling scheme and had an 82 % transmitting grounded grid in front of the first microchannel plate. The grounded anode was impedance matched for 50 Ω.

2.5.2.4 BiRa 5303 ADC

The ADC was used to convert signals from monitor photodiodes for storage in the computer.

The 5303 ADC has 16 bipolar channels each with 12 bit resolution. All the channels may be accessed sequentially or randomly, or one channel may be repetitively sampled. This latter mode of operation was used in the present work.

The unit was set-up to convert voltages between 0 and +5 V. In operation, the signal from a photodiode monitoring, for example, etalon fringes was sent to a gated integrator (Stanford Research Systems SR 250). The averaged output from the gated integrator was then digitised by the ADC.

As mentioned previously, all the experiments performed on the apparatus used the experimental cycle described in Section 2.2. Three different types of experiment were performed and they are described in the following section.

2.6 Modes of Operation

2.6.1 Acquisition of Mass Spectra

This was the most basic experiment and was an essential preliminary to more detailed experiments. The mass spectra were used to analyse the cluster species present in the molecular beam, to aid optimisation of the generation of the desired cluster range and to measure the relative intensity and stability of cluster generation on a day-to-day basis. Only when cluster intensity and shot-to-shot stability were satisfactory was it worthwhile to attempt more complex experiments.

In these experiments, referred to as "mass scans", all of the clusters of various sizes were photoionised in the extraction region of the TOFMS, usually with the 6.4 eV photon from the ArF excimer laser. The experimental cycle was repeated "N" times and at the end of each cycle, 2 K channels of digitiser memory were transferred to the computer to form a cumulative sum of photoion signal intensity against transient digitiser channel number. The value of "N" was programmable and was chosen to give an acceptable signal-to-noise ratio. From the known scan rate of the transient digitiser, the channel number could be related to the flight time of the ions and the mass spectrum was displayed as photoion intensity against time.

Figure 2.6 illustrates the generality of the laser vaporisation technique to produce clusters of a variety of materials with a wide range of boiling points. Clusters could be readily generated from copper (boiling point 2868 K) up to molybdenum (boiling point 5800 K).

Figure 2.6 : Mass spectra for nickel, iron and molybdenum clusters. All three spectra were acquired using the second harmonic from the Nd:YAG laser to generate the clusters and 193 nm ArF excimer laser output for photoionisation.

Figure 2.6 : Mass Scans

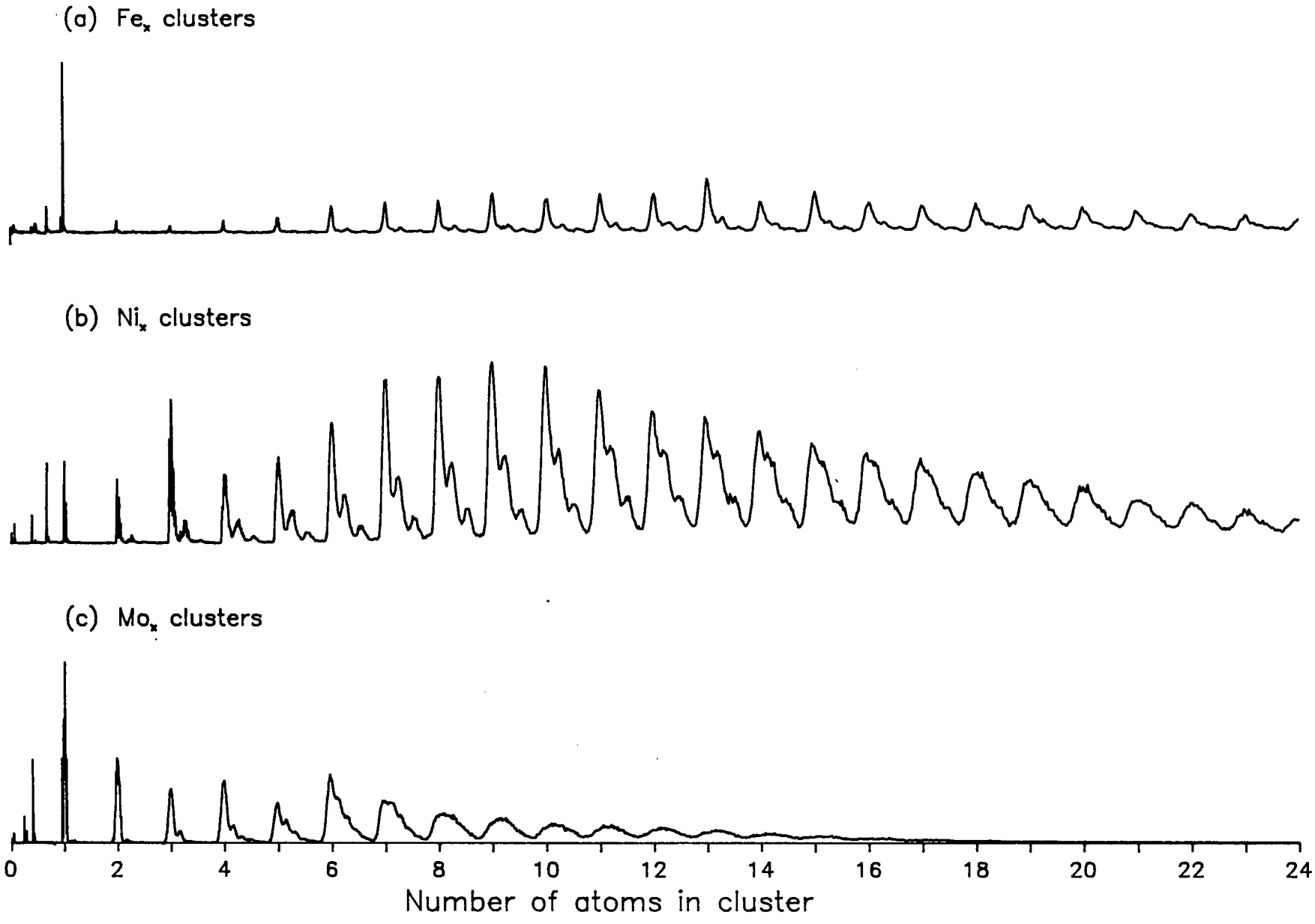

2.6.2 Acquisition of Timing Data

These experiments are referred to as "time scans". They depended for their success on the ability to monitor selectively the signal of interest as a function of the time delay between two events, such as the time delay between triggering the vaporisation laser and triggering the photoionisation laser. Selectivity was achieved by monitoring only those channels on the transient digitiser which held the mass resolved signal of the species under study. These channels are referred to as "mass channels".

The computer was programmed with a start-time, a stop-time and a step size for scanning. The programmed time delay in the selected channel of the pulse generator, the scanned channel, was set to the start-time. An experimental cycle was then run and the data from the mass channels was stored in the computer. The computer then incremented the time in the scanned channel by the step size and another experimental cycle was run. The data from the digitiser mass channels was transferred to the next array element in the computer. The time-increment / experimental cycle / store-in-next-element sequence was continued until the time in the scanned channel had reached the stop-time. At this point, the programmed time delay in the scanned channel was reset to the start-time and the whole cycle was repeated, storing the averaged signal for successive timings in successive array elements. Repetition of this cycle enabled an averaged spectrum of photoion intensity against trigger delay time to be acquired for an arbitrary number of samples.

Any channel of the pulse generators could be scanned and optimisation of the production and detection of the clusters required scanning of the triggers to the vaporisation and photoionisation lasers, respectively. It was also possible to measure the lifetimes of electronically excited states of selected cluster species in

this mode by time resolved resonant two-photon ionisation methods (See Section 4.4.5).

An example of the type of experiment that can be performed in this mode is illustrated in Figure 2.7. Figures 2.7a and 2.7b illustrate the importance of setting the correct timing between triggering the laser which vaporised the target rod and the laser which ionised the clusters. Figure 2.7a was obtained by monitoring the ion signal corresponding to the mass of helium as the trigger to the ArF excimer laser, used to produce the ions in the TOFMS, was scanned. By scanning the trigger to this laser, the helium pulse profile was mapped out. It can be seen that the pulse width is approximately 1 ms.

There is a significant dip in the helium pulse intensity at t = 1860 μs. This corresponds to that part of the gas pulse which was directly above the target rod at the time of vaporisation. The drop in intensity was caused by the laser generated plasma displacing the helium from the molecular beam [13].

Figure 2.7b was obtained by scanning the ionisation laser as before, but in this case the ion signal corresponds to ^{63}Cu. The clusters were present in only the small plug of the helium pulse which was disturbed in Figure 2.7a and not throughout the gas pulse.

Figure 2.7 : Illustration of the timing constraints on the detection of clusters. The figures illustrate that the signal due to ^{63}Cu is present in only a small part of the helium gas pulse and not throughout it. The dip in the helium pulse is due to the cluster plume displacing helium. Larger clusters behaved similarly to the atom.

Figure 2.7 : Example of a "Time Scan"

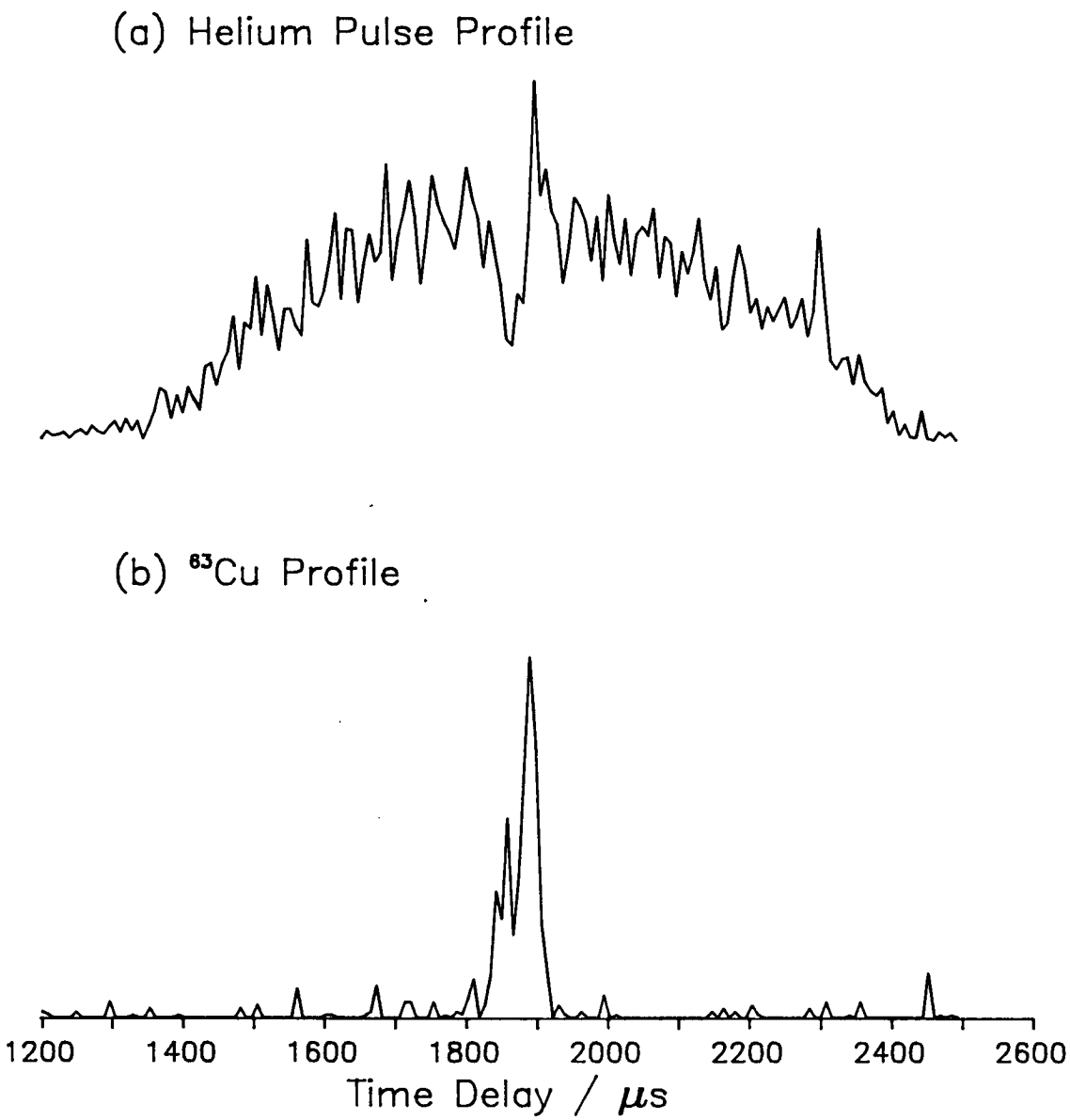

2.6.3 Acquisition of Spectroscopic Data

These experiments were used to obtain spectroscopic data on one or more clusters and are referred to as "frequency scans". Pre-selected mass channels were again required in order to study mass-selected signal. The experiments were performed via a resonant photoionisation scheme. The technique of resonant photoionisation is discussed in the following section.

The experimental cycle was repeated "N" times at a particular dye laser wavelength and the signal from the mass channels was summed, averaged and stored. The computer then triggered the stepper motor driving the grating of the dye laser, altering its wavelength. The experimental cycle was repeated another "N" times and the averaged ion signal from the mass channels was stored in the computer. This process of stepping the laser grating, performing "N" experimental cycles and storing the averaged signal was continued until a programmable stop wavelength was reached, yielding an array of averaged signal intensities. The approximate wavelength at which a particular element was acquired was contained in its position within the array.

The computer was capable of handling up to ten sets of independent mass channels and hence it was possible to scan the laser wavelength whilst monitoring several different clusters together with calibration fringes provided by a monitor etalon.

Figure 2.8 illustrates some results of spectroscopic data acquired in this manner. The spectrum of NbO was generated from a rod of niobium without addition of oxygen to the carrier gas and was recorded simultaneously with the Nb atomic spectrum. The spectrum did not disappear after the surface layer of the rod had been removed by the vaporisation laser, suggesting that oxygen had penetrated quite deeply into the rod.

Figure 2.8 : Illustration of spectroscopic experiments. The Nb atom spectrum exhibits many lines from the z ^{6}D ← a ^{6}D, z ^{6}F ← a ^{6}D, and the z ^{4}D ← a ^{4}F transitions. The NbO spectrum exhibits several bands from the G-X system ($^4\Sigma^- \leftarrow {}^4\Sigma^-$) transition, specifically the (0-1), (1-2), (2-3), (3-4), (4-5), (0-2), (1-3), (2-4), (3-5) bands.

Figure 2.8 : Spectroscopic Scans

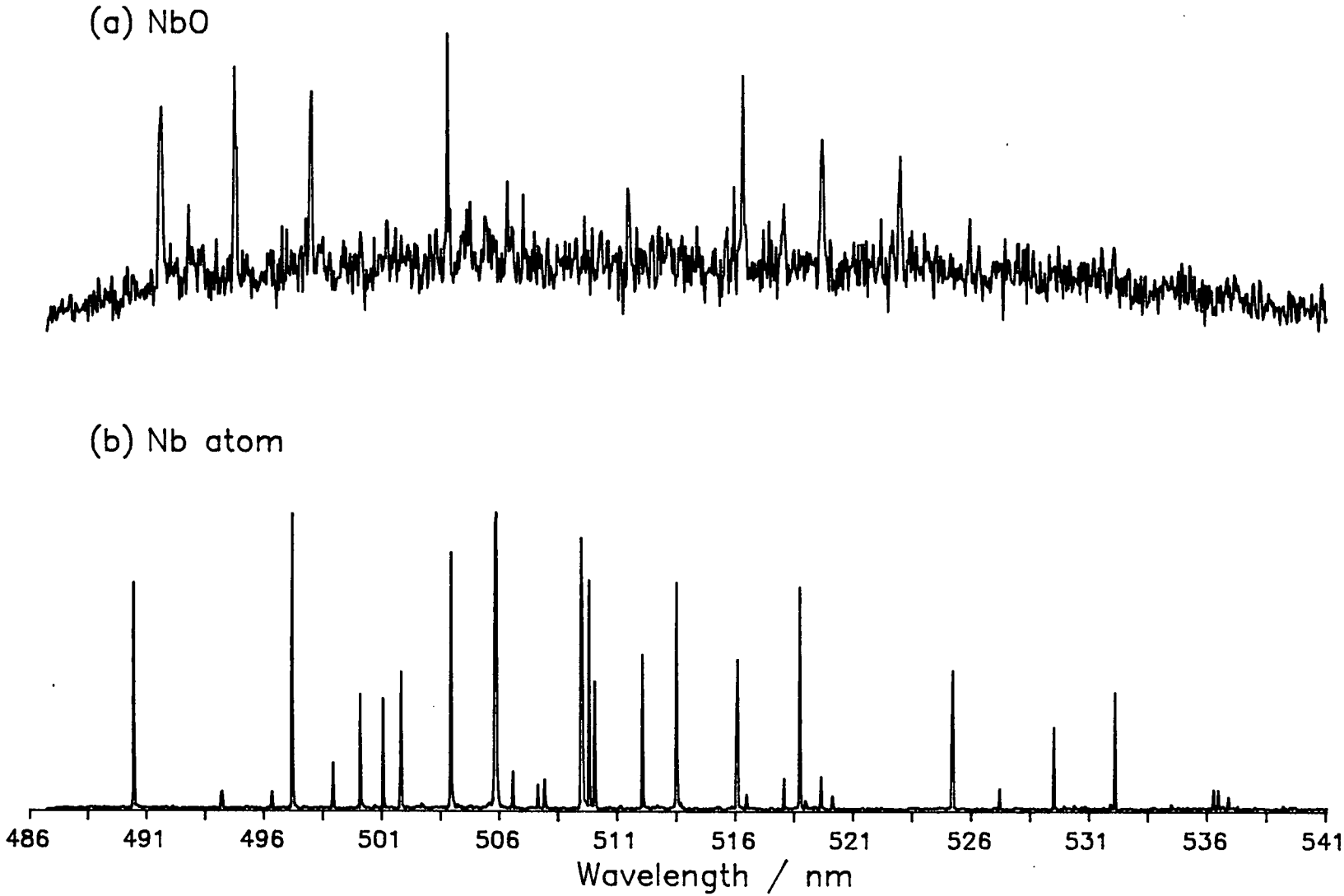

2.7 Photoionisation Techniques

The technique used to record the electronic spectra presented in this thesis was resonant two-photon ionisation. In this technique, ionisation occurs stepwise via an intermediate, resonant state. By monitoring the overall photoion yield as a function of excitation wavelength, a spectrum of the transition to the intermediate state can be obtained. This is illustrated by considering the three mechanisms by which a molecule can be ionised by either a single or by two photons. These are shown diagramatically in Figure 2.9.

2.7.1 Single Photon Ionisation

This process can occur when the energy of the incident photon is greater than the first molecular ionisation potential. It is a relatively facile process since the density of molecular states near the ionisation potential is usually high and selection rules are readily met. The latter factor is because the photoejected electron is able to carry away energy and angular momentum permitting strongly allowed transitions with good Franck-Condon factors [14]. The transition rate for absorption can be described by the equation [15],

$$W = \sigma_1 I$$

where,

W = transition rate in molecules per second

σ_1 = single-photon absorption cross-section in cm^2

I = radiation flux in photon $cm^{-2}s^{-1}$

Typically, single-photon absorption cross-sections are in the region of 10^{-16} to 10^{-22} cm^2 [15].

Figure 2.9 : Schemes for One- and Two-Photon Ionisation

Figure 2.9 : Single and Two Photon Ionisation Schemes

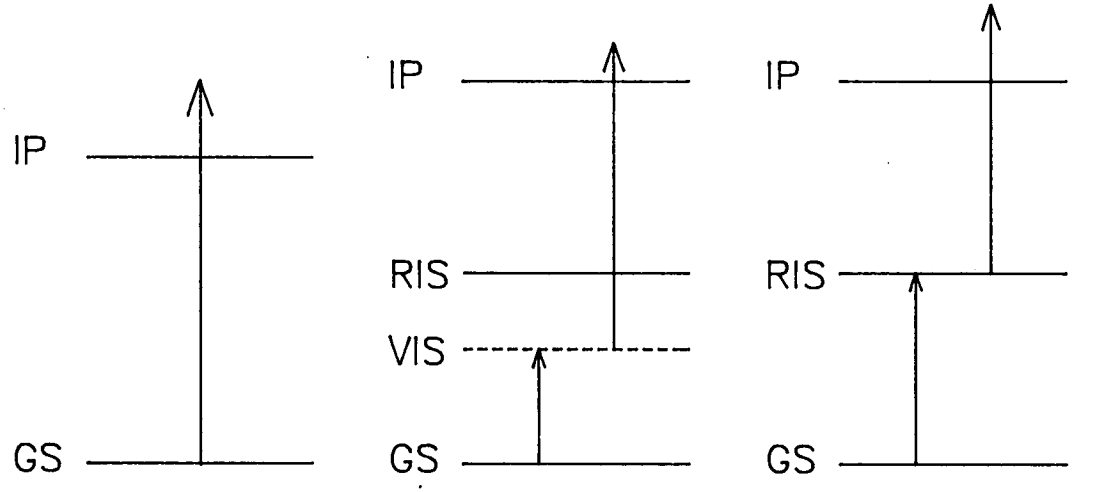

a) Single Photon Ionisation

b) Two Photon Non–Resonant Ionisation

c) Resonant Two Photon Ionisation

2.7.2 Non-Resonant Two-Photon Ionisation

When the photon energy is less than the molecular ionisation potential, but greater than half the value, and is also of such an energy that there are no excited states present at the correct energy to permit one photon absorption, then ionisation can be achieved by non-resonant two-photon ionisation. The transition rate is strongly dependent on the radiation flux and the rate of ionisation can be described by the equation [15],

$$W = \sigma_2 I^2$$

where,

σ_2 = two-photon absorption cross-section in cm^4 s

The other terms are as described previously.

The magnitude of σ_2 is very small compared to σ_1, typically being of the order of 10^{-50} cm^4s [16]. This process becomes more probable as the radiation flux is increased and most of the mass spectra described in this work were obtained using non-resonant two-photon ionisation with an argon fluoride excimer laser. The two-photon cross-section can be calculated from perturbation theory and its magnitude depends inversely on the sum of the differences between the energies of real states, E_i, and the energy of the photon [17]. The closer in energy the contributing real states E_i, are to the energy of the photon, then the greater is their contribution to the two-photon cross-section. It is therefore reasonable to suppose that when there is a real resonant state, then a rapid rise in the value of the absorption coefficient occurs. Although perturbation theory is not applicable when the first photon is resonant with a state, the implications are and the ion

signal produced via resonant two-photon ionisation can be orders of magnitude greater than the signal from non-resonant ionisation.

2.7.3 Resonant Two-Photon Ionisation

As described above, this technique applies when the first photon is in resonance with a molecular transition and is able to excite the molecule to a real resonant state. Transitions via real states are much stronger than non-resonant transitions, even if the real state is dissociative. The probability that a second photon can interact with the molecule and produce ionisation is greatly enhanced by the presence of a state resonant with the photon energy. The equation describing the rate of the transition can be written as [15],

$$W = \sigma_R I^n$$

where,

σ_R = two-photon resonant cross-section in cm^4 s

n = a number in the range 1 - 2.

It is the enhancement in ionisation observed when the first photon is resonant with a real intermediate state that presents the possibility of studying the intermediate state. Drawing on the terminology prevalent in optical-optical double resonance work [18], the first laser which promotes the transition between the ground state and the resonant state, will be referred to as the "pump" laser. The second laser responsible for ionising the molecule in the resonant state, will be referred to as the "probe" laser.

By scanning the wavelength of the pump laser and collecting the ion signal, it is

seen that the magnitude of the ion signal rises and falls dramatically as the pump beam moves into and out of resonance. A spectrum can be generated for the intermediate state. A distortion of the spectrum from the absorption spectrum may be produced by the probe laser also moving into and out of resonance as the wavelength of the pump laser is changed. However, distortions are likely to be small if the density of states accessed by the probe laser is high, if its bandwidth is large compared to the range in wavelength scanned with the pump laser and if the energy of the second photon is sufficiently high to take the molecule well above its ionisation threshold. These criteria were satisfied in the rotationally resolved spectra reported in this work since the pump laser was scanned over a narrow range of approximately 10 cm^{-1}, the probe laser was a broadband excimer laser and it excited the molecules to at least 1 eV above the ionisation threshold.

The detail attainable about the resonant intermediate state depends on the spectral resolution of the probe laser and the fundamental complication and congestion of the spectrum. Successful elucidation of the electronic spectra of the low-lying electronic states of copper dimer was only possible through the use of a high resolution dye laser as the pump laser and through mass-selective detection of the ion signal thereby removing isotopic congestion.

REFERENCES

1. T.G. Dietz, M.A. Duncan, and R.E. Smalley, J. Chem. Phys., **74**, 6511 (1981)

2. A.M. Butler, Ph.D. Thesis, Edinburgh University (1989)

3. J.B. Hopkins, P.R.R. Langridge-Smith, M.D. Morse, and R.E. Smalley, J. Chem. Phys., **78**, 1627 (1983)

4. A.G. Balzers, Document BG 800 105BE Liechenstein (1984)

5. T.E. Adams, B.H. Rockney, R.J.S. Morrison, and E.R. Grant, Rev. Sci. Instrum., **52**, 1469 (1981)

6. E.A. Rohlfing, D.M. Cox, and A. Kaldor, Chem. Phys. Lett., **99**, 161 (1983)

7. D.E. Powers, S.G. Hansen, M.E. Geusic, A.C. Puiu, J.B. Hopkins, T.G. Dietz, M.A. Duncan, P.R.R. Langridge-Smith, and R.E. Smalley, J. Phys. Chem., **86**, 2556 (1982)

8. P.J. Brucat, L.S. Zheng, C.L. Pettiette, S. Yang, and R.E. Smalley, J. Chem. Phys., **84**, 3078 (1986)

9. W.C. Wiley and I.H. McLaren, Rev. Sci. Instrum., **26**, 1150 (1955)

10. Lumonics Inc. Series TE-860-4 Excimer Laser Instruction Manual, Kanata, Ontario, Canada (1984)

11. J.L. Wiza, Nucl. Instr. Methods, **162**, 587 (1979)

12. J.L. Hellsing, L. Karrison, H.O. Andren, and H. Norden, J. Phys. E: Sci. Instrum. **18**, 920 (1985)

13. P.R.R. Langridge-Smith (Private Communication)

14. J.M. Hollas, *High Resolution Spectroscopy*, p444, Butterworths, London (1982)

15. D.H. Parker, *Ultrasensitive Laser Spectroscopy* Ed. D.S. Kliger, Academic Press, New York (1983)

16. P.M. Johnson and C.E. Otis, Ann. Rev. Phys. Chem. **31**, 139 (1981)

17. M. Goppert-Mayer, Ann. Phys. Leipzig, **9**, 273 (1931)

18. D.L. Andrews, *Lasers in Chemistry*, p95 Springer-Verlag, Heidelberg (1986)

CHAPTER THREE

Time-of-Flight Mass Spectrometry

3.1 Introduction

As discussed in Chapter II, cluster generation by laser vaporisation of a solid substrate into a molecular beam produces a soup of cluster sizes. The distribution of cluster sizes could be crudely controlled by changing either the backing pressure behind the nozzle or the length of extender piece in front of it. It was not possible, however, to "fine tune" the cluster distribution to predominantly contain species of just one size. Mass resolution of the ion signal was essential for the correct attribution of signal to carrier in the resonant two-photon ionisation studies reported in this thesis. This is readily illustrated in Figure 3.1.

Figures 3.1 a-c show the rotationally resolved spectrum of the 0-0 band of the C-X system of Cu_2 for all three isotopic combinations and Figure 3.1 d shows the composite spectrum that would have been obtained in the absence of mass resolution.

The nature of the experiments imposed severe constraints upon the type of mass spectrometer suitable. The experiments were performed in a pulsed mode with a duty factor less than 10^{-3}. The repetition rate was limited to 10 Hz by a variety of factors, such as the ability of the pumps to handle the high gas loads required for cluster generation, the design of the lasers and the speed of the data acquisition system. The low duty factor made it imperative to extract as much data as possible on each experimental cycle, which meant, in practice, that the mass spectrometer had to produce a complete mass spectrum on each cycle. The pulsed nature and the need for a complete mass spectrum per cycle were matched best by a TOFMS [1]. Precluding double-sector- and Fourier Transform mass spectrometers on the grounds of cost alone, the only alternative to the use of a TOFMS is the quadrupole mass filter. However, as the name implies, quadrupole mass filters selectively transmit ions of a particular charge-to-mass ratio whilst

discarding all the others. Even the fastest scanning quadrupole (approximately 6 amu per ms) would have been unable to acquire a complete mass spectrum on each and every cycle and its use would have resulted in an extremely inefficient collection of signal. The unsuitability of a quadrupole mass filter is not surprising since the instrument is designed to operate with a continuous source of ions rather than with a pulsed source. A TOFMS, on the other hand, requires a reference time, which is provided naturally in these experiments by the pulsed nature of the ionisation source. This results in an ideal match between the requirements of the experiment and the requirements of the mass spectrometer.

Figure 3.1 : Importance of mass resolution in simplifying spectral structure of the 0-0 band of the C-X system of Cu_2. Figures 3.1 a-c show the rotationally resolved spectra for $^{63}Cu_2$, $^{63}Cu^{65}Cu$ and $^{65}Cu_2$ respectively. Figures 3.1d was generated by combining the three spectra.

Figure 3.1 : Importance of Mass Resolution in Simplifying Spectral Structure

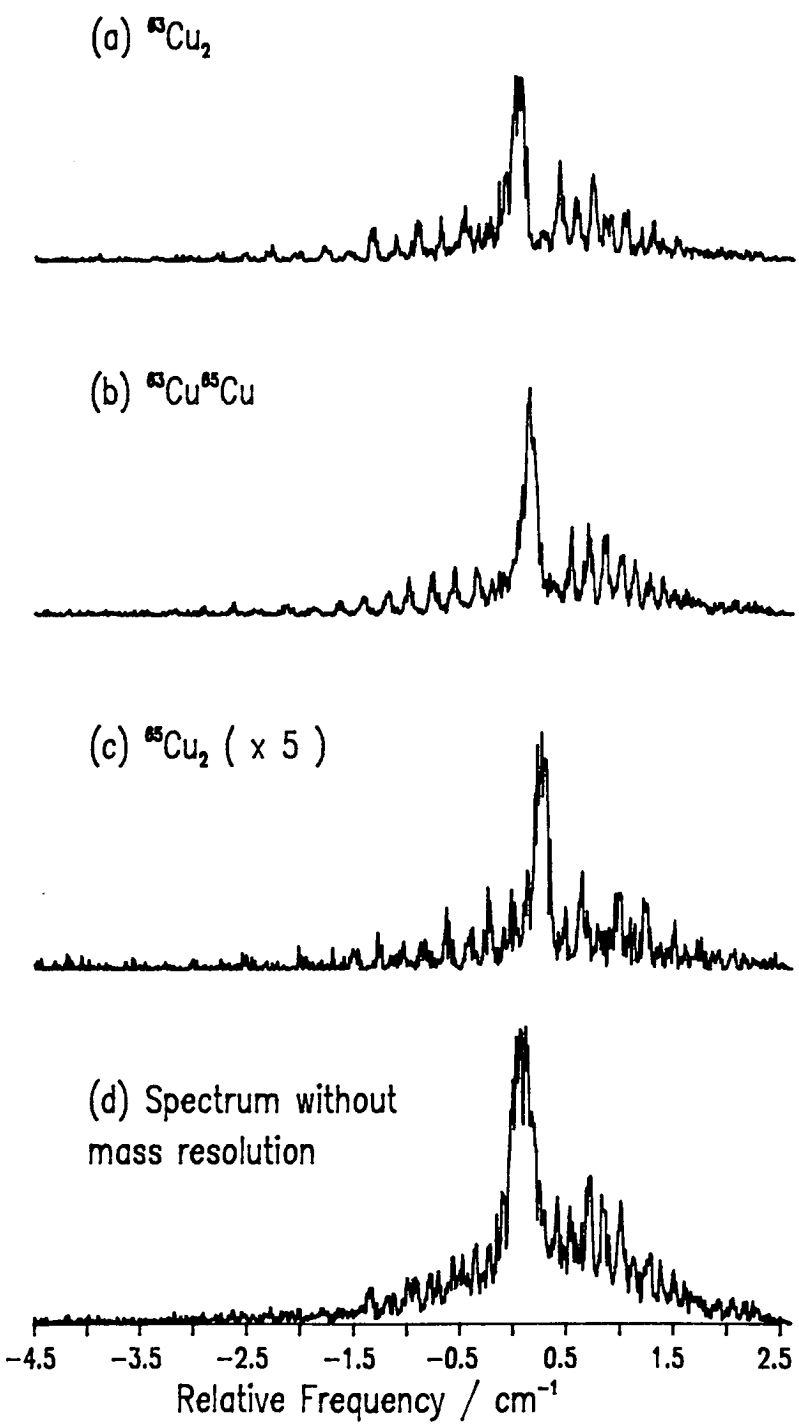

3.2 Principles of Operation of a TOFMS

Mass separation is achieved by the instantaneous generation of ions within the electric fields of the ion extraction optics, their acceleration and subsequent flight through a field-free region before their arrival at a detector. The ions traverse the field-free region, known as the drift tube, D, with velocities dependent on their charge-to-mass ratios (since all ions of the same charge extract the same energy from the electric fields in the acceleration region of the spectrometer). Heavier ions arrive at the detector after the faster, lighter ions. By recording the detector output as a function of time, a mass spectrum is obtained.

The flight time of an ion is related to its mass through the equation [2],

$$t_m = K\ m^{1/2} \qquad -(1)$$

where,

t_m = flight time of the ion of mass m.

K = proportionality constant.

The magnitude of K is determined by the parameters used in the physical design of the TOFMS and the initial energy of the ions. For example, the strengths of the electric fields used in the ion extraction optics and the size of the optics contribute to the value of K.

The two most important properties of a mass spectrometer are its resolution and its transmission. Unfortunately, a high resolution often results from a spectrometer being highly selective on the ions transmitted to the detector. Since TOF instruments place no filter on the transmitted ions, the resolution is generally

quite low and traditionally, this has been one of the major factors against their use. In the design of a TOFMS suitable for a particular application, several factors affecting the resolution and transmission of the instrument must be considered.

3.3 Resolution of a TOFMS

The limiting resolution can be defined as the mass at which the widths of the ion packets are just smaller than the difference between the flight times of ions separated in mass by 1 amu. With reference to equation (1), the difference in flight times is given by the formula,

$$\Delta t = t_{m+1} - t_m$$

$$= K \left((m+1)^{1/2} - m^{1/2} \right) \qquad -(2)$$

Clearly as the mass increases, the separation between flight times of adjacent species becomes smaller and even if the peak width were independent of the ion mass, a point would be reached when the TOFMS could no longer resolve adjacent mass peaks. The point at which resolution is lost depends on the widths of the ion packets and the value of K. A narrow packet width and a large value of K increase the maximum mass resolvable by the spectrometer.

The five factors affecting the resolution of a TOFMS by broadening the ion packet width are now considered.

Figure 3.2 : Schematic Diagram of the TOFMS Ion Extraction Optics.

Figure 3.2 : Schematic TOFMS Ion Extraction Optics

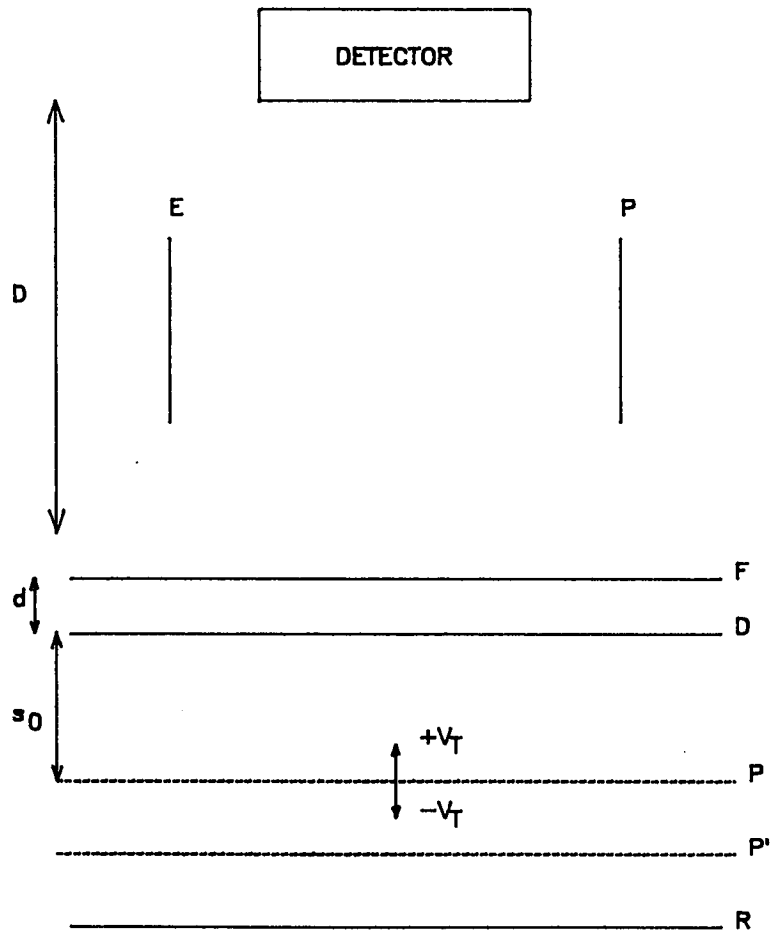

3.3.1 Factors Affecting the Mass Spectral Peak Widths in a TOFMS

3.3.1.1 The Potential at which the ion is formed - "Spatial Resolution"

With reference to Figure 3.2, all ions formed in plane P, perpendicular to the electric field and parallel to the detector will extract the same kinetic energy from the field. In the absence of all other peak broadening effects, all ions of the same charge-to-mass ratio will arrive at the detector simultaneously and the ion packet will be infinitely narrow. However, ions of the same charge-to-mass ratio formed in a different plane, for example P', or from different points of the same plane P, in the case of non-ideal fields, will extract varying amounts of energy from the field depending on their position. The infinitely narrow ion packet at the detector will acquire a finite width. Since this peak broadening is caused by the formation of ions at positions of different potential in the extraction region, the limiting resolution achievable with a particular mass spectrometer and caused by this effect is known as the "spatial resolution" of the instrument.

3.3.1.2 The Initial Energy of the Ions - "Energy Resolution"

The resolution of a TOFMS is affected by the component of velocity parallel to the spectrometer axis, the components in the plane perpendicular to the axis affect the transmission of the instrument. The simplest way to consider the effect of the initial ion energy is to consider the case of two ions in plane P subjected to ideal electric fields. If the ions had no velocity component along the axis of the TOFMS, they would arrive at the detector simultaneously. If, however, one ion had a velocity component of $+v_T$ along the TOFMS axis (positive towards the detector) whilst the other had a component $-v_T$, they would not arrive simultaneously. The second ion would lag the first ion by a "turn-around" time which depends on the ion energy and the strength of the electric field. The

"turn-around" time is the time taken for the ion with velocity $-v_T$ to decelerate and to return to its initial position with velocity $+v_T$. The ion would then follow a trajectory identical to that of the ion which originally had velocity $+v_T$ and would arrive at the detector delayed by the "turn-around" time. A distribution of initial energies will yield ion packets of finite width. By analogy to the case of spatial resolution, this effect is known as "energy resolution".

3.3.1.3 The Ionisation Source - "Timing Resolution"

In a simple TOFMS, the temporal width of the ion packet reaching the detector cannot be less than the temporal width of the ionisation source. Pulsed lasers readily produce light pulses shorter than 20 ns making them ideal ionisation sources for TOF instruments. Before the advent of pulsed lasers, timing resolution of the ion source was a major contributor to the temporal width of the ion packet and hence a fundamental limit on the resolution achievable with a TOFMS. For mass spectrometers which operate in a continuous mode, the precise time of ionisation is not so critical and electron impact ionisation is suitable. For time-of-flight mass spectrometry, the temporal characteristics of the ionisation source are vitally important to the resolution.

3.3.1.4 The Detector Response

The detector response includes the speed at which the ion signal can be transformed into an electrical signal and the speed at which the electrical signal can be processed. Both factors affect the observable mass resolution of a TOFMS without affecting its intrinsic resolution. If one considers a mass spectrometer capable of producing two adjacent mass peaks each of 5 ns temporal width and separated in arrival time at the detector by 20 ns then the mass spectrometer can be described as physically resolving the peaks. If the detector greatly broadens the

peaks or if the instrument which stores the time dependent output of the detector samples at, for example, only 10 MHz, resolved peaks will not be observed even though they were produced in the mass spectrometer. Hence, the TOFMS has to be designed to match the broadening effects of the detector and the sampling frequency of the instrument which monitors the detector output. No matter how effective the mass spectrometer is in maintaining narrow peak widths, if the detector response is not matched to the packet widths, no resolution, and possibly no spectrum, will be obtained.

3.3.1.5 Space-Charge Effects

The repulsion between ions of like charges travelling as a packet can serve to spread out the packet. The required ion density for such effects to become important has been suggested to be in the range 10^6 - 10^8 cm^{-3} [3][4]. It has been calculated that the number of ions generated experimentally was in the region of 10^2 - 10^4 (see Section 4.3.5) per pulse and the ions were produced in a volume of 0.05 cm^3. The ion density was therefore in the range 2×10^3 - 2×10^5 cm^{-3} and the effects of space-charge repulsion are believed to be small. The effects of space-charge repulsion on the resolution are therefore not considered in any greater detail.

The forementioned factors affecting the resolution of a TOFMS have been treated in various ways to minimise their effect. The problems of timing resolution and detector response can be tackled in two ways. The first and simplest is to increase the flight time of the ions as this increases the temporal separation of adjacent mass packets. Since the temporal width of the ionisation source is constant it becomes relatively less important as the ion flight time is increased. Similarly, the greater difference in flight times between adjacent mass peaks places lower demands on the detector response. The second way to reduce the problems of

timing resolution and detector response is to use shorter ionisation sources, such as picosecond pulsed lasers, and faster detectors [5], [6]. Ultimately, this path offers better performance since increased flight times result in lower transmission as the velocity components in the plane perpendicular to the TOFMS axis become more significant.

Energy resolution was improved by Mamyrin *et al* [7] in 1973. They used a "V" shaped TOFMS, known as a "reflectron", with the ion source at the end of one limb of the "V" and the detector at the end of the other limb. At the apex of the "V", they placed an electric field to reflect ions accelerated from the ion source to the detector. Energy resolution can be improved because ions with a greater velocity penetrate deeper into the reflecting field than the slower ions and spend longer in this region. Conditions can be chosen such that ions are temporally focused at the detector. This type of TOFMS was not used in the present work and will not be discussed any further.

The problem of spatial resolution was treated in 1955 by Wiley and McLaren [8] They developed a two-field ion acceleration region which enabled first-order focusing of the ions such that ions from different positions in the ionisation region would arrive at a detector placed a particular distance downstream at approximately the same time. The TOFMS used in this work follows the design described by Wiley and McLaren and the following treatment of spatial resolution is after them.

3.3.2 Wiley and McLaren Condition for Optimum Spatial Resolution

Wiley and McLaren tackled the problem of spatial resolution by using a two-field acceleration region as illustrated in Figure 3.2 .

Consider ions of initial energy U_0 formed in a plane P which is a distance s_0 from

plate D. All electric fields are considered to be ideal.

The equations describing the motion of a particle of charge q and mass m are [8],

$$T_s = (2m)^{1/2} / qE_s \left(\left(U_0 + qs_0E_s \right)^{1/2} \pm U_0^{1/2} \right) \qquad -(3)$$

$$T_d = (2m)^{1/2} / qE_d \left(\left(U^{1/2} - \left(U_0 + qs_0E_s \right)^{1/2} \right) \right. \qquad -(4)$$

$$T_D = (2m)^{1/2} \left(D / 2U^{1/2} \right) \qquad -(5)$$

where,

$$U = qs_0E_s + qdE_d + U_0 \qquad -(6)$$

and T_s, T_d, and T_D are the flight times for the ion to traverse the distances from plane P to plate D, from plate D to plate F, and from plate F to the detector, respectively.

Defining k_0, as

$$k_0 = \left(s_0E_s + dE_d \right) / s_0E_s \qquad -(7)$$

The total ion flight time, T_T, from the point of ionisation is given by,

$$T_T = (2m)^{1/2} \left(U^{1/2} / qE_d + \left(1 / qE_s - 1 / qE_d \right) \right.$$
$$\times \left(U_0 + qs_0E_s \right)^{1/2} + D / 2U^{1/2} \pm U_0^{1/2} / qE_s \left. \right) \qquad -(8)$$

For small displacements, Δs, about plane P, T_T can be approximated by a Taylor expansion,

$$T_T (s_0+\Delta s) = T_T(s_0) + \sum 1 / n! (\partial^n T(s_0) / \partial s^n) (\Delta s)^n \quad -(9)$$

Wiley and McLaren obtained an expression which forced $\partial T / \partial s = 0$ and hence yielded first-order spatial focusing of the ions. Equating,

$$\partial T_T / \partial s = 1 / 2 (2m)^{1/2} (U^{-1/2} E_s / E_d + (1 - E_s / E_d) \times (U_0 + qs_0E_s)^{-1/2} - 1 / 2 qE_sDU^{-3/2}) \quad -(10)$$

to zero, yields the following expression for the required length of drift tube, D,

$$D = 2U^{3/2} / qE_s (E_s / E_d U^{-1/2} + (1 - E_s / E_d) (U_0 + qs_0E_s)^{-1/2}) \quad -(11)$$

Equation (11) is a function of the initial ion energy U_0. The sensitivity of the required drift tube D to the initial energy U_0 can be estimated by expanding D as a Taylor Series in U_0. Neglecting all terms greater than the first-order term,

$$D (U_0+\Delta U_0) - D (U_0) = (2 / qE_d + 2 / qE_s (1 - E_s / E_d) \times (U^{1/2} (U_0 + qs_0E_s - 1 / 2 qdE_d) / (U_0 + qs_0E_s)^{3/2}) \Delta U_0 \quad -(12)$$

At $U_0 = 0$ and substituting in parameter k_0 from equation (7) into (12) and (11) respectively,

$$D (\Delta U_0) - D (0) = (2 / qE_d + 1 / qE_s (1 - E_s / E_d) \times (k_0^{1/2}(3 - k_0))) \Delta U_0 \quad -(13)$$

$$D = 2 s_0 k_0^{3/2}(1 - 1 / (k_0 + k_0^{1/2}) d / s_0) \quad -(14)$$

Equation (14) defines the first-order focus of the ions which is independent of mass and dependent only on the electric fields applied in the two regions of the

extraction optics, the position of ionisation within the first electric field and the initial ion kinetic energy. Equation (13) shows the sensitivity of the focal position defined in (14) to initial ion energy; it does not define a focusing condition for a spread in initial energy. To obtain the latter, equation (8) must be expressed as a Taylor Series in U_0 and $\partial T_T / \partial U_0$ equated to 0.

$$\partial T_T / \partial U_0 = 1 / 2 (2m)^{1/2} (U^{-1/2} / qE_d + (1 / qE_s - 1 / qE_d) \times (U_0 + qs_0E_s)^{-1/2} - 1 / 2 DU^{-3/2} \pm U_0^{-1/2} / qE_s) \quad -(15)$$

At $\partial T_T / \partial U_0 = 0$,

$$D = 2U^{3/2} (U^{-1/2} / qE_d + (1 / qE_s - 1 / qE_d) \times (U_0 + qs_0E_s)^{-1/2} \pm U_0^{-1/2} / qE_s) \quad -(16)$$

Due to the last term, $\pm U_0^{-1/2} / qE_s$, this cannot be an exact focal position.

When $U_0 = 0$, equation (16) simplifies to equation (14) and hence the first-order focus for ions with initially no kinetic energy and with small spatial displacements around s_0 is the same as the focal position for ions formed at s_0 with small initial kinetic energies. It is not possible to improve on the Wiley and McLaren first-order focus with simple two-field ion acceleration optics [9].

The focal position has a small dependence on U_0 as shown in equation (13). For systems used in this work, the ions have small variations of approximately 10^{-3} eV about the average energy (that is, kinetic energy due to the component of velocity parallel to the TOFMS axis). Using the experimental values for E_s, E_d, and k_0,

$$D (0+10^{-3}) - D (0) = -2.13 \times 10^{-6} \text{ m}$$

Thus for the likely initial ion energies in the system, the equations derived

assuming $U_0 = 0$ are valid. The remainder of the treatment assumes this condition to hold.

Equation (14) gives the first-order focal position, that is, the required drift length such that ions formed at s_0 and at small displacements around s_0 arrive at the detector at approximately the same time. How approximate depends on the magnitude of the higher terms in the Taylor expansion, equation (9). Due to the smallness of Δs, it will be assumed that the most significant of the remaining terms is the second-order term, $1 / 2\ \partial^2 T / \partial s^2\ (\Delta s)^2$. At $U_0 = 0$,

$$\partial^2 T_T / \partial s^2 = 1 / 4\ (2m / qE_s)^{1/2}\ 1 / (s_0 k_0)^{3/2} \times ((k_0^{3/2} - 1)\ 1 / (k_0 - 1)\ d / s_0 - k_0^{3/2} + 3D / 2 s_0 k_0) \quad -(17)$$

and substituting in the first-order value of D,

$$d^2 T_T / ds^2 = 1 / 4\ (2m / qE_s)^{1/2}\ (qE_s / U)^{3/2} \times [\ 2E_s / E_d + k_0^{1/2} (3 - k_0)\ (1 - E_s / E_d)\ ] \quad -(18)$$

For constant field strength E_s and constant total energy, U, the sign and absolute magnitude of $\partial^2 T_T / \partial s^2$ are determined by the quantity in the square brackets. If the term is positive, then the flight times of ions from positions slightly displaced from s_0 will be greater than the flight time of ions from s_0; if it is equal to zero, the flight times of ions from positions displaced from s_0 and from s_0 will be equal to second-order and higher order terms will be responsible for differences in flight times. Finally, if the term in square brackets is negative, the flight times of ions formed with slight displacements from s_0 will be less than the flight times of ions formed at s_0. At first sight, a spectrometer should be chosen such that $\partial^2 T / \partial s^2 = 0$ and the only contribution to spatial peak broadening would be third or higher order terms. However, the resolution of the spectrometer depends on other factors

and these must be considered in determining the overall resolution of a TOFMS.

3.3.3 Overall Resolution in TOFMS

The overall resolution of a TOFMS depends on a combination of the temporal width of the ion packets at the detector and on the time separation between adjacent ion packets. With reference to equation (3), it is readily seen that the separation between the peaks is proportional to the flight time and hence the resolution is dependent on the flight time of the ions. The factors affecting the ion packet width have been outlined above. The flight times of ions of a particular mass can be readily calculated from equation (8). Practically, it is found that satisfying the second-order spatial focus requires the use of a relatively short drift tube. This results in a consequent reduction in ion flight times which outweighs the gain in resolution achieved by the narrower ion packets at the second-order focus.

3.4 Ion Transmission Function

There are only two requirements of the transmission function of a TOFMS : it should be as large as possible and essentially mass independent. The ion transmission function is affected by several factors, such as the divergence of the ion source, the flight time of the ions and the finite size of the detector. The factors combine to give the overall transmission function and it is clear that a source of low divergence, a short flight time and a large detector size all contribute to a high transmission function.

The ion transmission function can be further reduced by the presence of obstacles in the ion flight path, such as high transmission grids used to define the electric fields of the ion source.

The simplest way to estimate ion transmission function is to consider ions as originating from a point source along the TOFMS axis. The ion intensity is attenuated at each of the grids through which the ions must pass to leave the acceleration region of the TOFMS. If the ions pass through n grids each of equal transmittance T_R, the ion intensity after leaving the acceleration region will be,

$$I_{DT} = T_R^n \, I_S$$

where,

I_{DT} = intensity of the ions at the start of the drift tube

I_S = intensity of the ions at the source

The total flight time, T_F, of the ions can be approximated by the equation,

$$T_F = D \, (\, m \, / \, 2U \,)^{1/2}$$

where,

D = length of the drift tube

m = mass of the ion

U = energy of the ion.

If the radius of the circular detector is r, then a limiting off (TOFMS) axis speed can be defined such that ions with greater speeds move so far from the TOFMS axis that they are not detected. The limiting speed is defined by,

$$v_{lim} = r \, / \, T_F$$

If further, the velocity distribution of the ions is assumed to be Boltzmann with a mean zero velocity away from the TOFMS axis, then the proportion of ions with speeds greater than the limiting value , v_{lim}, can readily be calculated. Using a two-dimensional Boltzmann distribution [10], the proportion of ions reaching the detector from the ion source can be approximated by,

$$I_{det} = I_S \; T_R^n \qquad \int_0^{v_{lim}} mv / kT \; e^{- mv / kt} \, dv \qquad -(19)$$

Equation (19) is only an approximation to the true transmission function since the transmission function is affected by factors neglected in the calculation. For example, stray electric or magnetic fields, space-charge repulsions and collisions with background gas may all further reduce the transmission function. The calculations are also based on assumptions which are only valid at a high level of approximation. The assumptions are discussed below.

i) The ion source is not strictly a point source but a line of point sources. Those point sources off the TOFMS axis will have smaller transmission functions than the point source located on the axis. The overall transmission function will be less than that calculated for a single point source located on the TOFMS axis.

ii) It has been calculated that the temperature distributions perpendicular and parallel to a supersonic molecular beam axis are different, limiting the validity of the assumption of a common two-dimensional velocity distribution [11].

iii) In the configuration used in this work, the TOFMS axis was perpendicular to the molecular beam axis and ions were generated with a large velocity along the molecular beam axis. Deflection plates were placed above the acceleration region of

the TOFMS to remove the energy associated with the directed flow.

If one considers a pair of deflection plates of length d and with an electric field of strength E between them, then an ion with energy U_{PD} perpendicular to the field and energy U_{PL} parallel to the field will extract an energy

$$E = -Edq\,(U_{PL} / U_{PD})^{1/2} + E^2q^2d^2 / U_{PD}$$

from the field. This is mass independent and the appropriate field strength and plate length could be chosen to remove the ion kinetic energy associated with motion parallel to the field. Unfortunately, the nature of the cluster ion source is to produce ions which have approximately the same velocity along the molecular beam axis irrespective of mass [12]. The heavier clusters therefore possess more energy associated with this motion than the lighter ones. The deflection plates thus introduce mass discrimination into the transmission function [13] and the assumption of a Boltzmann distribution with zero mean velocity with respect to the TOFMS axis is valid only for a small range of masses at any particular value of the electric field between the deflection plates. This mass discrimination is illustrated in Figure 3.3, which shows mass spectra of copper clusters taken under identical conditions except for the voltage across the deflection plates. It is clearly seen that the higher voltage over-compensates for the directed flow of the lighter clusters and that the lower voltage under-compensates for the directed flow of the heavier clusters.

The method of calculating ion transmission functions is highly approximate but has the advantage of being quick and simple. A different method of estimating ion transmission functions is described in Section 3.6.3 .

Figure 3.3 : Mass discrimination of the deflection plates. Figure 3.3a was recorded with 250 V across the deflection plates. Figure 3.3b was recorded with 450 V across the deflection plates, significantly favouring the heavier clusters.

Figure 3.3 : Effect of Deflection Plate Voltage on the Mass Spectrum of Copper Clusters

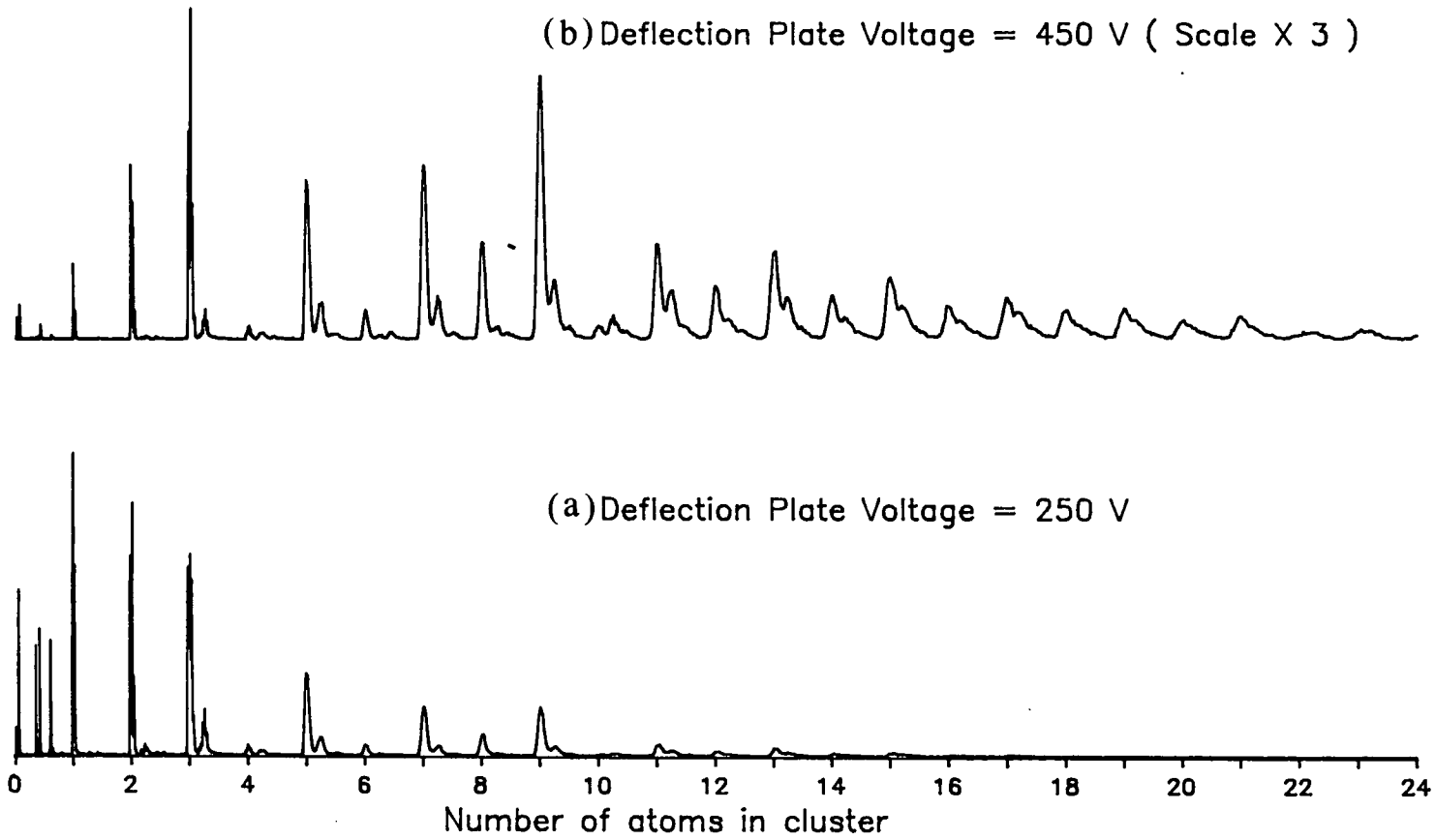

3.5 Choice of an Experimental TOFMS

The analytical equations introduced earlier can be used to calculate the flight times of ions with any displacement and any initial velocity parallel to the TOFMS axis. If the TOFMS is restricted to obey the Wiley and McLaren condition for spatial focusing, then several empirical rules can be derived by performing calculations on ions with different displacements and velocities for a variety of TOFMS parameters. Calculations were performed on benzene ions with translational temperatures along the TOFMS axis of between 0.03 and 300 K, displacements from s_0 as large as s_0 itself and for electric field strengths of E_s between 10 - 10^5 Vm^{-1}. The results of the calculations were always unambiguous and empirical rules were derived for identifying the ion which had the longest flight time and the one which had the shortest. For a TOFMS with a focal point that is a maximum, the ion of shortest flight time is the one closest to the detector and with maximum velocity towards the detector. The ion with the longest flight time is the one at s_0 and with maximum velocity away from the detector. Similar rules could be developed for a TOFMS with a focal point at a minimum. It was not possible to develop such simple rules for a TOFMS where the focal point was a point of inflection.

Practical TOF instruments are invariably selected with the focal position as a maximum since this permits longer drift tubes and better resolution. Hence using the rules derived for a TOFMS with a maximum focal point and by tracking the ions of longest and shortest flight time, a crude estimate of the ion packet width can be obtained. With the inclusion of the temporal distribution of the ionisation source, the maximum resolvable mass of the instrument can be estimated. By making reasonable assumptions about the spatial and energy distributions, the maximum resolvable mass could be calculated for a TOFMS with a series of

parameters. A further empirical rule was derived which showed that if the maximum voltage applied to the repeller plate and the length of the drift tube are fixed, then the highest resolving TOFMS is the one with the largest value of s_0. This rule was used as guidance in selecting the parameters for an experimental TOFMS.

There were certain physical constraints imposed on the design of the TOFMS. The flight tube was to be between 1.2 - 1.5 m since previous studies had been successful using flight tubes of this length. The length chosen was 1.32 m. Due to the requirement for deflection plates above the ion acceleration region, the combined size of (s_0 + d) was limited to 50 mm. Finally, the maximum voltage that could be applied to the repeller plate was limited to 3.5 kV by the available power supplies. The experimental parameters chosen are listed in Table 3.4, along with the estimated maximum resolvable mass. It is instructive to compare the predicted performance of the TOFMS with that obtained experimentally.

Table 3.4 : Parameters used in the Experimental TOFMS

Voltage on Repeller Plate	: 3015 V
Voltage on Draw-out Grid	: 2555 V
Voltage on Flight Grid	: 0 V
Repeller / Draw-out distance	: 32 mm
Draw-out / Flight distance	: 6 mm
Flight / Deflection plates	: 17 mm
Length of drift tube	: 1.32 m
Temporal width of ion packet at mass = 98 amu	: 6 ns
Maximum resolvable mass by simple method	: 540 amu

3.6 Comparison of the Experimental and Theoretical TOFMS

3.6.1 Experimental Performance of the TOFMS

Figure 3.5 shows the mass spectrum of carbon clusters in the size range up to 140 atoms. The spectrum was taken by photoionising the clusters using ArF radiation and the spectrum was recorded with 460 V on the deflection plates. It is clear from the spectrum that the experimental performance of the TOFMS is far inferior to that predicted with the crude model described in Section 3.5 and quoted in Table 3.4 .

Figures 3.6a and 3.6b show unit mass resolved spectra for Mo^+ and Mo_2^+ , respectively. The spectrum of Mo^+ was taken non-resonantly by photoionising with 266 nm radiation. The spectrum of Mo_2^+ was taken through a resonant scheme via the A-X system of Mo_2 [14]. The resolution of the instrument, defined as M / Δm where M is the mass of the species and Δm is the peak width [15], is 364 and 385 for Figures 3.6a and 3.6b respectively. A similar resolving power was reported by Riley [16].

Figure 3.7 shows the peak corresponding to $^{98}Mo^+$ greatly expanded. The FWHM of the peak is approximately 26 ns, compared to 6 ns from the crude model presented in Section 3.5 . It was not possible to reduce the experimental peak width by fine-tuning the voltages applied to the ion extraction optics, suggesting that the observed resolution was a fundamental limit to a real TOFMS. Since the resolution was so markedly different from that predicted, it was decided to investigate the discrepancy further. The most likely cause for the discrepancy was thought to be due to the crude model used to estimate peak widths. It was therefore decided to treat the problem more rigorously.

Figure 3.5 : Mass spectrum of carbon clusters illustrating the high mass resolution of the experimental TOFMS.

Figure 3.5 : Mass Spectrum of Large Carbon Clusters

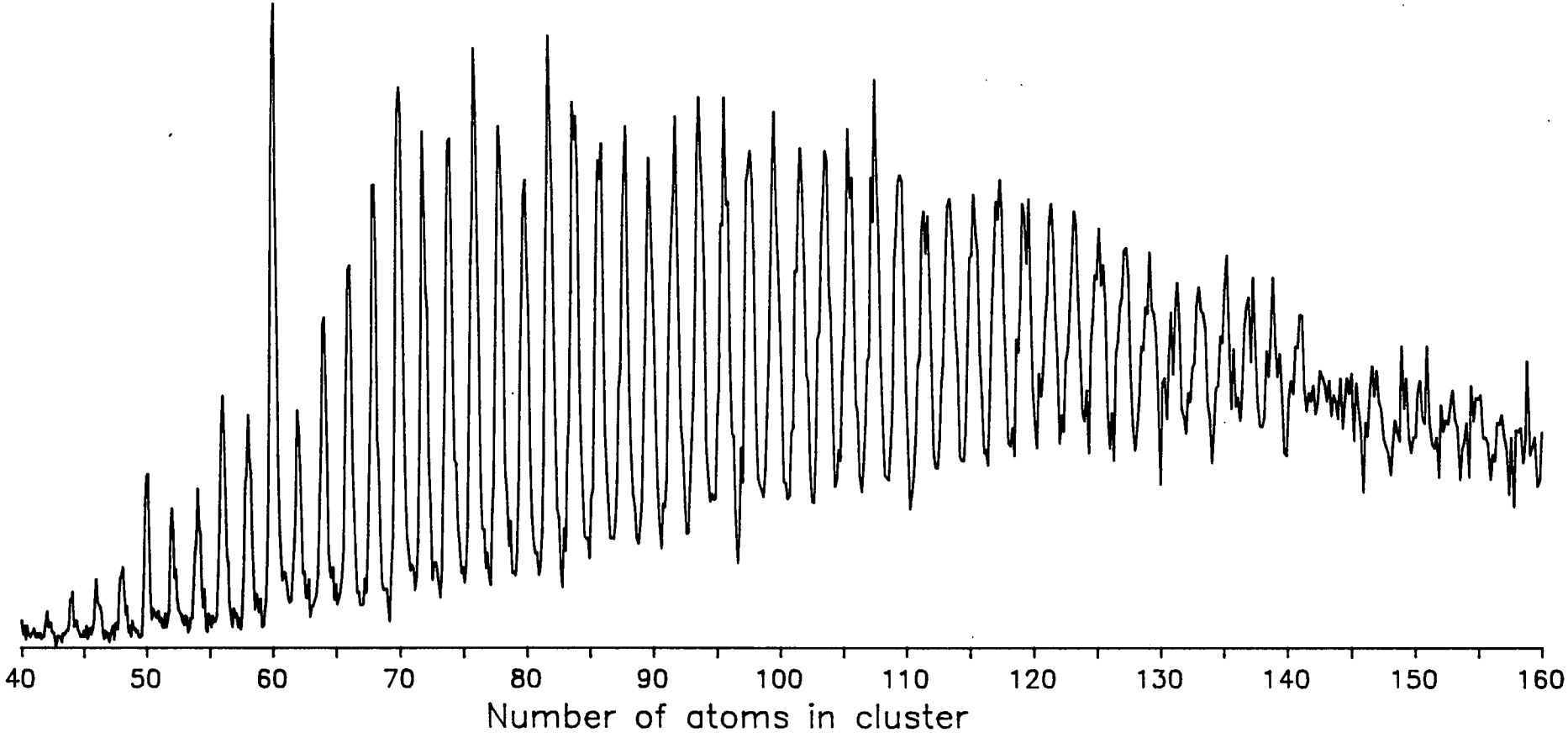

Figure 3.6 : Mass Spectra of Mo^+ and Mo_2^+

Figure 3.6 : Mass Spectra of Mo and Mo_2

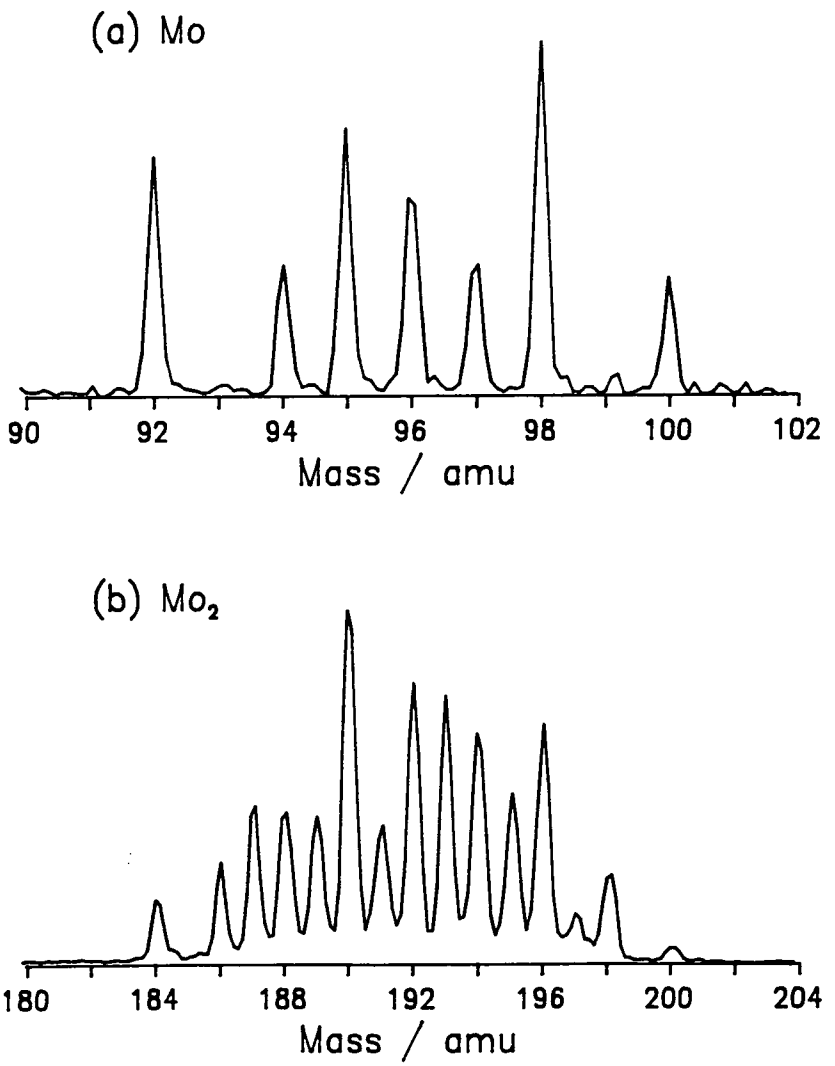

Figure 3.7 : Expanded Mass Peak of $^{98}Mo^{+}$

Figure 3.7 : Expanded ^{98}Mo Peak

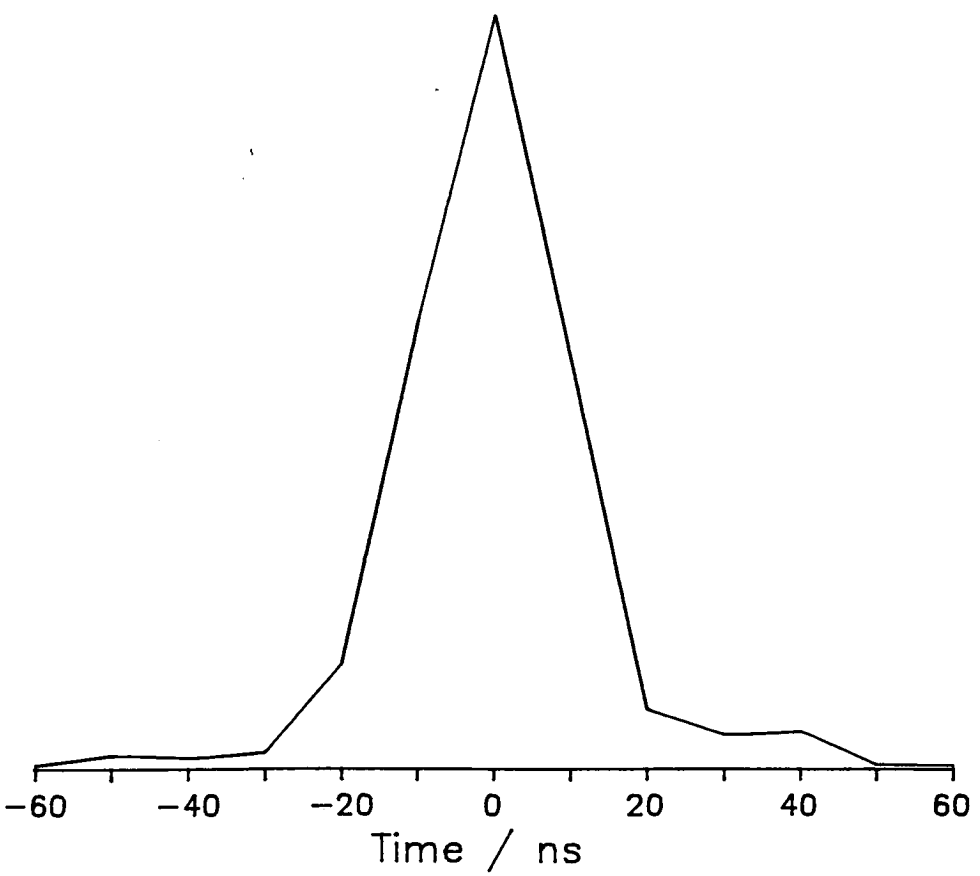

3.6.2 Analytical Treatment of the TOFMS

The method used to simulate the mass spectral peaks analytically is described in Appendix A. The program was tested by performing simulations on benzene and using parameters reported by Opsal *et al* [17]. The results obtained were in very good agreement with the published simulations. The simulations described below were all performed on $^{98}Mo^{+}$.

The clusters were generated in a molecular beam and photoionisation was achieved with an apertured laser beam. The spatial distribution of the ions was assumed to be Gaussian with a FWHM of 1.0 mm about s_0. The spatial distribution of the ions is the product of the spatial distribution of the neutrals and the spatial dependence of the photoionisation laser power. The latter could be considered constant over a small range of 3 - 4 mm. Simulations were performed treating the spatial distribution of the ions as either a delta function of width 1.0 mm or as a Gaussian distribution with a FWHM of 1.0 mm. No significant difference to the final simulated peak width was made by the choice.

The velocity distribution was also assumed to be Gaussian. The most efficient cooling within a supersonic molecular beam occurs with the translational modes [18] and since rotational temperature have been measured as low as 6 K (see Section 4.4), it should be reasonable to assume that the translational temperature is equally as low. In the simulations the velocity distribution was treated as having a standard deviation of 41 ms^{-1}, equivalent to a temperature of 20 K. By erring on the hot side with the translational temperature, an upper limit to the contribution of the velocity distribution to the peak width was obtained.

The ionisation source employed in these experiments was a high powered pulsed laser. Attempts to measure the temporal pulse width by monitoring the output

from a fast photodiode with a 100 MHz transient digitiser or on a 125 MHz oscilloscope suggested that the FWHM of the pulse was less than 10 ns. In the simulations, therefore, the photoionisation source was treated as having a Gaussian profile with a FWHM of 10 ns.

Figure 3.8a displays the mass peak for $^{98}Mo^{+}$ simulated by setting all but the spatial distribution to zero. The peak is asymmetrical with a sharp cut-off at longer flight times and a relatively long tail to shorter flight times. The shape of the peak is as expected since the value of k_0 was such that the TOFMS focused to a maximum. Ions with small displacements from s_0 had shorter flight times than those from s_0 leading to the tail to shorter flight times.

The simulation shown in Figure 3.8b was obtained by setting all but the velocity distribution to zero. It is significantly broader than the width due to the spatial distribution, suggesting that even in a molecular beam with a translational temperature of 20 K, the spread of initial energies made a significant contribution to the mass peak width. The peak width displayed in Figure 3.8b can be considered an upper limit to the contribution from the velocity spread.

Figure 3.8c shows a simulation that was obtained by setting all but the time distribution to zero. It too is significantly broader than the width due to the spatial spread. The simulations suggest that the major contributions to the analytical peak width are due to the velocity distribution and the temporal width of the ionisation source.

Figure 3.8d is the simulated mass peak with none of the distributions set to zero.

Figure 3.8 : Analytical peak shapes calculated for $^{98}Mo^{+}$ using experimental parameters for the TOFMS.

Figure 3.8
Analytical Peak Shapes

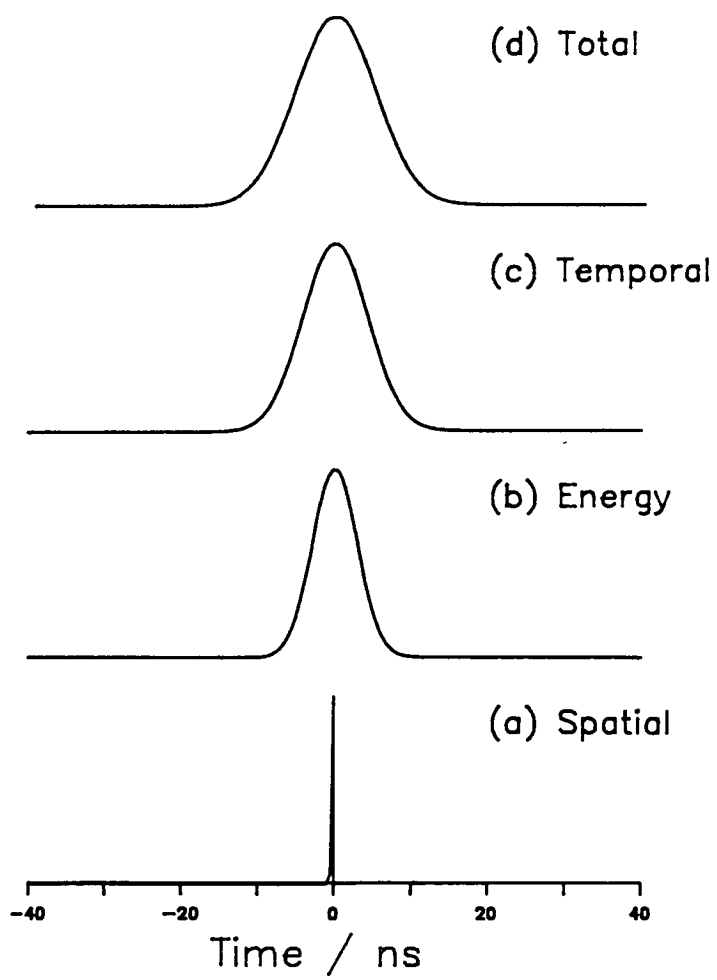

The simulations implicitly assumed that ions with all possible values of the s, v, and t variables would reach the detector. The only reason for this not happening is if the velocity components perpendicular to the TOFMS axis resulted in some ions missing the detector. This can be calculated from equation (19). Using a detector radius of 9 mm, the limiting off TOFMS axis velocity for ^{98}Mo to hit the detector is 464 ms^{-1}. The proportion of ions having velocities greater than this at 20 K is negligible. Hence, irrespective of the values of s, v and t, all ions would reach the detector. In passing through the extraction optics the ion pass through two 90 % transmitting grids and in front of the detector there is another 82 % transmitting grid. Hence the transmission function is reduced to 66 %. However, the attenuation introduced by the grids is indiscriminate and the peak shapes in Figure 3.8 will not be distorted. They can be viewed as the true analytical approximations to the mass spectral peaks.

Comparison with the experimental peak illustrated in Figure 3.7 shows that the experimental peak is significantly broader than the simulated one. There are immediately two likely causes of the broadened peak width:

1) As stated previously, a set of deflection plates had to be applied above the extraction optics to remove ion velocity along the molecular beam axis. These plates introduced an electric field into what should have been a field-free region. Ions which closer approach the positively biased plate P (Figure 3.2) sample a higher potential and are more retarded than ions which traverse the region close to the earthed plate E. This effect introduces an additional peak broadening to those previously considered.

2) The analytical equations assume perfect electric fields, which, to a greater or lesser extent, must be approximations. Any irregularities in the fields will serve to enhance the spatial peak-broadening factors.

It was decided to investigate these two peak-broadening effects with a Monte Carlo trajectory program using a two-dimensional model of the potential within the extraction optics and between the deflection plates.

3.6.3 Monte Carlo Simulation of Mass Spectral Peaks

The first step in simulating mass spectral peaks by a Monte Carlo method was to generate the potential through which the ions travelled. Since the drift tube was a field-free region, the potential had only to be calculated for the ion extraction optics and for the part of the drift tube influenced by the deflection plates. The potential was generated by solving the Laplace equation numerically by a relaxation technique [19] and using as boundary conditions the copper box surrounding the acceleration region. More details can be found in Appendix A.

Figure 3.9 shows a potential map generated by the relaxation technique for the experimental extraction optics. It can be seen that the field between the repeller plate and draw-out plate is far from ideal and that the field-free region around the deflection plates is not field-free.

Figure 3.9 : Relaxed potential map with no guard rings. The map was generated with 250 V across the deflection plates and the contours are spaced by 50 V intervals.

Figure 3.9 : Relaxed Potential
with 250 V on the Deflection Plates

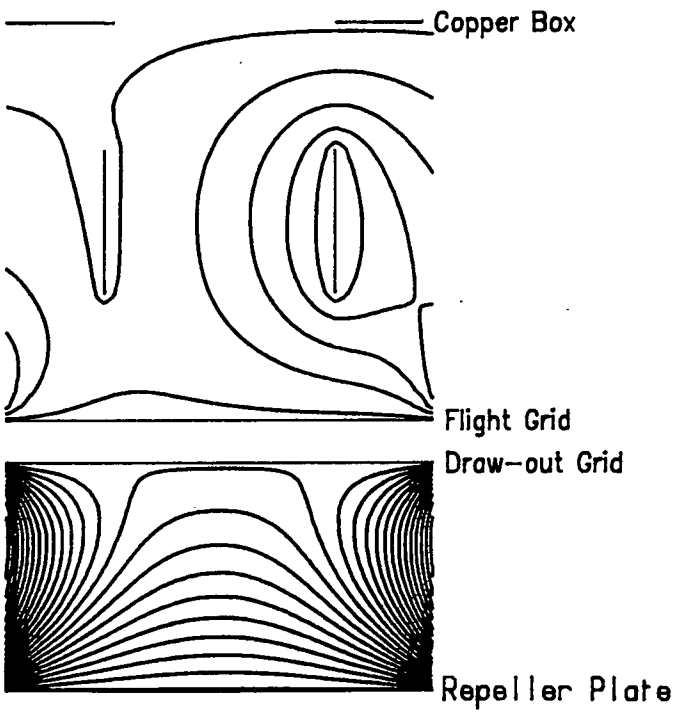

Before simulating trajectories on the above potential, the Monte Carlo method was tested on a potential with ideal electric fields and with no voltage across the deflection plates. These conditions matched the ones used in the analytical simulations. The spatial, velocity and temporal distributions used in all the Monte Carlo simulations were the same as those used in the analytical case. To reiterate, the spatial distribution was Gaussian with a FWHM of 1.0 mm, the velocities were distributed according to a one dimensional Boltzmann velocity distribution at 20 K and the temporal width of the photoionisation source was Gaussian with a FWHM of 10 ns. Figure 3.10 shows the simulated mass peaks obtained using the Monte Carlo method on the ideal potential for the spatial distribution alone, the velocity distribution alone, the temporal ionisation distribution alone and for all three distributions. Each peak was generated by following 40,000 ion trajectories and collecting each ion in the plane of the detector. The mass spectral widths and flight times calculated by the analytical and Monte Carlo methods agree to within 1 ns. The peak widths simulated for the spatial distributions alone are relatively least in agreement. As the peak widths increase, the discrepancy between the two methods remains constant, indicating that the discrepancy is a small correction rather than a relative difference. The discrepancy is probably due to two factors:

1) The potential map is generated on a grid with a mesh length of 2 mm and hence the plate positions can only be defined to such an accuracy. However, the peaks show that the potential is a good approximation to the analytical one.

2) Flight times through each cell of the grid are calculated to an accuracy better than 0.1 ns. Since in traversing the extraction region, ions have to pass through about 40 cells, the flight times could accumulate errors of up to approximately 4 ns. This extreme is not the case, but errors in flight times of approximately 1 ns could be due to this cause. Since peak width accuracy is not required to 1 ns, this

level of uncertainty is acceptable and is unlikely to distort any conclusion. The Monte Carlo method on an ideal potential agrees with the results of the analytical approach.

The power of the Monte Carlo method over the analytical approach is that it can readily take into account perturbations introduced by non-ideal fields and by the deflection plates. To fully define the problem, one more variable must be included, namely the position along the molecular beam axis at which the ion is formed. This distribution, known as the lateral distribution and given the symbol "l" was taken to be a 10 mm long strip centred on the TOFMS axis. The probability density function was further assumed to be a delta function of width 10 mm. In the case of ideal fields and no deflection plates, this variable has no effect on the peak widths.

Figure 3.11 shows the peak widths calculated on an ideal potential but with 250 V across the deflection plates. As expected the peak width most severely affected is the lateral peak width. However, the contribution of the broadened lateral peak to the final peak width is quite small and is insufficient to obtain agreement between the simulated and experimental peak widths. It appears, therefore, that the deflection plates only have a small effect on mass spectral peak widths. Although not shown in the figures, one effect of the deflection plates is to lengthen the ion flight times. The flight time for $^{98}Mo^{+}$ calculated analytically and on the ideal potential with 0 V across the deflection plates was 19.399 μs. The flight time on an ideal potential with 250 V across the deflection plates was 19.409 μs. The deflection plates thus present a potential barrier to the ions which lengthens the overall flight time.

Figure 3.10 : Monte Carlo simulations of the $^{98}Mo^{+}$ mass peak on an ideal potential with no voltage across the deflection plates.

Figure 3.10 : Monte Carlo
Simulations on an Ideal Potential

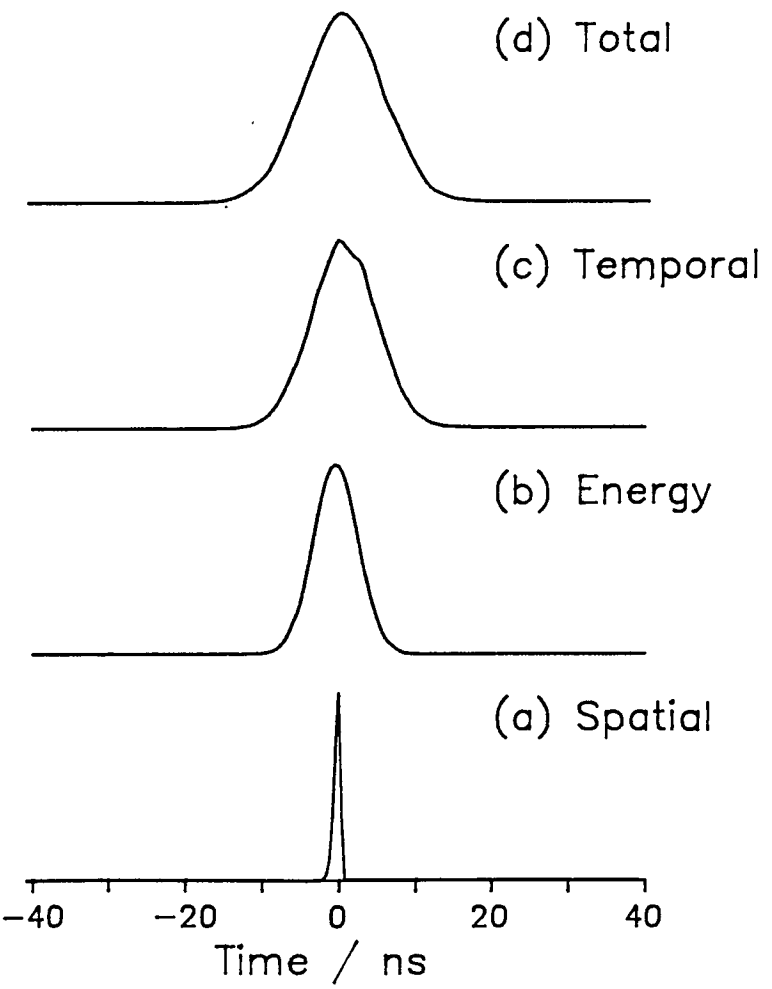

Figure 3.11 : Monte Carlo simulations of $^{98}Mo^{+}$ on an ideal potential with 250 V across the deflection plates.

Figure 3.11 : Monte Carlo Simulations on an Ideal Potential with Deflection Plates

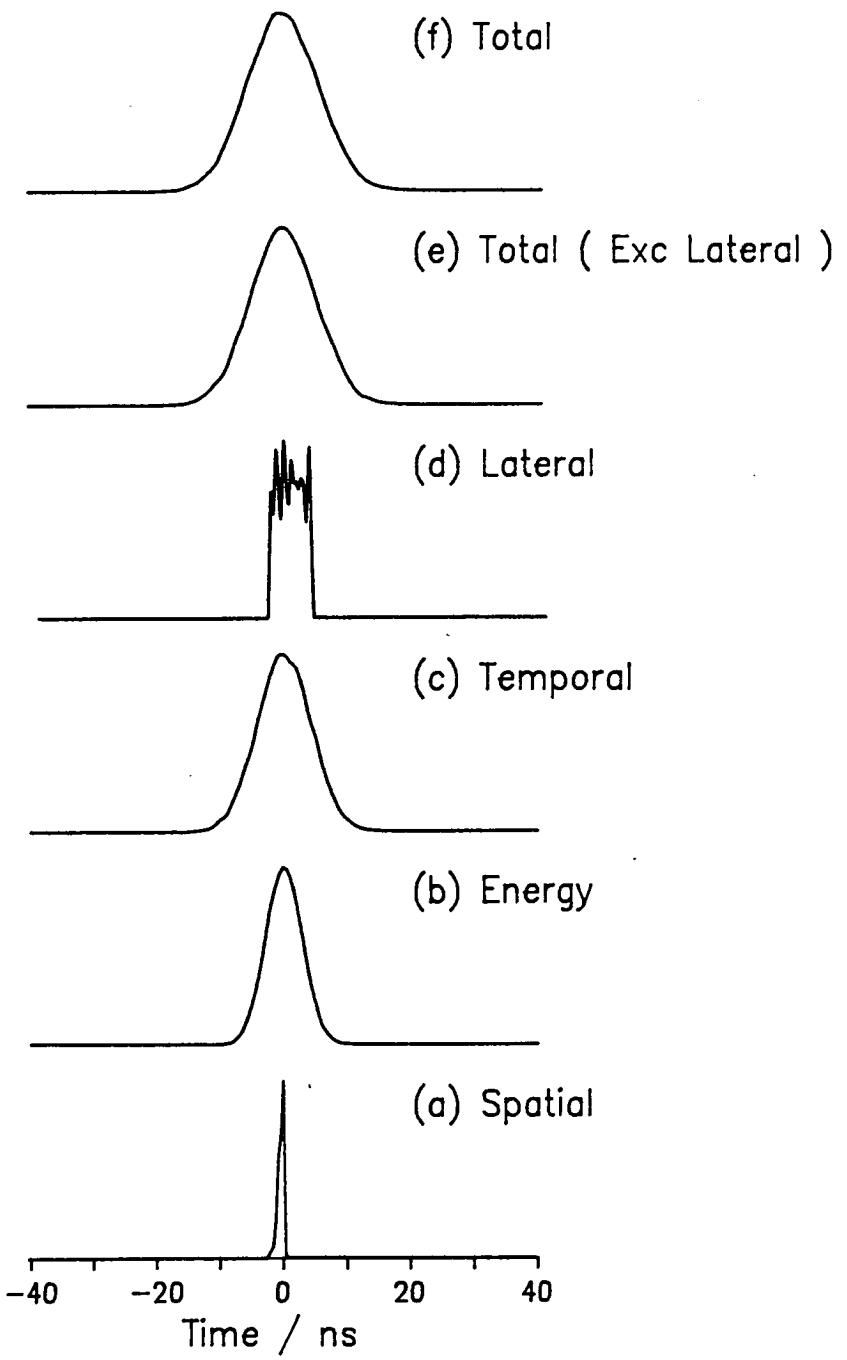

Figure 3.12 shows the effect of relaxing the potential and maintaining 250 V across the deflection plates. The effect is dramatic. The peak widths that depend on the position of the ion within the ion extraction optics - the spatial and lateral distributions - have broadened greatly and the simulated peak width is broader than the experimental one (Figure 3.7). This is in contrast to all previous simulations where the experimental peak was always broader. Equally important is the significant lengthening of the flight time from approximately 19.40 μs to 19.70 μs. From the potential map shown in Figure 3.9, the lengthened flight time and the broadening of the mass spectral peaks, it is clear that the electric field between the repeller and draw-out plates is not uniform and that the potential at any point is less than would have been predicted assuming uniform fields. With the relaxed potential, the Wiley and McLaren condition for spatial focusing is not met.

In contrast to the earlier simulations where the the peaks were simulated to a resolution of 1 ns, the simulations in Figure 3.12 were performed with a resolution of 10 ns. This was done to bring the simulation closer to the conditions used to record the experimental peak.

Simulations were also performed on a relaxed potential with 0 V across the deflection plates. There was essentially no change in the peak width or the flight time compared to the simulation performed with 250 V across the deflection plates. This confirmed that the distortions introduced by the deflection plates are very small compared to those introduced by the non-uniform electric fields.

Relaxing the potential resulted in a simulated peak width greater than the experimental peak width. However, the experimental peak width is generated by only those ions which strike the detector whereas the simulated peak was generated by collecting all ions in the plane of the detector. Figure 3.13 shows the simulated peak width generated by collecting only those ions which arrive in the detector

plane within one detector radius of the TOFMS axis. Immediately obvious is the reduction in the lateral peak width. Ions from large lateral displacements follow trajectories which either crash into the walls of the flight tube or miss the detector. It can also be seen that the overall peak width has decreased to a FWHM of 28 ns, comparing very favourably with the experimental peak of FWHM 26 ns. By placing a finite size on the detector and counting only those ions that strike the detector, the transmission function of the TOFMS can be estimated. Although only two dimensional, it is likely to be more realistic than that estimated by the analytical method. The percentage of ions with trajectories hitting the detector was 12 %. By including the grids through which the ions must pass to reach the detector, the transmission function can be estimated as approximately 8 %.

It is clear that it is the spread, Δs, and the non-uniform electric fields which most affect the peak width. The simplest way to improve the uniformity of the fields and hence reduce the peak width is to use guard rings. Figure 3.14 shows the potential generated using two guard rings between the repeller and draw-out plates, and Figure 3.15 shows a simulated mass peak for $^{98}Mo^{+}$ on this potential. The width of the spectral peak is significantly reduced, having a FWHM of only 12 ns, close to the limit set by the temporal width of the ionisation source. This width is equivalent to a resolution of approximately 810. The flight time calculated for the ion is 19.402 μs, only 3 ns longer than that calculated analytically or by Monte Carlo simulations on an ideal potential.

Figure 3.12 : Simulations on a relaxed potential collecting all ions in the plane of the detector.

Figure 3.12 : Monte Carlo Simulations on

a Relaxed Potential with Deflection Plates

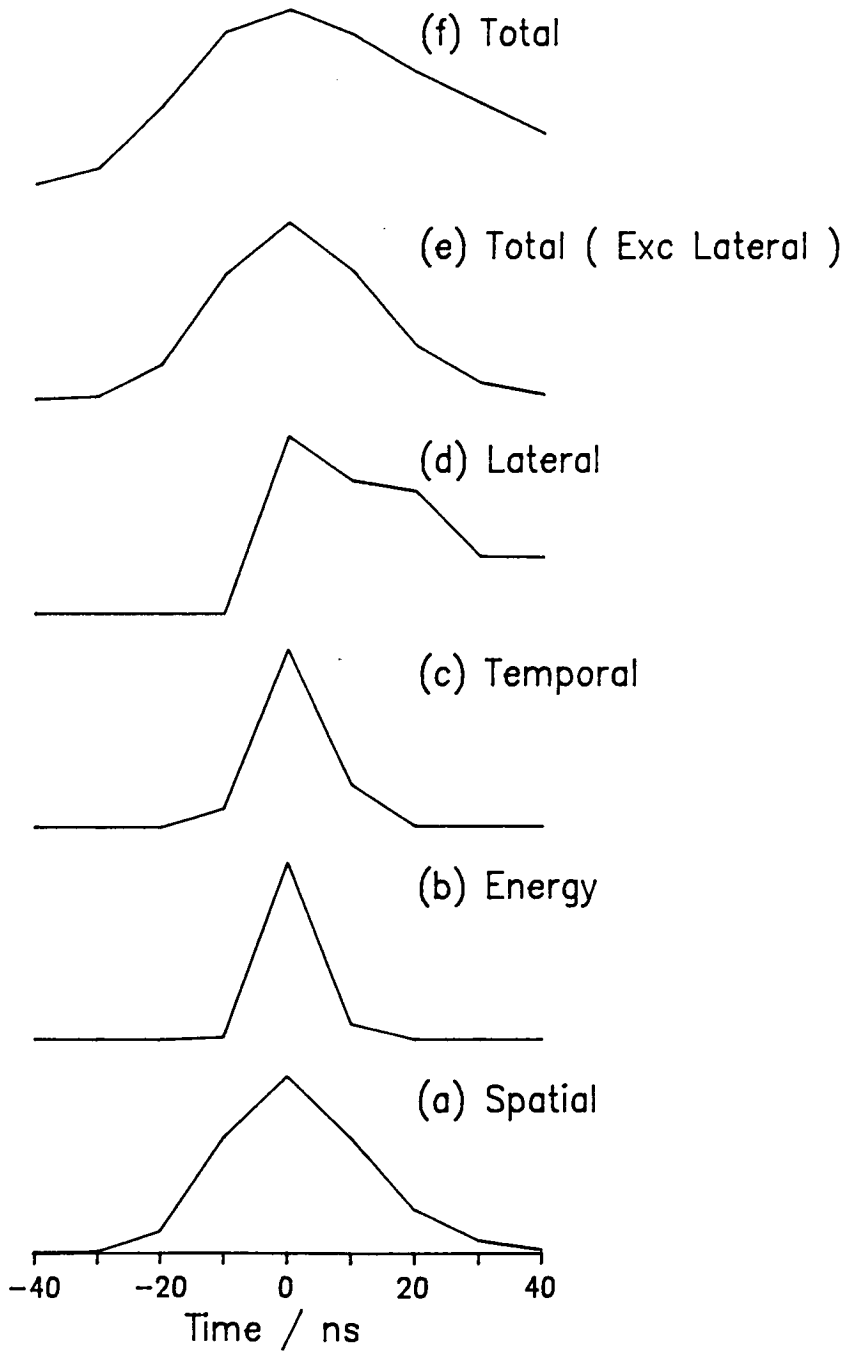

Figure 3.13 : Simulations on a relaxed potential collecting only those ions which hit a finite detector.

Figure 3.13 : Monte Carlo Simulations on

a Relaxed Potential with a Finite Detector

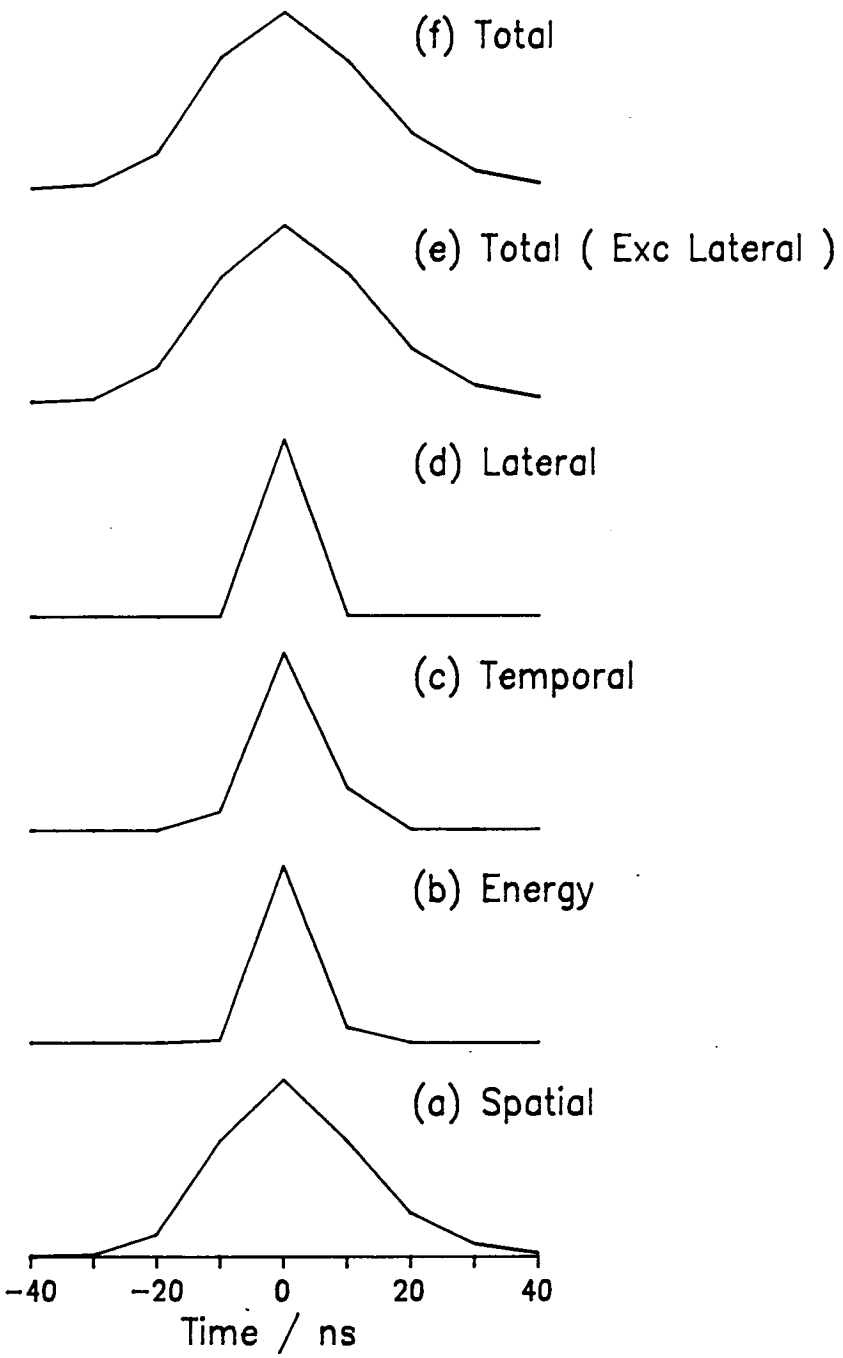

Figure 3.14 : Potential map generated using two guard rings between the repeller plate and the draw-out grid.

Figure 3.14 : Relaxed Potential With Guard Rings and 250 V across the Deflection Plates

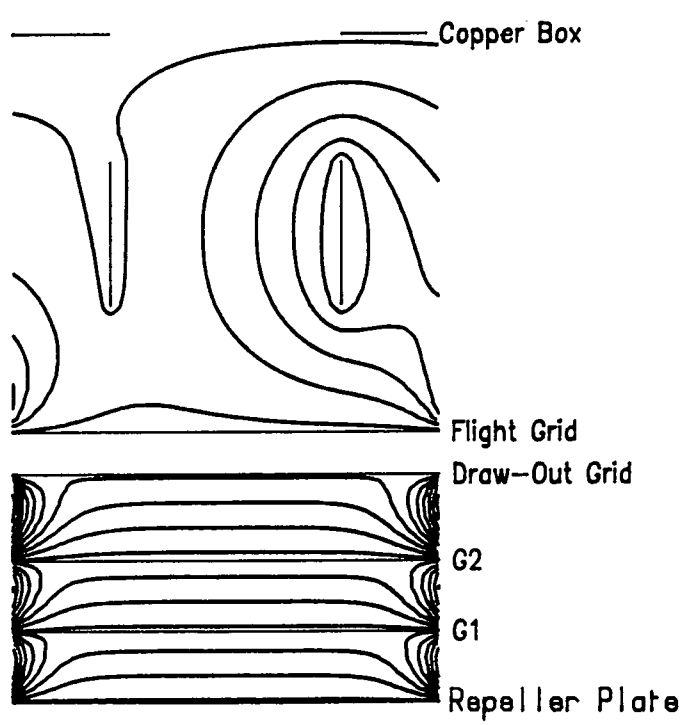

Figure 3.15 : Simulation on a relaxed potential with guard rings.

Figure 3.15 : Monte Carlo Peak Shape on a Relaxed Potential With Guard Rings

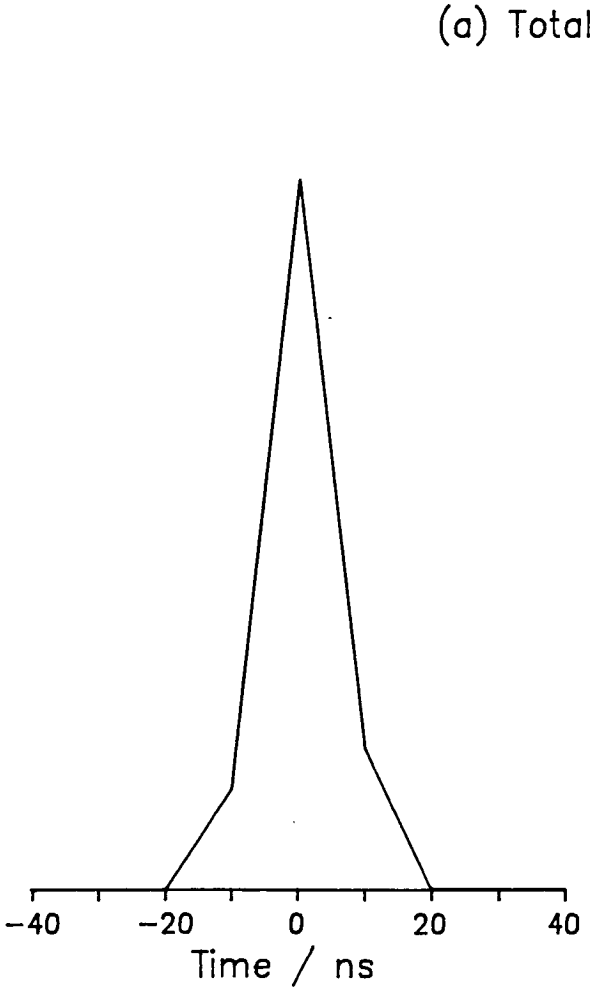

3.7 Conclusions

The Monte Carlo method offers a good way of simulating peak widths in a TOFMS and results close to experimental can be obtained. The ion transmission function of a TOFMS can also be estimated by collecting only those ions which hit a simulated detector. However, it has the disadvantage of being a computationally expensive method.

The simulations have shown the importance of uniform electric fields in attaining a high resolution. Unfortunately, one of the appeals of a TOFMS is the ease with which its open ion extraction optics can be coupled to a supersonic molecular beam with minimal interference to the molecular beam flow. The presence of the guard rings required to maintain uniform electric fields will possibly result in greater interaction between the molecular beam and the structure of the ion extraction optics. This could lead to collisional heating, fragmentation or loss of signal through increased collisions. The presence of the guard rings may also introduce further transmission grids with consequent loss of transmission.

It should be noted that the potential generated is 'probably worse than the experimental potential. This is because generation of the potential required boundary conditions and assumed that the copper box surrounding the extraction optics was complete (See Appendix A). This is not true as each wall in the copper box contained a 40 mm hole for the passage of the molecular beam or the photoionisation laser. Since the electric potential could penetrate through these holes, the potential near the centre of the extraction optics where photoionisation occurs would not have been dragged down as much as when calculated under assumption of no holes.

REFERENCES

1. D. Price and G. Milnes, Int. J. Mass Spectrom. Ion Phys., **60**, 61 (1984)

2. J.B. Farmer, *Mass Spectrometry*, Ed. C.A. McDowell, McGraw-Hill (1963)

3. M.S. Vries, N.J.A. Van Veen, T. Baller, and A.E. de Vries, Chem. Phys., **56**, 157 (1981)

4. D.H. Parker, *Ultrasensitive Laser Spectroscopy*, Ed. D.S. Kliger, Academic Press (1983)

5. R Larciprete and M. Stuke, J. Phys. Chem., **90**, 4568 (1986)

6. L.Q. Huang, R.J. Conzemius, G.A. Junk, and R.S. Houk, Anal. Chem., **60**, 1490 (1988)

7. B.A. Mamyrin, V.A. Karataev, D.V. Schmikk, and V.A. Zagulin. Sov. Phys., JETP **37**, 45 (1973)

8. W.C. Wiley, and I.H. McLaren, Rev. Sci. Instrum., **26**, 1150 (1955)

9. G. Sanzone, Rev. Sci. Instrum., **41**, 741 (1970)

10. P.W. Atkins, *Physical Chemistry*, Oxford University Press (1982)

11. J.P. Toennies and K. Winkelmann, J. Chem. Phys., **66**, 3965 (1977)

12. E.A. Rohlfing, D.M. Cox, and A. Kaldor, J. Chem. Phys. **81**, 3322 (1984)

13. E.A. Rohlfing, D.M. Cox, and A. Kaldor, J. Phys. Chem., **88**, 4497 (1984)

14. J.B. Hopkins, P.R.R. Langridge-Smith, M.D. Morse, and R.E. Smalley, J. Chem. Phys., **78**, 1627 (1983)

15. U. Boesl, H.J. Neusser, R. Weinkauf, and E.W. Schlag, J. Phys. Chem., **86**, 4857 (1982)

16. S.C. Richtsmeier, E.K. Parks, K. Liu, L.G. Pobo, and S.J. Riley, J. Chem. Phys., **82**, 3659 (1985)

17. R.B. Opsal, K.G. Owens, and J.P. Reilly, Anal. Chem., **57**, 1884 (1985)

18. R.E. Smalley, L. Wharton, and D.H. Levy, Acc. Chem. Res., **10**, 139 (1977)

19. W. Kaplan, *Advanced Mathematics for Engineers*, Addison-Wesley (1980)

CHAPTER FOUR

Spectroscopic Studies of the Lower Electronic States of Copper Dimer

4.1 Introduction

Copper dimer should offer the simplest example of the electronic spectroscopy of transition metal clusters [1]. It is the lightest member of the group of dimers formed from atoms with a closed shell of d-electrons and its spectra should be simpler than those of the heavier members of its group which have smaller rotational constants and, hence, more congested spectra. The closed d-shell and the related wide separation of the atomic terms results in a density of molecular states significantly lower than many of the other homonuclear transition metal dimers. For example, it has been calculated that 30 molecular states of Ni_2 lie within 1 eV of the ground state [2]. In contrast, no known excited electronic molecular states lie within 1 eV of the ground state of Cu_2.

There are also sound practical reasons for studying the low-lying excited electronic states of copper dimer. The transitions from the ground state occur in a convenient region for excitation with a dye laser and their spectroscopy is relatively well documented [3-13], compared to other transition metal dimers. However, the understanding of the electronic structure of Cu_2 provided by the previous body of work is not complete. A study of the electronic spectroscopy of Cu_2 therefore provided an opportunity to test the newly constructed experimental apparatus, described in Chapter II, with studies on well known systems and to perform new work on the less well known systems. The following section provides a review of previous experimental studies performed on the low-lying states of copper dimer.

4.2 Previous Experimental Work

The earliest observations of the emission spectrum of copper dimer were reported in 1954 by Kleman and Lindkvist [3] and Ruamps [4]. They observed vibrationally resolved emission in the blue and green. The green emission , the A → X system with its origin at 20,396 cm^{-1}, was the more extensive, but the blue emission, the B → X system with its origin at 21,748 cm^{-1}, appeared of dominating strength. Emission was observed from a furnace filled with 500 torr of argon [3], suggesting that the radiative process competes quite effectively against non-radiative processes.

Rotational resolution of the B-X system was achieved in 1965 by Aslund *et al* [11]. They conclusively showed that the B-X system corresponded to a $^1\Sigma$ - $^1\Sigma$ transition. By consideration of the atomic electronic configurations, the ground state was assigned to $^1\Sigma_g^+$ symmetry and the upper state to $^1\Sigma_u^+$ symmetry.

Pesic and Weniger [12], in 1971, performed a rotational analysis of the A-X system and assigned the A-state to $^1\Pi_u$ or 1_u symmetry. In a subsequent laser-induced fluorescence study, Lochet [13] observed only P and R branches forcing the symmetry of the A-state to be $^1\Sigma_u^+$ or 0_u^+.

Using a dc arc source to generate copper dimer, Rao and Rao [7] observed six band systems in the region 270 - 600 nm. Two systems could be assigned as emissions from the known A- and B-states and two matched observations reported from studies on the spectra of flames of copper salts [14]. These latter two had also tentatively been assigned to copper dimer. Rao and Rao vibrationally analysed the two new systems, one of which emitted to the ground state. This emission is now known as the E → X system and has an electronic origin at 27,136 cm^{-1}. The other emission did not terminate on the ground state and is therefore either

between two excited states of copper dimer or from a different spectral carrier.

Preuss *et al* [15], in 1979, identified a spectral feature approximately 100 cm^{-1} to the blue of the B-X origin. The authors were unable to perform a detailed study on this new feature since it appeared with approximately one-third to one-half of the intensity of the B-X system and, conceivably, half of the intensity could have been due to underlying B-X structure (the 5-4 band).

Powers *et al* [5] and Gole *et al* [16] simultaneously published the results of studies of Cu_2 seeded in an inert gas supersonic beam which confirmed that the spectral feature previously observed by Preuss [15] did indeed emanate from Cu_2. The electronic origin of the upper state, known as the C-state, was found to lie at 21,870 cm^{-1}. Powers *et al*, using R2PI, found the intensity of the 0-0 band of the C-X system to be approximately two and a half times that of the B-X system, in complete contrast to Preuss' earlier work. Powers *et al* also measured the lifetimes for the B- and C-states, obtaining values of 35 ± 10 ns and 1.0 ± 0.2 μs respectively. The conflict in the lifetime and intensity data was accounted for by stating that the B-state lifetime was shortened by predissociation.

Cu_2 has also been investigated trapped in inert gas matrices. Ozin *et al* [17] published results which suggested that when Cu_2 was trapped in argon, krypton or xenon matrices, the matrix induced shifts of the spectral transitions to the A- and B-states were large, approximately 5000 - 7000 cm^{-1} to the blue. Bondybey *et al* [6], however, found that the matrix-induced shift of the electronic transition energy for the A-X and B-X systems in a neon matrix was small. Bondybey *et al* performed a time resolved fluorescence emission study on the system excited at 26,000 cm^{-1} that Ozin had assigned to a strongly blue shifted A- (or B-) state. The emission from this system was long-lived with an estimated lifetime of approximately 6.5 μs. This is considerably longer than the matrix-isolated lifetimes

of either the A- or B-states, both of which have been measured as shorter than 10 ns [8].[18]. The state excited at 26,000 cm^{-1} in the neon matrix is known as the D-state. The intensity distribution of the emission from the D-state suggested that it was considerably less strongly bound than the A- and B-states.

Studies have also revealed information on the lifetimes and photoprocesses of the excited states. Steele [19] measured the lifetimes of several vibrational levels of the A- and B-states at a selection of buffer-gas pressures. The B-state lifetime, measured by monitoring laser-induced emission, was shorter than that of the A-state and in addition to the expected decrease in lifetimes with increasing buffer gas pressure, the B-state luminescence showed evidence at the higher pressures (10 torr of Ar) of a second longer-lived decay corresponding to the lifetime of the A-state.

In later work, Bondybey *et al* [20] measured the gas-phase lifetimes of the A-, B- and C-states. The lifetimes for the lowest three vibrational levels of the A-state were found to shorten rapidly with vibrational excitation but, in contrast to Steele's earlier work, were independent of helium pressure in the range 0.5 to 15 torr. The emissions from $v' = 3$ and $v' = 4$ levels appeared only weakly.

The lifetime of the C-state, in agreement with Gole's [16] work on the lowest three vibrational levels, was confirmed as being strongly dependent on pressure with an extrapolated zero pressure lifetime of 800 ± 100 ns. At high pressures, the Stern-Volmer plot became non-linear and at pressures above approximately 10 torr, the lifetime was found to level off near 100 ns.

The lifetimes of the lowest three vibrational levels of the B-state were found to be identical within experimental error, in agreement with Steele's [19] previous work. At higher pressures, the decay curves became doubly exponential with one

component shortening and one lengthening with respect to the 40 ns lifetime at lower pressures. By pressures of 10 - 12 torr, only the longer component survived. The longer component was identical to the lifetime of the C-state at similar pressures. Bondybey concluded that efficient collisional transfer between vibrational levels of the B- and C-states led to a joint decay of the two coupled levels.

Gole *et al* [16] complemented their gas-phase work on the A- and B-state lifetimes with studies on matrix-isolated dimers. In addition to fluorescence from the directly excited state, a second much stronger and longer-lived emission was also observed in the red and near infra red. This emission was attributed to the predissociation of either the A- or B-states followed by a cage recombination of the atoms to form the $^3\Sigma_u^+$ state correlating to the $^2S + {}^2S$ atomic limit. Further matrix work by Bondybey [8] on this long-lived emission in the red measured its lifetime as 27 ms and confirmed the assignment of the state as the lowest triplet state of Cu_2.

Work on the D → X system [6] showed that the emission was accompanied by stronger B-X fluorescence and by phosphorescence in the near IR (from the $^3\Sigma_u^+$ a-state). The measured lifetime of the B-state emission was long and it was clear that the B-state was populated indirectly via the higher lying D-state. No emission corresponding to the A-X system was observed even though B-X and a-X emissions were present. The true radiative lifetime of the D-state was estimated to be three or four times longer than that measured (6.5 μs) due to the above-mentioned photoprocesses shortening the measured lifetime.

There is no experimental data on the lifetime of the E-state.

4.3 Experimental Details of R2PI Spectroscopy

The overall description of the experimental apparatus and of cluster generation can be found in Chapter II. The details included here are specific to the two colour spectroscopic and lifetime studies on copper dimer.

The investigations were performed using frequency scans and time scans, both of which have been described previously. With either technique, channels from the transient digitiser corresponding to ions of a certain mass are selected and the ion signal recorded in these channels is monitored as a function of the laser wavelength (frequency scans) or of the time delay between excitation and ionisation of the molecule (time scans). A more detailed description has been presented in Chapter II.

4.3.1 Pump Laser

The first colour was provided by an excimer pumped dye laser (Lambda Physik). Two different dye solutions were required to cover the wavelength range. For the A-X system Coumarin 102 (range 460 - 510 nm) was used and for the B-X and C-X systems, Coumarin 47 (range 440 - 484 nm) was used. Line narrowing of the dye laser output was achieved through the use of an air spaced intracavity etalon with a free spectral range of 1 cm^{-1} [21] and a finesse of at least 25. The laser was capable of producing line narrowed tunable radiation with a bandwidth of approximately 0.04 cm^{-1}. The etalon was angle-tuned as the wavelength was scanned to maintain synchronisation between the peak of the profile transmitted by the grating and peak transmission of the etalon. The synchronised scanning of grating and etalon was under the control of a dedicated microprocessor and it was only necessary to locate the normal position of the etalon and one transmitted maximum as calibration points for the scanning program. The scan range was

limited to approximately 1 nm at the wavelengths used in these studies and the direction of scanning had always to be from red to blue. The former restriction caused no problems for spectra as compact as those generated from supersonically cooled copper dimer. However, the latter tended to be a nuisance with systems which formed a head at the blue end of the spectrum.

It was advantageous to pump the dye laser with a high energy excimer pump beam energy (200 mJ) and to reduce the dye laser output irradiating the Cu_2 sample with neutral density filters rather than to operate the dye laser with reduced pump beam. Typically, the dye laser beam energy was below 1 mJ $pulse^{-1}$ and was then further attenuated with neutral density filters of total optical density between 0.6 - 1.6 OD. Hence the energy of the dye beam was in the region 100 to 250 μJ $pulse^{-1}$. The beam diameter was apertured from approximately 8 mm to 3 mm and the approximate power density was 500 μJ cm^{-2} $pulse^{-1}$. No focusing was required or used.

4.3.2 Probe Laser

The second colour was provided by the Lumonics laser operating on argon fluoride. For temporal stability, this was operated at an energy of approximately 50 mJ $pulse^{-1}$ and was then attenuated by placing a series of metal grids between the laser and entrance window to the cluster apparatus. The grids served to reduce the power density from 6.4 mJ cm^{-2} $pulse^{-1}$ to approximately 400 μJ cm^{-2} $pulse^{-1}$.

Emission from this laser was both broadband and of sufficiently high energy (6.42 eV) not to have caused any distortions of the spectrum.

4.3.3 Alignment of the Lasers and Molecular Beam

The two laser beams were counterpropagating and crossed the molecular beam at right angles. To observe an R2PI signal, the problems of the spatial and temporal alignment of the pulsed beams had to be solved.

The first step in this process was the optimisation of cluster generation and detection. Optimisation of cluster generation involved tuning the focus and timing of the vaporisation laser (See Chapter II). The detection of the maximum number of dimer species was obtained by operating the ArF excimer laser at high energy and iteratively adjusting the height of the laser with respect to the molecular beam and the trigger to the laser with respect to the trigger to the molecular beam valve. Although cluster generation and detection are logically two separate operations, experimentally they are coupled. Hence the steps taken to maximise cluster generation had to be performed iteratively with the steps to maximise cluster detection.

Once the optimum signal had been observed using non-resonant photoionisation, the pump laser beam was introduced. The two laser beams were aligned spatially, and then temporally. The latter was achieved by splitting off small fractions from each beam and directing them to independent fast photodiodes whose outputs were monitored on an oscilloscope. For excited electronic states with short lifetimes, the constraints on temporal alignment could be quite severe. For example, to obtain a spectrum of the B-X system of Cu_2, the two lasers had to be aligned temporally to within 10 ns. The final adjustment of temporal alignment was performed iteratively whilst monitoring the signal of interest. With the spatial and temporal alignments completed, the correct probe laser wavelength was set and the ratio of the powers between the pump and probe lasers was adjusted to observe R2PI.

4.3.4 Adjustment of the Ratio of Laser Powers

Obtaining the correct ratio of powers was an empirical operation. To observe a spectral transition the probe laser beam power had to be attenuated so that most of the species in the probed volume were resonantly ionised. It was desired to operate with the maximum laser powers. The upper limit to the power of the pump laser was set by saturation effects broadening the spectral features and degrading the resolution. The upper limit to the power of the probe laser was set by the need to obtain sufficient contrast between the resonantly ionised signal and the non-resonant signal. In typical operation, the laser powers were selected such that the ratio of resonantly ionised signal (with the pump laser set at a wavelength near to a rotational head) to non-resonant signal (where the pump laser was set at a wavelength beyond a rotational head) was between eight and ten to one. Reduction of the probe laser power from this point led to particularly noisy spectra while an increase in pump laser power resulted in line broadening.

4.3.5 Number of Ions Generated

A good signal for resonant ionisation was a pulse approximately 320 mV in amplitude and 40 ns wide across a 50 Ω load. This corresponded to a charge of approximately 2.5×10^{-10} C, or 1.5×10^{9} electrons. The signal was the result of various stages of attenuation and amplification. From computer simulations (see Section 3.6.3), the transmission function of the TOFMS drift tube has been estimated as approximately 8 %. At the end of the drift tube the ions struck the microchannel plate detector, which provided between 10^5 - 10^6 amplification. The signal was further amplified by the preamplifier with a gain of between 10 - 100. The overall amplification of the ion signal between the point of generation and it reaching the digitiser was between 10^5 - 10^7, suggesting therefore that between 10^2 - 10^4 ions were produced by each laser pulse.

4.3.6 Spectral Calibration

Calibration was achieved by splitting-off a small fraction of the line-narrowed dye laser output and passing it through an air-spaced confocal etalon with a free spectral range (FSR) of 0.1 cm^{-1}. The transmitted light was monitored by a fast photodiode, the output of which was fed into a gated integrator. The output from the gated integrator was sampled by an ADC and subsequently stored in the computer.

4.4 Experimental Results

4.4.1 Low Resolution Spectroscopy of Cu_2

Figure 4.1 shows the spectrum of Cu_2 between 446 - 467 nm using a step size of 0.05 nm (approximately 2.4 cm^{-1}). The spectrum is dominated by the B-X and C-X systems of Cu_2. The C-X system appears with a much greater intensity than the B-X system in agreement with earlier R2PI studies [5]. However, caution must be observed not to assign too much significance to the experimentally measured intensities because of three factors.

i) The laser step size was large compared to its bandwidth and to the width of the spectral features. The maximum signal observed experimentally was not necessarily the result of the peak of the laser profile exciting the strongest transitions in the vibronic band.

ii) The timing between the trigger pulses to the pump and probe lasers was longer than optimum to prevent time drift between the two lasers completely losing the signal. This would have occurred if the probe laser preceded the pump laser. A longer time delay favoured observation of the state with the longer lifetime.

iii) The experiments were difficult to perform and shot-to-shot variations in the detected cluster signal were large. Even after averaging, the uncertainty in the intensity remained at between 10 - 25 %.

It was not possible to average more samples at each wavelength or to scan the laser with a smaller step size because of the long-term instability of the system. The spectrum illustrated in Figure 4.1 took approximately 30 minutes to run. To have scanned the range in laser bandwidth size steps would have taken approximately 3 hours, far too long for guaranteed experimental stability.

Figure 4.1 : Vibronic spectrum of the B-X and C-X systems of Cu_2. The spectrum was taken by scanning the dye laser from blue to red in 0.05 nm steps. Each point is the result of 30 laser shots. The ArF excimer laser was used to photoionise the excited species.

Figure 4.1 : Vibronically Resolved Spectrum of the B–X and C–X Systems of $^{63}Cu^{65}Cu$

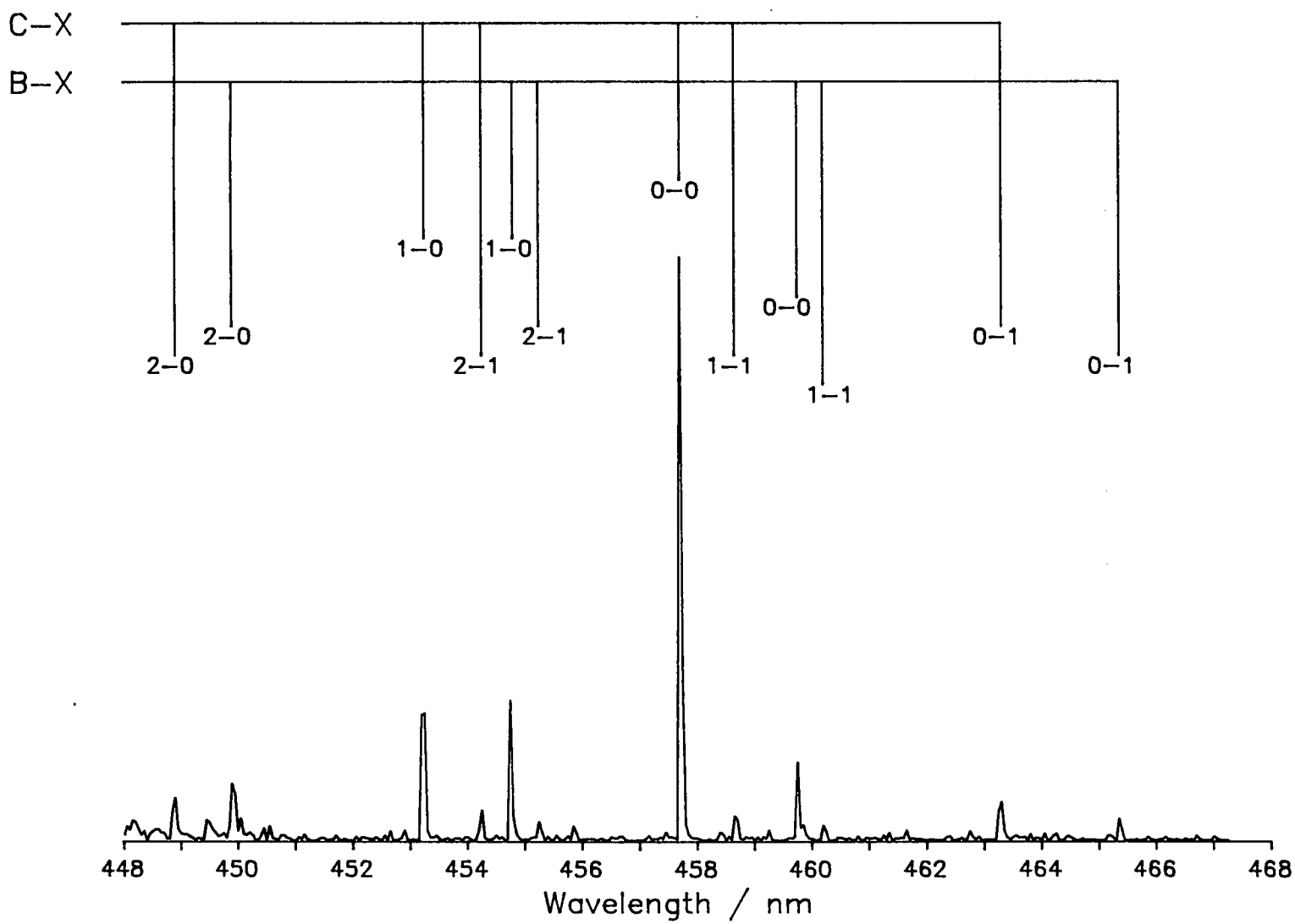

Figure 4.2 shows the spectrum of copper dimer over the range 492 - 485 nm and exhibits only several bands of the A-X system. The laser was stepped at approximately 1 cm^{-1}. A crude estimation of the vibrational temperature was obtained by comparing the intensities of the (0-0) and (1-0) bands to those of the (1-1) and (2-1) bands, after each band had been normalised by the appropriate Franck-Condon factor. The vibrational temperature obtained was 312 ± 160 K. The temperature illustrates the cooling effect of the supersonic expansion [22]. The dimers condense from the laser generated plasma and although the original vibrational temperature is unknown, it is estimated to be very high [23]. However, the expansion serves to cool the vibrational temperature to approximately ambient temperature. The narrowness of the bands in Figures 4.1 and 4.2 show that the rotational structure has been greatly collapsed through the cooling achieved in the supersonic expansion.

To fully appreciate this cooling and to determine any useful information regarding electronic state symmetries, the vibronic bands had to be investigated under greater resolution.

Figures 4.3 a-c show the origin bands of the A-X, B-X and C-X systems respectively obtained by scanning the dye laser without an intracavity etalon and with a step size of 0.001 nm (approximately 0.0045 cm^{-1}). The contours for the A-X and B-X systems appear to form heads at the blue end of the spectrum whereas the C-X contour shows less evidence of head formation and instead shows a relatively intense central band.

It was not possible to resolve the rotational structure lying beneath the contours without recourse to a higher resolution excitation source. This was provided by using the intracavity etalon in the Lambda Physik laser.

Figure 4.2 : Vibronic spectrum of the A-X system of Cu_2. The spectrum was acquired by scanning the dye laser from red to blue in 0.02 nm steps and averaging 30 laser shots at each point. Photoionisation of the excited species was achieved with the ArF excimer laser.

Figure 4.2 : Vibronic Spectrum of the A–X System of $^{63}Cu_2$

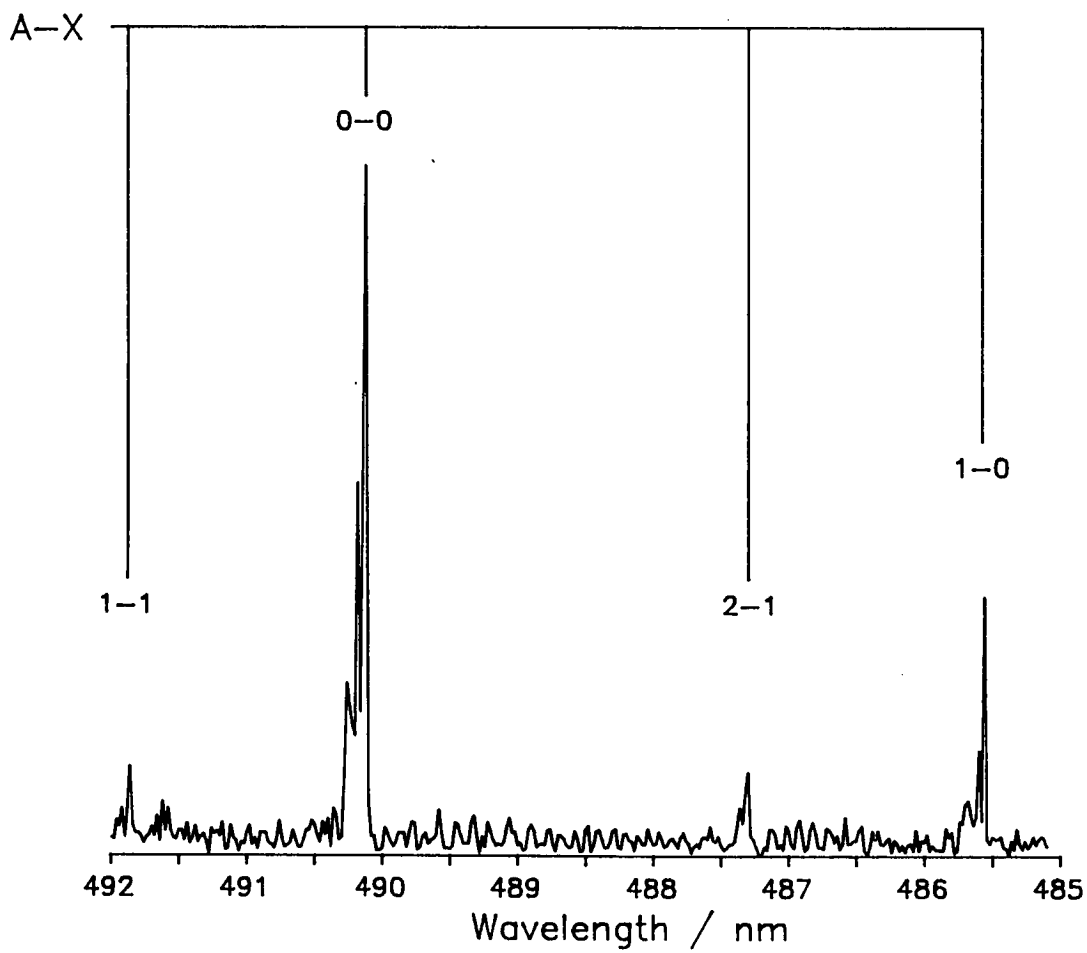

Figure 4.3 : Low resolution scans over the (0-0) bands of the A-X, B-X and C-X systems of Cu_2. The dye laser was scanned in 0.001 nm steps. For the B-X and C-X spectra, 50 laser shots were averaged at each point. The A-X spectrum was recorded by averaging 40 shots at each point. Photoionisation was achieved with the ArF excimer laser.

Figure 4.3 : Low Resolution Scans over the 0–0 bands of the A–X, B–X and C–X Systems of $^{63}Cu_2$

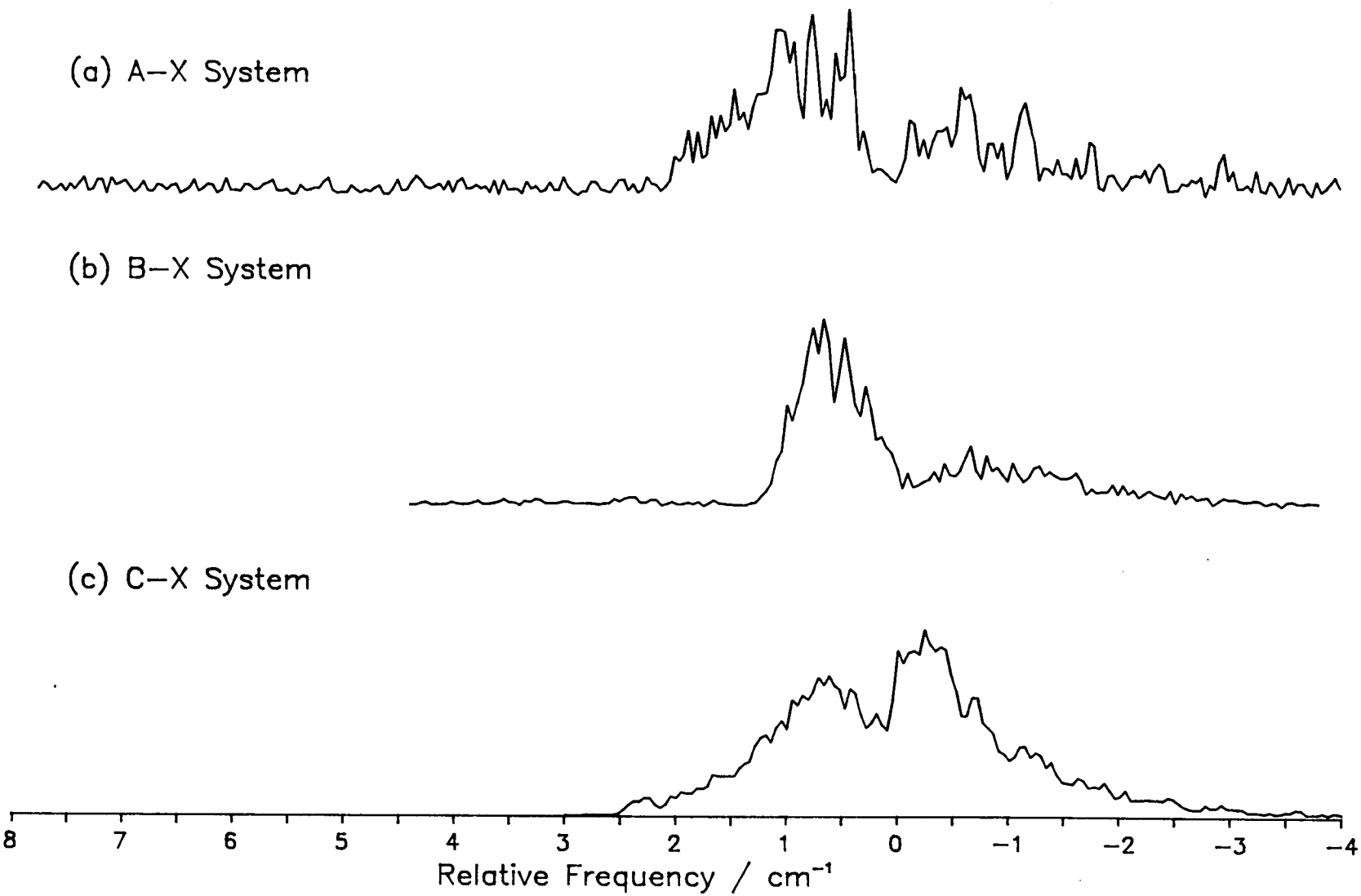

4.4.2 High Resolution Spectroscopy of Cu_2

4.4.2.1 A-X System

Figure 4.4a shows the high resolution spectrum of the (0-0) band of the A-X system of Cu_2 recorded using line narrowed output from the FL3002EC laser. The spectrum was obtained under the most severe expansion conditions (1 ms wide gas pulses from the NRC BV-100 valve operating with 10 bar backing pressure of He) and it is readily seen from the simulated spectrum in Figure 4.4b that the rotational structure has been strongly cooled. The details of spectral simulation are covered in Section 4.4.3.

To obtain more extensive rotational structure for a more accurate determination of the rotational constants, spectra were also recorded with attenuated expansion conditions. Figure 4.5a illustrates a hotter spectrum for the A-X system. The rotational temperature, as determined by simulation, is 18 K.

Several high resolution spectra were recorded for the (0-0) band of the A-X system at the attenuated expansion conditions. Each one was analysed and the rotational constants extracted. If the FSR of the etalon used to calibrate the spectra was treated as a fixed parameter, the spectroscopic constants extracted from one spectrum invariably differed from those extracted from another spectrum. However, the ratio of the upper state rotational constant to the lower state constant was, within experimental error, the same from spectrum to spectrum. The FSR of the monitor etalon was therefore treated as constant within a spectrum but as a variable parameter between spectra. Its value was determined by normalising the ground state rotational constant extracted from the data to the literature value [1]. After normalisation, the upper state constants extracted from the various spectra all agreed within experimental error. The spectroscopic

constants for the (0-0) band of the A-state listed in Table 4.6 are the average of 8 normalised spectra. The constants for the (1-0) band were extracted from a single spectrum. All isotopic combinations were fitted simultaneously and more details of the extraction of the spectroscopic constants from the the spectra are discussed in Section 4.4.4.

Table 4.7 shows the experimental line positions, the calculated line positions, and the residuals for a representative (0-0) band spectrum of the A-X system. Normalisation of the ground state spectroscopic constants in this spectrum to the literature value required the use of a FSR of 0.09964 cm^{-1}.

It is clear from the spectra illustrated in Figures 4.4a and 4.5a that the A-X system of Cu_2 consists of only parallel bands and the assignment of Lochet [13] is correct. The spectroscopic constants obtained for the upper state do not agree within experimental error with Lochet's, but it is believed that the constants quoted in this work are more correct than those reported by Lochet due to the larger number of lines analysed.

Figure 4.4 : Low temperature high resolution spectrum of the (0-0) band of the A-X System of Cu_2. The spectrum was taken using line narrowed radiation from the dye laser. Each point is the result of averaging 30 laser shots and the laser wavelength was scanned in 0.000294 nm steps. The spectrum was acquired using the most severe expansion conditions for the molecular beam.

Figure 4.4 : 0–0 Band of the A–X system of $^{63}Cu_2$

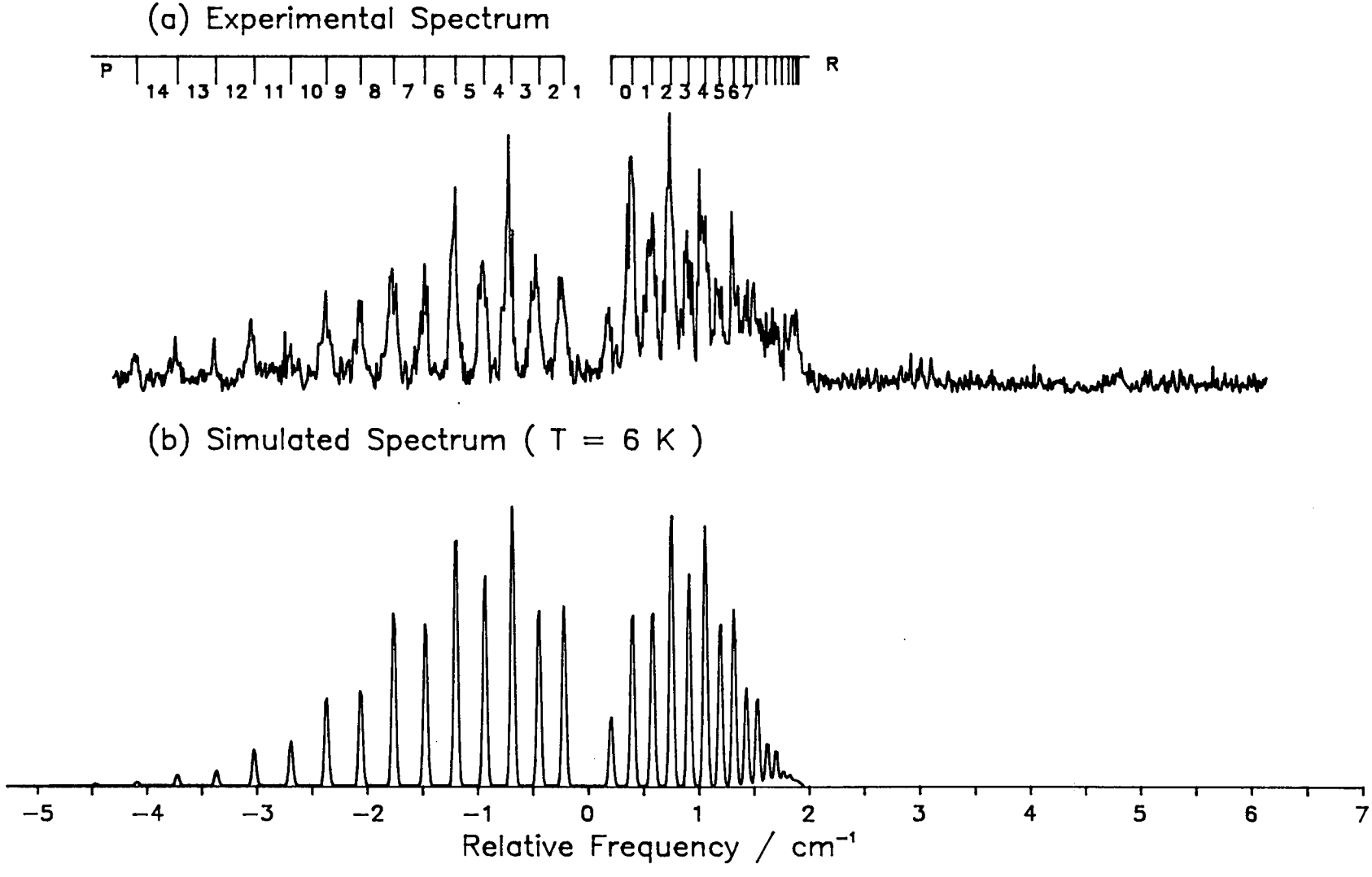

Figure 4.5 : High temperature high resolution spectrum of the (0-0) band of the A-X system of $^{63}Cu_2$. The conditions were as in Figure 4.4 except that milder expansion conditions were used, resulting in a rotationally warmer spectrum.

Figure 4.5 : 0–0 Band of the A–X system of $^{63}Cu_2$

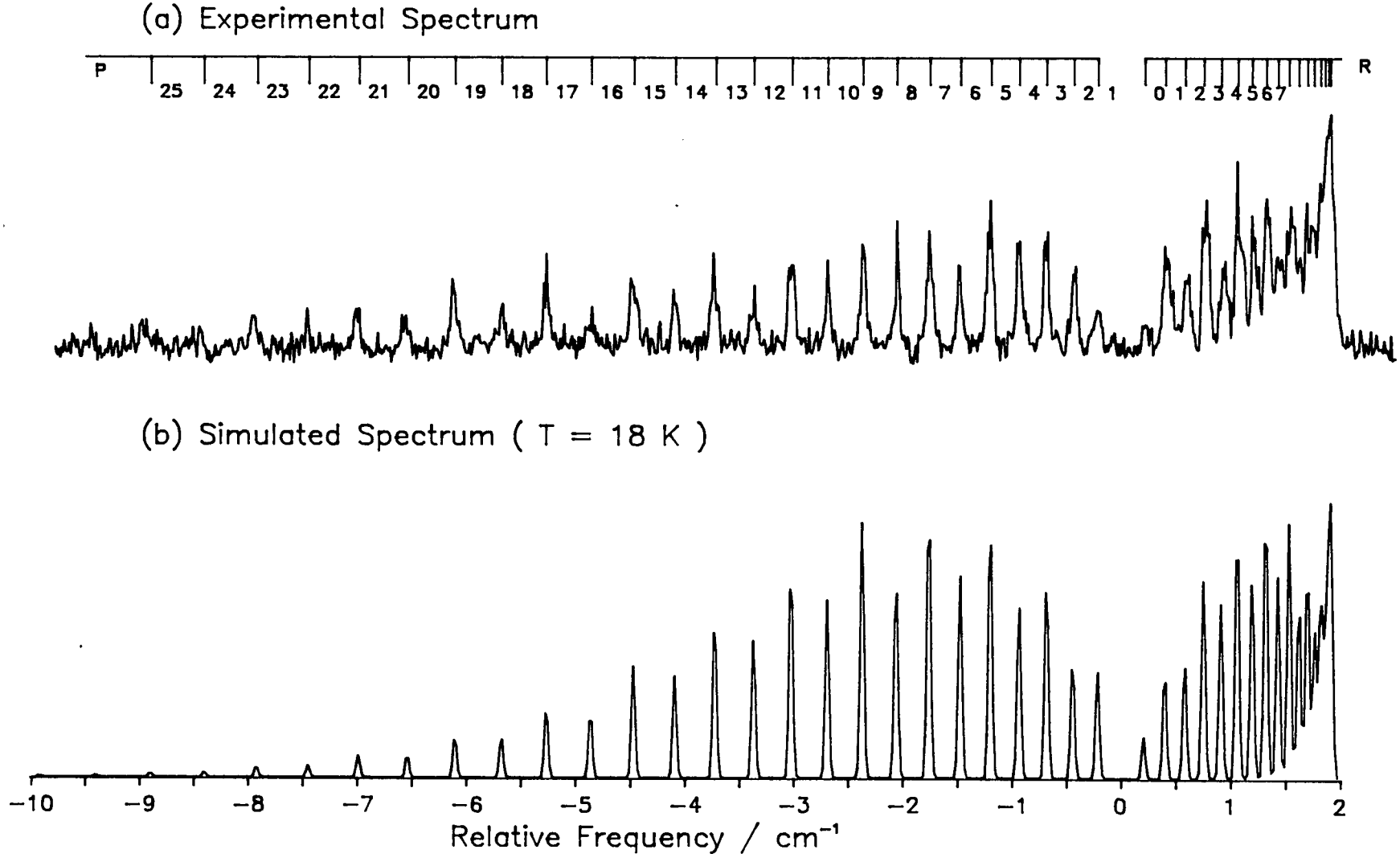

Table 4.6A : Rotational constants for selected vibrational levels of the A-, B- and C-states of $^{63}Cu_2$

STATE	v'	B_n / cm^{-1}	Error / cm^{-1}
A	0	0.102636	0.000069
A	1	0.10173	0.00037
B	0	0.09849	0.00044
C	0	0.104077	0.000048
C	1	0.10311	0.00010

Notes :

1) Each upper state rotational constant reported in the table is the result of averaging constants extracted from several spectra. Before averaging, the ground state rotational constants from the fit were normalised to the literature value of B''_e = 0.108433 cm^{-1}

2) The spectrum of the (1-0) band of the A-X system was courtesy of A.M. James.

Table 4.6B : Equilibrium Rotational Constants for the A- and C-states

STATE	B_e / cm^{-1}	Error / cm^{-1}	$\alpha_e \times 10^4$ / cm^{-1}	Error $\times 10^4$ / cm^{-1}
A	0.10309	0.00038	9.1	3.8
C	0.10456	0.00012	9.7	1.1

Table 4.7 : Rotational Line Positions for the 0-0 Band of the A-X System of Cu_2

$^{63}Cu_2$: Rotationless Origin = 0.000 ± 0.002 cm^{-1}

Branch	J″	Calc. / cm^{-1}	Obs. / cm^{-1}	Error / cm^{-1}	Resid. / cm^{-1}
P	16	-4.8621	-4.8593	0.0116	0.0028
P	15	-4.4712	-4.4637	0.0071	0.0074
P	14	-4.0919	-4.0974	0.0075	-0.0055
P	13	-3.7342	-3.7348	0.0083	-0.0106
P	12	-3.3681	-3.3677	0.0129	0.0004
P	11	-3.0236	-3.0244	0.0094	-0.0008
P	10	-2.6907	-2.6801	0.0091	0.0106
P	8	-2.0598	-2.0662	0.0064	-0.0064
P	7	-1.7617	-1.7655	0.0091	-0.0038
P	6	-1.4752	-1.4827	0.0098	-0.0075
P	5	-1.2003	-1.1984	0.0090	0.0019
P	4	-0.9371	-0.9302	0.0057	0.0069
P	3	-0.6854	-0.6889	0.0060	-0.0035
P	2	-0.4453	-0.4411	0.0085	0.0043
P	1	-0.2169	-0.2199	0.0069	-0.0031
R	0	0.2053	0.2024	0.0131	-0.0028
R	1	0.3989	0.4047	0.0052	0.0058
R	2	0.5810	0.5757	0.0077	-0.0053
R	3	0.7514	0.7571	0.0095	0.0057
R	5	1.0576	1.0524	0.0091	-0.0051

Table 4.7 (cont.)

$^{63}Cu^{65}Cu$: Rotationless Origin = 0.211 ± 0.002 cm^{-1}

Branch	J''	Calc. / cm^{-1}	Obs. / cm^{-1}	Error / cm^{-1}	Resid. / cm^{-1}
P	17	-4.9722	-4.9658	0.0112	0.0064
P	16	-4.5759	-4.5713	0.0128	0.0046
P	15	-4.1910	-4.1781	0.0092	0.0130
P	14	-3.8176	-3.8092	0.0072	0.0084
P	13	-3.4555	-3.4556	0.0091	-0.0001
P	12	-3.1049	-3.1089	0.0081	-0.0040
P	11	-2.7657	-2.7643	0.0044	0.0015
P	10	-2.4380	-2.4479	0.0058	-0.0100
P	9	-2.1216	-2.1263	0.0103	-0.0046
P	8	-1.8167	-1.8225	0.0078	-0.0058
P	7	-1.5232	-1.5244	0.0060	-0.0012
P	6	-1.2412	-1.2467	0.0111	-0.0055
P	5	-0.9705	-0.9592	0.0085	0.0113
P	4	-0.7113	-0.7043	0.0109	0.0070
P	3	-0.4635	-0.4511	0.0128	0.0124
P	1	-0.0022	-0.0198	0.0121	-0.0177
R	0	0.4134	0.4235	0.0123	0.0101
R	1	0.6041	0.6063	0.0069	0.0022
R	2	0.7834	0.7921	0.0110	0.0087
R	3	0.9512	0.9608	0.0112	0.0096
R	4	1.1076	1.0989	0.0066	-0.0087
R	5	1.2526	1.2385	0.0109	-0.0141

Table 4.7 (cont.)

$^{65}Cu_2$: Rotationless Origin = 0.432 ± 0.002 cm^{-1}

Branch	J"	Calc. / cm^{-1}	Obs. / cm^{-1}	Error / cm^{-1}	Resid. / cm^{-1}
P	17	-4.6706	-4.6690	0.0211	0.0015
P	15	-3.9016	-3.9051	0.0106	-0.0035
P	14	-3.5340	-3.5511	0.0120	-0.0171
P	13	-3.1776	-3.1721	0.0148	0.0055
P	12	-2.8325	-2.8340	0.0132	-0.0015
P	11	-2.4986	-2.5063	0.0101	-0.0077
P	10	-2.1760	-2.1766	0.0130	-0.0007
P	9	-1.8646	-1.8735	0.0140	-0.0089
P	7	-1.2755	-1.2813	0.0181	-0.0058
P	6	-0.9978	-0.9906	0.0148	0.0073
P	5	-0.7314	-0.7339	0.0076	-0.0024
P	4	-0.4763	-0.4750	0.0079	0.0013
P	3	-0.2323	-0.2223	0.0066	0.0100
P	2	0.0003	0.0014	0.0140	0.0010
P	1	0.2218	0.2140	0.0156	-0.0078
R	0	0.6309	0.5999	0.0237	-0.0310
R	1	0.8186	0.8337	0.0106	0.0151
R	2	0.9951	1.0044	0.0158	0.0093
R	3	1.1603	1.1507	0.0111	-0.0096
R	4	1.3143	1.3428	0.0385	0.0285
R	5	1.4570	1.4563	0.0080	-0.0007
R	6	1.5885	1.5964	0.0686	0.0079
R	7	1.7087	1.7178	0.0304	0.0091

Normalised constants derived from spectrum ($^{63}Cu_2$)

B'_0 = 0.10263 ± 0.00018 cm^{-1}

B''_0 = 0.10843 ± 0.00016 cm^{-1} (FSR = 0.09964 cm^{-1})

Chi-squared = 41.94 with 60 degrees of freedom

Reduced Chi-squared = 0.70

4.4.2.2 B-X System

Figure 4.8a illustrates a high resolution scan recorded over the (0-0) band of the B-X system of Cu_2. Figure 4.8b illustrates a simulation of the spectrum for a rotational temperature of 18 K. The spectroscopic constants extracted from the data are listed in Table 4.6 and are the result of averaging the normalised constants from two spectra.

Table 4.9 shows the experimental line positions, the calculated line positions and the residuals for a spectrum of (0-0) band of the B-X system. Normalisation of the ground state constant to the known literature value yielded an etalon FSR of 0.10036 cm^{-1}.

The spectroscopic constants listed in Table 4.9 are in agreement with those published by Aslund *et al* [11] and confirm that the electronic symmetry of the B-state is either $^1\Sigma_u^+$ or 0_u^+.

Figure 4.8 : High resolution spectrum of the (0-0) band of the B-X system of Cu_2. The spectrum was acquired by scanning the line narrowed output from the dye laser in 0.000273 nm steps. Each point in the spectrum is the average of 30 laser shots. Photoionisation was achieved with the ArF laser.

Figure 4.8 : 0–0 Band of the B–X system of $^{63}Cu_2$

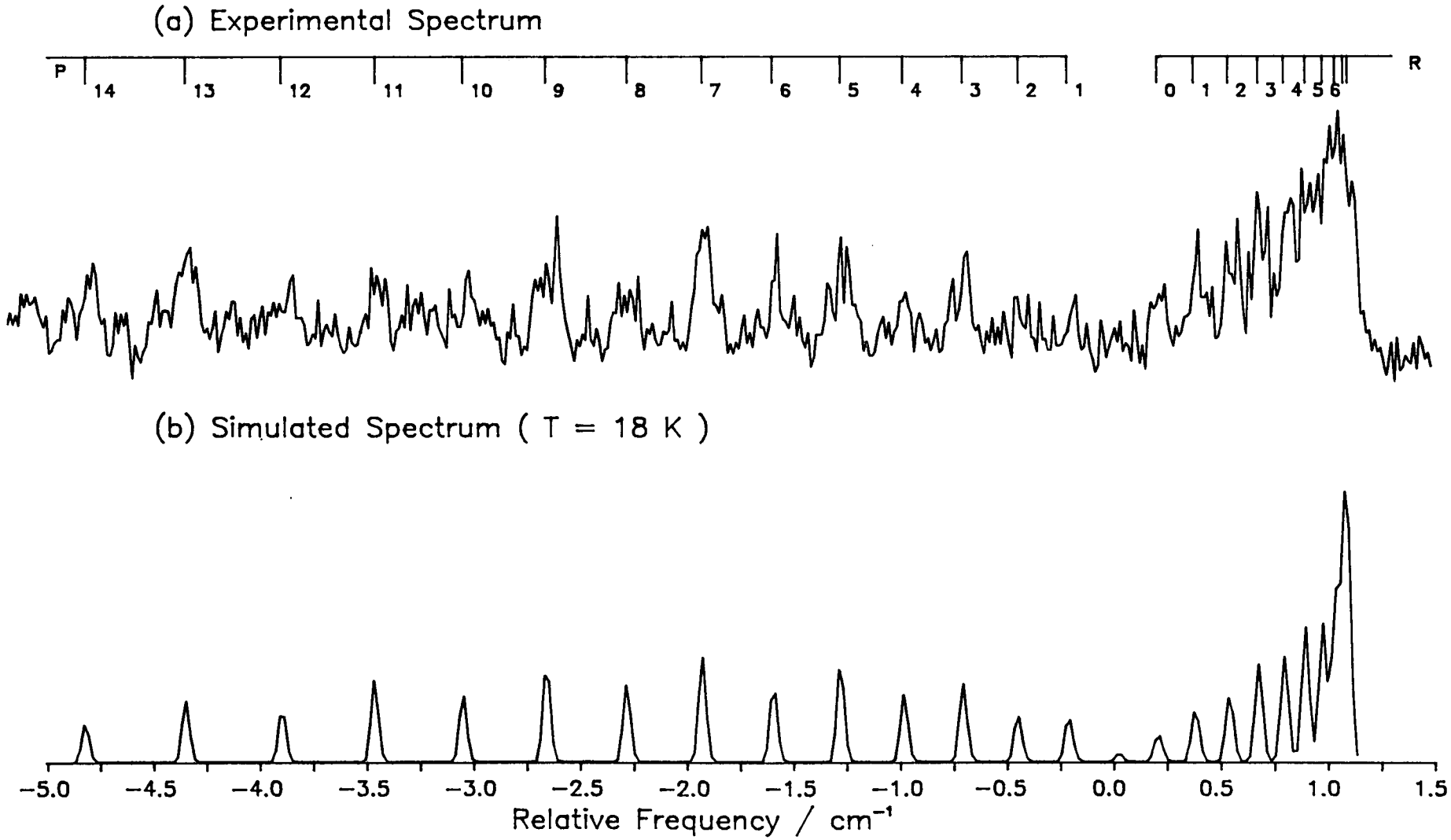

Table 4.9 : Line Positions for the 0-0 Band of the B-X System of Cu_2

$^{63}Cu_2$: Rotationless Origin = 0.000 ± 0.003 cm^{-1}

Branch	J"	Calc. / cm^{-1}	Obs. / cm^{-1}	Error / cm^{-1}	Resid. / cm^{-1}
P	13	-4.3741	-4.3827	0.0073	-0.0085
P	12	-3.9180	-3.8947	0.0199	0.0234
P	11	-3.4818	-3.4787	0.0189	0.0032
P	9	-2.6693	-2.6610	0.0106	0.0083
P	8	-2.2929	-2.2988	0.0190	-0.0059
P	7	-1.9365	-1.9411	0.0073	-0.0046
P	6	-1.6000	-1.6054	0.0079	-0.0053
P	5	-1.2835	-1.2783	0.0200	0.0052
P	4	-0.9869	-0.9802	0.0264	0.0066
P	3	-0.7101	-0.7174	0.0121	-0.0072
P	2	-0.4534	-0.4544	0.0246	-0.0009
P	1	-0.2166	-0.2038	0.0123	0.0129
R	0	0.1972	0.1951	0.0081	-0.0021
R	1	0.3742	0.3759	0.0184	0.0018
R	2	0.5312	0.5605	0.0141	0.0293
R	3	0.6683	0.6782	0.0188	0.0099

Table 4.9 (cont.)

$^{63}Cu^{65}Cu$: Rotationless Origin = 0.021 ± 0.002 cm^{-1}

Branch	J″	Calc. / cm^{-1}	Obs. / cm^{-1}	Error / cm^{-1}	Resid. / cm^{-1}
P	14	-4.7552	-4.7484	0.0195	0.0068
P	13	-4.2865	-4.2900	0.0646	-0.0036
P	12	-3.8374	-3.8580	0.0125	-0.0207
P	11	-3.4079	-3.3844	0.0239	0.0235
P	10	-2.9981	-2.9830	0.0178	0.0151
P	9	-2.6079	-2.6219	0.0223	-0.0140
P	8	-2.2373	-2.2299	0.0083	0.0075
P	7	-1.8864	-1.8849	0.0142	0.0015
P	6	-1.5551	-1.5499	0.0148	0.0051
P	5	-1.2434	-1.2350	0.0098	0.0084
P	4	-0.9513	-0.9400	0.0131	0.0113
P	3	-0.6789	-0.6787	0.0095	0.0002
P	2	-0.4261	-0.4215	0.0209	0.0046
P	1	-0.1930	-0.1987	0.0167	-0.0057
R	0	0.2145	0.1902	0.0140	-0.0242
R	1	0.3887	0.3868	0.0031	-0.0019
R	3	0.6784	0.7059	0.0230	0.0276
R	4	0.7938	0.8424	0.0341	0.0486

Table 4.9 (cont.)

$^{65}Cu_2$: Rotationless Origin = 0.044 ± 0.004 cm^{-1}

Branch	J″	Calc. / cm^{-1}	Obs. / cm^{-1}	Error / cm^{-1}	Resid. / cm^{-1}
P	15	-5.1378	-5.1203	0.0147	0.0175
P	14	-4.6571	-4.6750	0.0104	-0.0179
P	13	-4.1957	-4.1948	0.0123	0.0010
P	12	-3.7537	-3.7419	0.0111	0.0117
P	11	-3.3309	-3.3143	0.0120	0.0166
P	10	-2.9275	-2.9434	0.0212	-0.0160
P	9	-2.5434	-2.5766	0.0713	-0.0332
P	8	-2.1786	-2.1399	0.0234	0.0387
P	7	-1.8331	-1.8323	0.0060	0.0009
P	6	-1.5070	-1.5068	0.0159	0.0002
P	5	-1.2002	-1.2071	0.0165	-0.0069
P	4	-0.9127	-0.9127	0.0131	0.0000
P	3	-0.6426	-0.6533	0.0119	-0.0088
P	2	-0.3957	-0.4110	0.0140	-0.0153
P	1	-0.1662	-0.1722	0.0176	-0.0060

Normalised constants from spectrum ($^{63}Cu_2$)

B'_0 = 0.09847 ± 0.00039 cm^{-1}

B''_0 = 0.10843 ± 0.00033 cm^{-1} (FSR = 0.10036 cm^{-1})

Chi-squared = 37.97 with 44 degrees of freedom

Reduced Chi-squared = 0.863

4.4.2.3 C-X System

Figure 4.10a illustrates a high resolution scan over the (0-0) band of the C-X system of Cu_2. It is immediately obvious from the spectrum that the transition is perpendicular, in contrast to the A-X and B-X systems. Figure 4.10b illustrates a simulation of this spectrum using a rotational temperature of 5 K. The spectrum in Figure 4.10a was obtained using the most severe expansion conditions.

The spectroscopic constants derived for the C-state are listed in Table 4.6. The constants for the (0-0) band were obtained by averaging the normalised constants from five spectra. The constants for the (1-0) band were extracted from one spectrum.

A hot spectrum of the (1-0) band of the C-X system is shown is Figure 4.11a. Table 4.12 shows experimental line positions, calculated line positions, and residuals for a representative hot spectrum of the (0-0) band of the C-X system. An etalon FSR of 0.100028 cm^{-1} was required to normalise the spectrum. The C-state can be assigned either to a state of Π_u electronic symmetry in Hund's case (a) or of 1_u electronic symmetry in Hund's case (c). This is the first assignment of the electronic symmetry of the C-state.

Figure 4.10 : Low temperature high resolution spectrum of the (0-0) band of the C-X System of Cu_2. The spectrum was obtained using the most extreme expansion conditions of the molecular beam. The intracavity etalon was installed in the dye laser to line narrow the output. Each point is the result of 30 laser shots and the scan step size was 0.000276 nm. Photoionisation was achieved with the ArF excimer laser.

Figure 4.10 : 0–0 Band of the C–X system of $^{63}Cu_2$

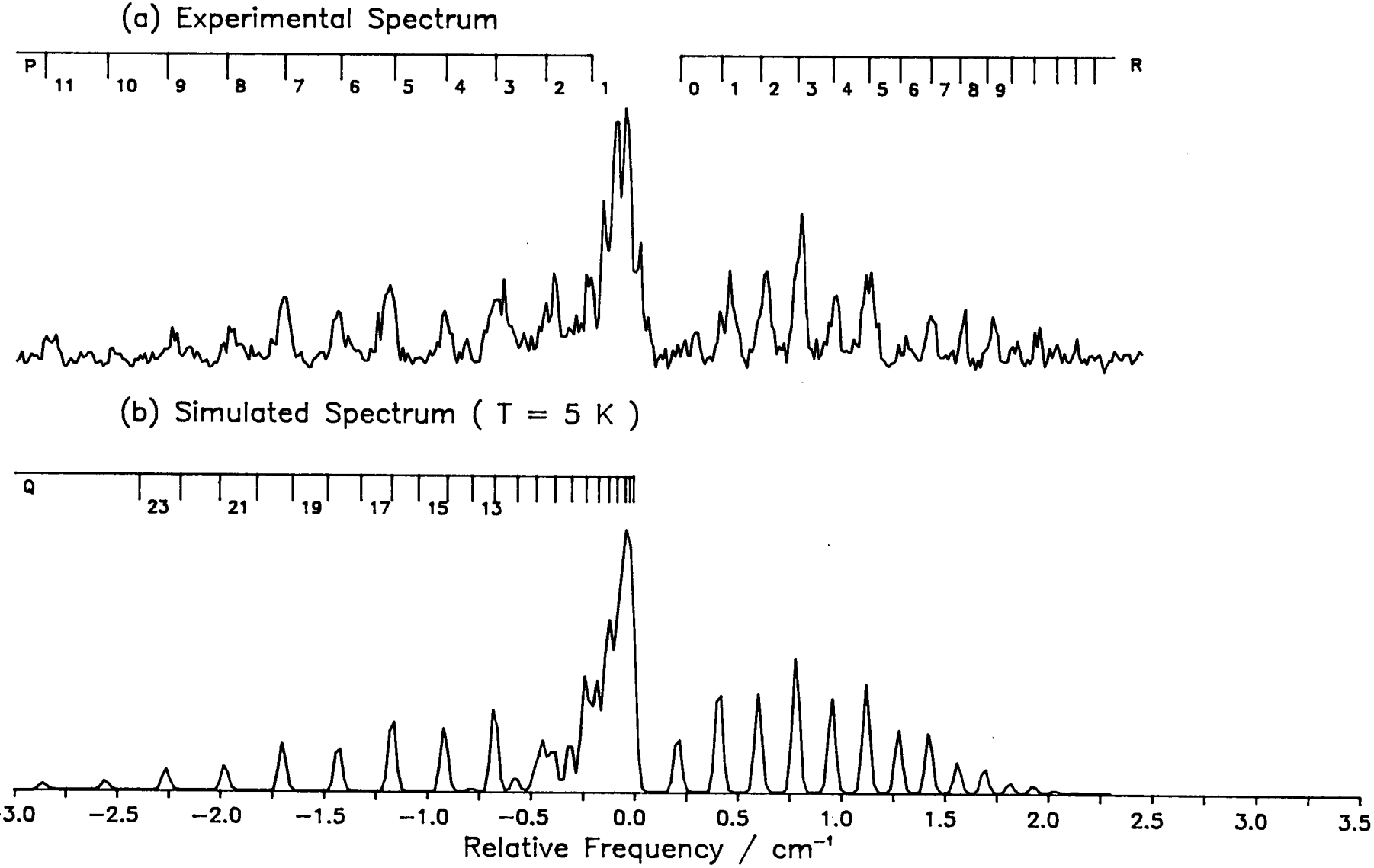

Figure 4.11 : High temperature high resolution spectrum of the (1-0) band of the C-X System of Cu_2. The spectrum was acquired using milder beam expansion conditions than used in acquiring the spectrum shown in Figure 4.10. Each point is the average of 30 laser shots and the scan step size was 0.000272 nm. Photoionisation was achieved with the ArF excimer laser.

Figure 4.11 : 1−0 Band of the C−X system of $^{63}Cu_2$

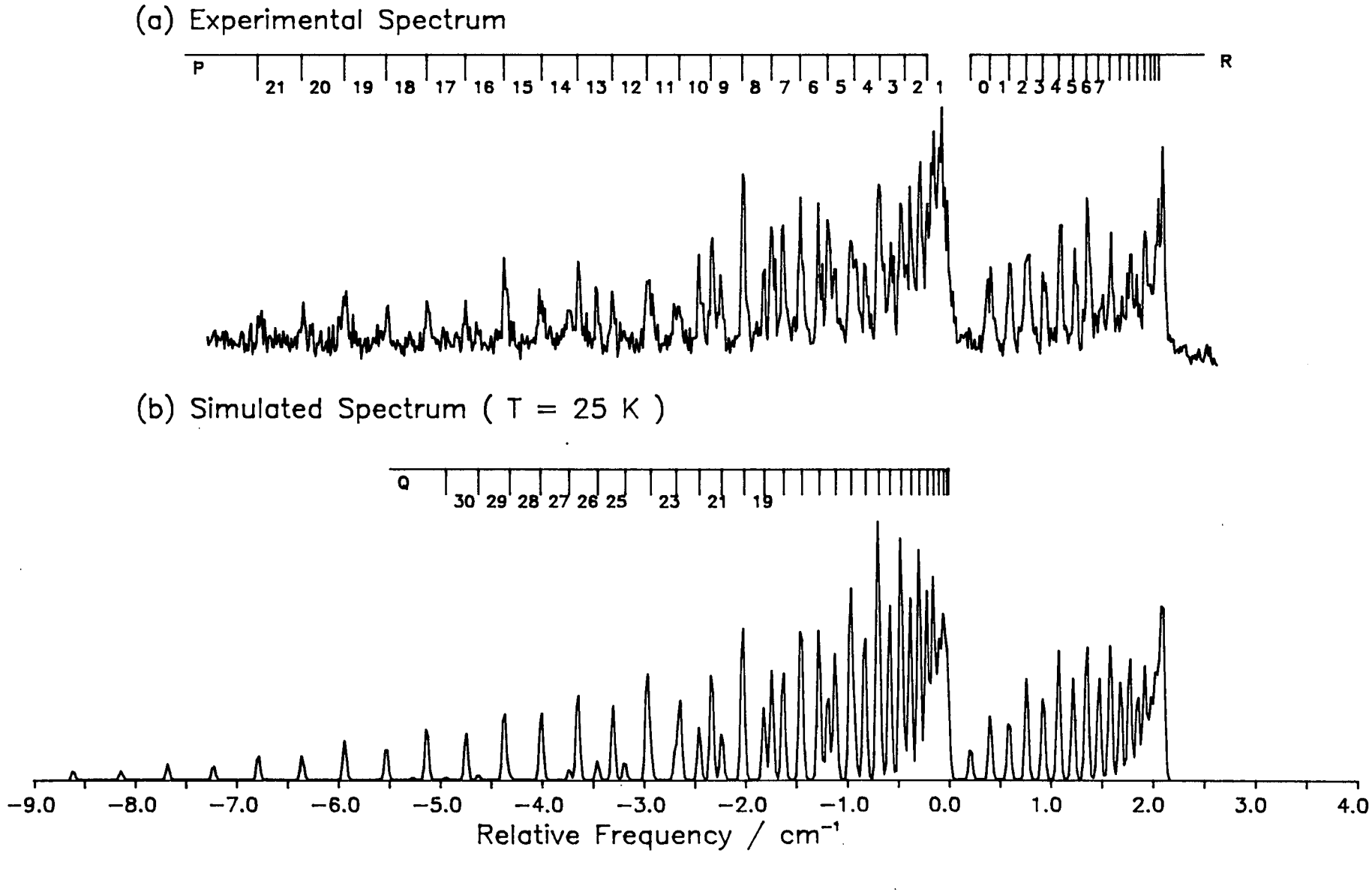

Table 4.12 : Line Positions for the 0-0 Band of the C-X System of Cu_2

$^{63}Cu_2$: Rotationless Origin = 0.000 ± 0.002 cm^{-1}

Branch	J"	Calc. / cm^{-1}	Obs. / cm^{-1}	Error / cm^{-1}	Resid. / cm^{-1}
P	23	-7.2069	-7.1895	0.0078	0.0174
P	21	-6.3959	-6.3808	0.0121	0.0150
P	20	-6.0036	-5.9585	0.0234	0.0450
P	19	-5.6200	-5.6135	0.0194	0.0065
P	18	-5.2452	-5.2585	0.0244	-0.0132
P	17	-4.8792	-4.8986	0.0204	-0.0194
P	16	-4.5220	-4.5326	0.0066	-0.0106
P	15	-4.1735	-4.1766	0.0115	-0.0031
P	14	-3.8338	-3.8345	0.0160	-0.0007
P	13	-3.5029	-3.4977	0.0112	0.0052
P	12	-3.1808	-3.1646	0.0138	0.0162
P	11	-2.8674	-2.8735	0.0103	-0.0061
P	10	-2.5628	-2.5708	0.0161	-0.0079
Q	23	-2.4207	-2.4138	0.0128	0.0069
P	9	-2.2670	-2.2578	0.0148	0.0092
P	8	-1.9799	-1.9796	0.0318	0.0003
P	7	-1.7016	-1.7024	0.0090	-0.0008
P	6	-1.4321	-1.4231	0.0226	0.0090
P	5	-1.1714	-1.1773	0.0115	-0.0059
Q	15	-1.0521	-1.0607	0.0047	-0.0086
P	4	-0.9194	-0.9323	0.0131	-0.0128
Q	13	-0.7977	-0.8091	0.0093	-0.0114
Q	9	-0.3941	-0.4002	0.0121	-0.0061
R	1	0.4081	0.4131	0.0113	0.0050
R	2	0.5986	0.5925	0.0091	-0.0061
R	3	0.7804	0.7860	0.0167	0.0056
R	4	0.9534	0.9617	0.0112	0.0083
R	5	1.1176	1.1218	0.0108	0.0041
R	6	1.2731	1.2771	0.0125	0.0040
R	7	1.4198	1.4298	0.0120	0.0101
R	8	1.5577	1.5574	0.0087	-0.0003
R	9	1.6868	1.6886	0.0228	0.0018
R	11	1.9188	1.9268	0.0107	0.0080
R	12	2.0216	2.0360	0.0108	0.0144
R	13	2.1156	2.1254	0.0185	0.0098

Table 4.12 (cont.)

$^{63}Cu^{65}Cu$: Rotationless Origin = 0.146 ± 0.002 cm^{-1}

Branch	J"	Calc. / cm^{-1}	Obs. / cm^{-1}	Error / cm^{-1}	Resid. / cm^{-1}
P	27	-8.6513	-8.6625	0.0143	-0.0112
P	25	-7.7837	-7.7920	0.0366	-0.0083
P	24	-7.3629	-7.3685	0.0112	-0.0056
P	23	-6.9506	-6.9408	0.0153	0.0099
P	22	-6.5471	-6.5700	0.0143	-0.0229
P	21	-6.1522	-6.1511	0.0162	0.0011
P	20	-5.7659	-5.7621	0.0095	0.0038
P	19	-5.3882	-5.3760	0.0236	0.0122
P	18	-5.0192	-5.0144	0.0182	0.0048
P	17	-4.6588	-4.6552	0.0093	0.0036
P	16	-4.3071	-4.3190	0.0117	-0.0119
P	15	-3.9640	-3.9573	0.0089	0.0066
P	14	-3.6295	-3.6413	0.0085	-0.0118
P	13	-3.3037	-3.3063	0.0175	-0.0026
Q	27	-3.1192	-3.1377	0.0203	-0.0195
P	12	-2.9865	-2.9703	0.0083	0.0162
P	11	-2.6780	-2.6800	0.0118	-0.0020
P	10	-2.3780	-2.3898	0.0095	-0.0117
Q	23	-2.2381	-2.2463	0.0193	-0.0082
P	9	-2.0868	-2.0814	0.0081	0.0054
P	8	-1.8041	-1.8034	0.0107	0.0007
Q	20	-1.6680	-1.6956	0.0141	-0.0276
P	7	-1.5301	-1.5399	0.0155	-0.0098
P	6	-1.2648	-1.2622	0.0186	0.0026
Q	16	-1.0288	-1.0174	0.0119	0.0114
P	4	-0.7600	-0.7671	0.0119	-0.0071
Q	13	-0.6401	-0.6384	0.0081	0.0017
Q	12	-0.5278	-0.5418	0.0133	-0.0140
R	0	0.3509	0.3662	0.0258	0.0154
R	1	0.5471	0.5527	0.0137	0.0056
R	2	0.7347	0.7349	0.0185	0.0001
R	3	0.9137	0.9218	0.0107	0.0081
R	4	1.0841	1.0818	0.0133	-0.0023
R	5	1.2458	1.2488	0.0154	0.0031
R	6	1.3988	1.4050	0.0124	0.0062
R	7	1.5432	1.5375	0.0069	-0.0057
R	8	1.6790	1.6854	0.0197	0.0064
R	9	1.8062	1.7956	0.0166	-0.0106
R	10	1.9247	1.9231	0.0129	-0.0016
R	11	2.0346	2.0408	0.0046	0.0062

Table 4.12 (cont.)

$^{65}Cu_2$: Rotationless Origin = 0.289 ± 0.003 cm^{-1}

Branch	J″	Calc. / cm^{-1}	Obs. / cm^{-1}	Error / cm^{-1}	Resid. / cm^{-1}
P	18	-4.7955	-4.7959	0.0089	-0.0004
P	17	-4.4408	-4.4332	0.0148	0.0076
P	16	-4.0945	-4.0840	0.0080	0.0105
P	13	-3.1068	-3.1040	0.0134	0.0028
P	11	-2.4909	-2.4911	0.0113	-0.0002
P	9	-1.9089	-1.9033	0.0218	0.0056
Q	21	-1.6753	-1.6903	0.0161	-0.0150
P	7	-1.3610	-1.3628	0.0173	-0.0018
R	1	0.6838	0.6685	0.0291	-0.0153
R	2	0.8685	0.8655	0.0096	-0.0030
R	3	1.0447	1.0413	0.0103	-0.0034
R	4	1.2124	1.2099	0.0270	-0.0024
R	5	1.3715	1.3663	0.0117	-0.0052
R	6	1.5222	1.5074	0.0189	-0.0148
R	7	1.6644	1.6735	0.0212	0.0091
R	8	1.7980	1.7924	0.0243	-0.0057
R	9	1.9232	1.9174	0.0181	-0.0058
R	10	2.0399	2.0411	0.0085	0.0013

Normalised constants derived from spectrum ($^{63}Cu_2$)

B'_0 = 0.10405 ± 0.00007 cm^{-1}

B''_0 = 0.10843 ± 0.00006 cm^{-1} (FSR = 0.100028 cm^{-1})

Chi-squared = 59.19 with 88 degrees of freedom

Reduced Chi-squared = 0.673

4.4.3 Simulation of Rotational Spectra

To simulate rotational spectra, the positions and relative intensities of rotational lines within a vibronic band must be calculated. The rotational line positions were calculated from known spectroscopic constants according to the equation [24],

$$\begin{aligned}\nu &= T'_e + \omega'_e (v' + 1/2) - \omega_e x_e' (v' + 1/2)^2 \\ &+ B'_v J' (J' + 1) - D'_v (J' (J' + 1))^2 \\ &- \omega''_e (v'' + 1/2) + \omega_e x_e'' (v'' + 1/2)^2 \\ &- B''_v J'' (J'' + 1) + D''_v (J'' (J'' + 1))^2 \end{aligned} \qquad -(1)$$

Due to the cold rotational temperatures, the quartic terms in J" (J') were ignored. The vibrational terms were included with the term value to give the rotationless transition energy and the line positions were calculated relative to this origin.

The relative intensities of rotational lines within a rovibronic band are governed by four factors [24]:

i) The wavelength dependent intensity of the excitation source

ii) The nuclear spin statistical weighting

iii) The intrinsic rotational line strengths

iv) The population distribution of molecules between the various rotational levels of the lower state

The rotationally resolved spectra of Cu_2 are very compact and the intensity of the excitation source can be treated as independent of wavelength over the range of the spectra. The relative intensity of a rotational line is then reduced to the product of the other three factors and can be described by the equation,

$$I_R = N^s_{J''} \; S_{J''J'} \; N_0 \, e^{-BJ''(J+1)/kT} \qquad -(2)$$

where,

I_R = relative intensity of the rotational transition between J" and J'

$N^s_{J''}$ = nuclear spin statistical weighting on rotational level J"

$S_{J''J'}$ = rotational line strength for the transition from J" to J'

$N_0 \, e^{-BJ''(J+1)/kT}$ = population of rotational level J"

Each of the three factors is readily calculated.

Nuclear Spin Statistical Weighting

The total wavefunction of a homonuclear diatomic molecule may be written as the product of four parts, the electronic-, vibrational-, rotational-, and nuclear-wavefunctions [24],

i.e.

$$\Psi = \psi_e \, \psi_r \, \psi_v \, \psi_n \qquad -(3)$$

The behaviour of the total wavefunction to the exchange of nuclei depends on the nuclear spin of the (identical) nuclei. If the nuclear spin is zero or an integral value, then the wavefunction obeys Bose-Einstein statistics and is symmetric to exchange of nuclei. Alternatively, if the nuclear spin is half-integral, then the wavefunction obeys Fermi-Dirac statistics and is antisymmetric to the exchange of nuclei. The vibrational part of the wavefunction is symmetric to the exchange of

nuclei and hence the overall symmetry of the wavefunction is determined by the product of the rotational, electronic, and nuclear-spin wavefunctions.

Restricting the discussion to Cu_2, the nuclear spin of both copper isotopes is 1.5 [25] and hence they are Fermions. The ground state of Cu_2 is $^1\Sigma_g^+$ symmetry with the consequence that the even rotational levels are symmetric to nuclear exchange and the odd rotational levels are antisymmetric. To obey Fermi-Dirac statistics, molecules possessing antisymmetric rotational wavefunctions (odd J) must have nuclei with symmetric nuclear spin wavefunctions and vice-versa. The number of molecules in the even rotational levels compared to the odd rotational levels will be weighted by the number of nuclei with odd nuclear spin wavefunctions to the number of nuclei with even nuclear spin wavefunctions. Since nuclear spin splittings are very small, each nuclear spin level has almost the same population and the number of nuclei with symmetric and antisymmetric wavefunctions is readily calculable from the degeneracies of the symmetric and antisymmetric nuclear spin levels.

The total nuclear spin angular momentum for Cu_2 can be calculated using a Clebsch-Jordan series as 3, 2, 1, 0 units. The wavefunctions for the states of 3 and 1 units are symmetric and those of 2 and 0 units are antisymmetric. Allowing for the (2I + 1) degeneracy of the states, there are 10 symmetric states to 6 antisymmetric ones. The net result is to weight the odd rotational levels 5 / 3 times the even rotational levels.

Rotational Line Strength

The strength of the individual rotational lines within a vibronic band may be calculated using the Hönl-London formulae appropriate to the change in angular momentum and the electronic state symmetries of the lower and upper states. The

line strength includes all terms dependent on either J" or J', except for the Boltzmann factor. Hence the degeneracy of the rotational level is included within the line strength.

The formulae for the line strengths of P, Q, and R branches for transition between electronic states where $\Delta\Lambda = 0, \pm 1$ are listed in reference [24] and these were applied in the simulation of the spectra.

Boltzmann Population

If the ensemble of molecules is in thermal equilibrium at a single temperature, then the proportion of molecules in a given excited rotational level relative to those in the lowest excited level can be described by the Boltzmann equation [24],

$$N_e / N_0 = (2J + 1)\ e^{-BJ(J+1)/kT} \qquad -(4)$$

Since the degeneracy factor, $(2J + 1)$ is included in the rotational line strength, only the exponential term is included in the calculation of line intensities. In simulating the spectra, thermal equilibrium was assumed and the temperature, T, was treated as a variable parameter which was adjusted to obtain the best fit between the simulated spectrum and the experimental data.

Computational Details

The spectral simulation program performed three functions. Firstly, the rotational line positions were calculated. Once the line positions had been calculated, a "stick" spectrum was generated by plotting at each rotational line position a line whose height was proportional to the product of the nuclear spin statistical weighting, the rotational line strength and the Boltzmann population of the ground state rotational level. The "stick" spectrum was converted to the simulated spectrum by

running a laser beam of finite bandwidth over the spectrum. The function of this convolution was to blend lines that experimentally were unresolvable but which were resolved in the "stick" spectrum. This was essential to simulate realistic intensities for bandheads where, experimentally, many rotational transitions were excited simultaneously and each contributed to the observed ion signal. In all the simulations performed the laser pulse was treated as Gaussian with a FWHM bandwidth of 0.04 cm^{-1}.

4.4.4 Extraction of Rotational Constants

The etalon fringe calibration spectrum and the spectra for the different isotopic combinations of copper dimer were recorded simultaneously and stored independently in the computer. The spectral intensity was stored sequentially in an array (See Section 2.6.3). Each element in the array was known as a "bin". Extraction of the rotational constants involved the following steps:

(1) Location of the bin numbers corresponding to the spectral peaks and etalon fringes.

(2) Conversion of the spectra stored as intensity against bin number to spectra of intensity against etalon fringe number. This was necessary as the constant frequency marker was provided by the fringes and not the bin number.

(3) Assignment of the lines in the spectrum.

(4) Extraction of the molecular constants by a linear least squares method.

The typical frequency step used in acquiring the spectra was approximately 0.0125 cm^{-1}. When examined this closely, the spectral peaks showed the intensity fluctuations expected from the nature of cluster generation and the instabilities in the lasers. To determine the best value for the location of the peak maximum, a

least squares cubic polynomial was fitted through the data and the position of the peak maximum and its uncertainty were extracted analytically from the least squares coefficients [26]. More details can be found in Appendix B. This method was used to locate the peak maxima for both the etalon calibration fringes and the experimental peaks.

The conversion of the spectrum in bin numbers to a spectrum in etalon fringe numbers was achieved simply by counting the number of etalon fringes between the first fringe and the spectral feature of interest. Linear interpolation between fringes yielded the fractional displacement. Thus the line positions were measured in free spectral ranges (FSR's). The FSR of the confocal etalon used to calibrate the spectrum was quoted as 0.1 cm^{-1}. Since it was not possible to simultaneously calibrate the etalon against known atomic lines, the FSR was kept as a variable and its value determined by normalisation of the calculated ground state constant of copper dimer to the value quoted in the literature [1]. Table B2 in Appendix B lists the values of the FSR obtained by applying this method to the various spectra examined in this work. The averaged value of the FSR was calculated to be 0.10008 ± 0.00060 cm^{-1}.

Assignment of the lines in the spectrum was most easily achieved by considering the R-branches of the spectra for the $^{63}Cu_2$ isotopic combination since the R-branch suffered no interference from the Q-branch and the homonuclear $^{63}Cu_2$ exhibited a modulation in line intensity between even and odd rotational levels which aided assignment. The absolute numbering was confirmed from combination differences [24],

$$R(J''-1) - P(J''+1) = 2B''(J''+2) \qquad -(5)$$

using the known value for B''_o and the good estimate of the free spectral range.

The molecular sample was rotationally cold and all the spectra involved transitions to v' = 0 or 1 in the respective upper states. Consequently, the data was fitted to expressions involving only B'_n and B''_o and any contributions from the centrifugal distortion coefficient were ignored. The spectra for all three isotopic combinations were recorded simultaneously and were fitted in one expression. The data to be fitted can be described by the following system of equations:

$$\begin{bmatrix} \nu_1 \\ . \\ . \\ . \\ \nu_n \end{bmatrix} = \begin{bmatrix} 1 & 0 & 0 & J'(J'+1) & J''(J''+1) \\ . & . & . & . & . \\ 0 & 1 & 0 & \rho_1^2 J'(J'+1) & \rho_1^2 J''(J''+1) \\ . & . & . & . & . \\ 0 & 0 & 1 & \rho_2^2 J'(J'+1) & \rho_2^2 J''(J''+1) \end{bmatrix} \begin{bmatrix} \nu_{oo}^{126} \\ \nu_{oo}^{128} \\ \nu_{oo}^{130} \\ B' \\ B'' \end{bmatrix}$$

where,

ν_n = frequency of the transition from J'' to J'

ρ_1 = ratio of the reduced masses of $^{63}Cu_2$ and $^{63}Cu^{65}Cu$

ρ_2 = ratio of the reduced masses of $^{63}Cu_2$ and $^{65}Cu_2$

ν_{00}^{126}= rotationless transition energy for $^{63}Cu_2$

ν_{00}^{128}= rotationless transition energy for $^{63}Cu^{65}Cu$

ν_{00}^{130}= rotationless transition energy for $^{65}Cu_2$

A least squares solution [27] of this system of equations yielded the spectral origins for all three isotopic combinations of the dimer and B' and B''. The absolute values

of the spectral rotationless origins are arbitrary, but the differences gave the isotope shifts. It must be noted that this system of equations is only an approximation to the true system since the formulae relating the rotational constant for one isotopic combination to that for another isotopic combination involve B_e rather than B_n (n = vibrational level). Strictly, the columns relating to B_n should have been replaced by two columns, one relating to B_e and one to α_e, for both the upper and lower states. However, the columns relating to B_e and α_e are nearly linearly dependent and produced instability in the method. It is shown in Appendix B that the magnitude of the error introduced on making this simplification is negligibly small.

4.4.5 Collision-Free Lifetimes of the Lower Excited Electronic States of Cu_2

It is possible to measure the lifetime of a molecular state by a time-resolved R2PI technique [28]. With this technique, a molecule is excited to a state below its ionisation potential by a pump laser. The power of the pump laser is maintained sufficiently low that multiphoton ionisation is negligible. After an experimentally chosen time delay, the sample is irradiated by a second laser to generate photoions. By monitoring the photoion signal as a function of the time delay between the two lasers, it is possible to measure the lifetime of the excited state.

Figures 4.13 a-c show the spectra obtained for the A-, B- and C-states by scanning the trigger to the probe laser with respect to the pump laser. The spectra were taken by setting the wavelength of the pump laser to a rotational head. The intracavity etalon was not used to narrow the dye laser output, and hence, many rotational lines were excited simultaneously. Since Cu_2 was studied within a fully expanded supersonic molecular beam, the lifetime measured is effectively the collision-free lifetime.

The collision-free lifetimes extracted from the spectra are listed in Table 4.14. The measured lifetimes are in agreement with published values [20]. The lifetime of the B-state is seen to be the shortest, in agreement with reference [19] and with the results of fluorescence emission studies which have found emission from the B-state to be the most intense [3]. The lifetime of the A-state is approximately three times longer than that of the B-state. However, both lifetimes are short compared to that of the C-state. The lifetimes of the different vibrational levels of the C-state are seen to agree within experimental error. There may be a shortening by $v' = 2$, but one can not be conclusive due to the large error bound. The lifetime for $v' = 2$ is subject to greater error because it was experimentally more difficult to take the spectrum due to the low Franck-Condon factor between it and $v'' = 0$ in the ground state. Attempts to access the level through a hot band were unsuccessful due to their low intensity in the cold sample. An attempt was also made to measure the lifetime of $v' = 3$ in the C-state via the 3-0 band of the C-X system. A spectrum was obtained that appeared qualitatively similar to those for the lower vibrational levels. However, the spectrum was of insufficient quality to yield a lifetime.

Figure 4.15 shows the curves fitted through the data after lifetimes had been extracted. The method of extraction of the collision-free lifetimes of the states will now be described.

Figure 4.13: Lifetime scans of the vibrationless origins of the A-, B- and C-states of Cu_2. The figure illustrates graphically the difference in the lifetime between the vibrationless levels of the three states.

Figure 4.13 : Lifetimes of the 0–0 Bands of the A–X, B–X and C–X systems of $^{63}Cu_2$

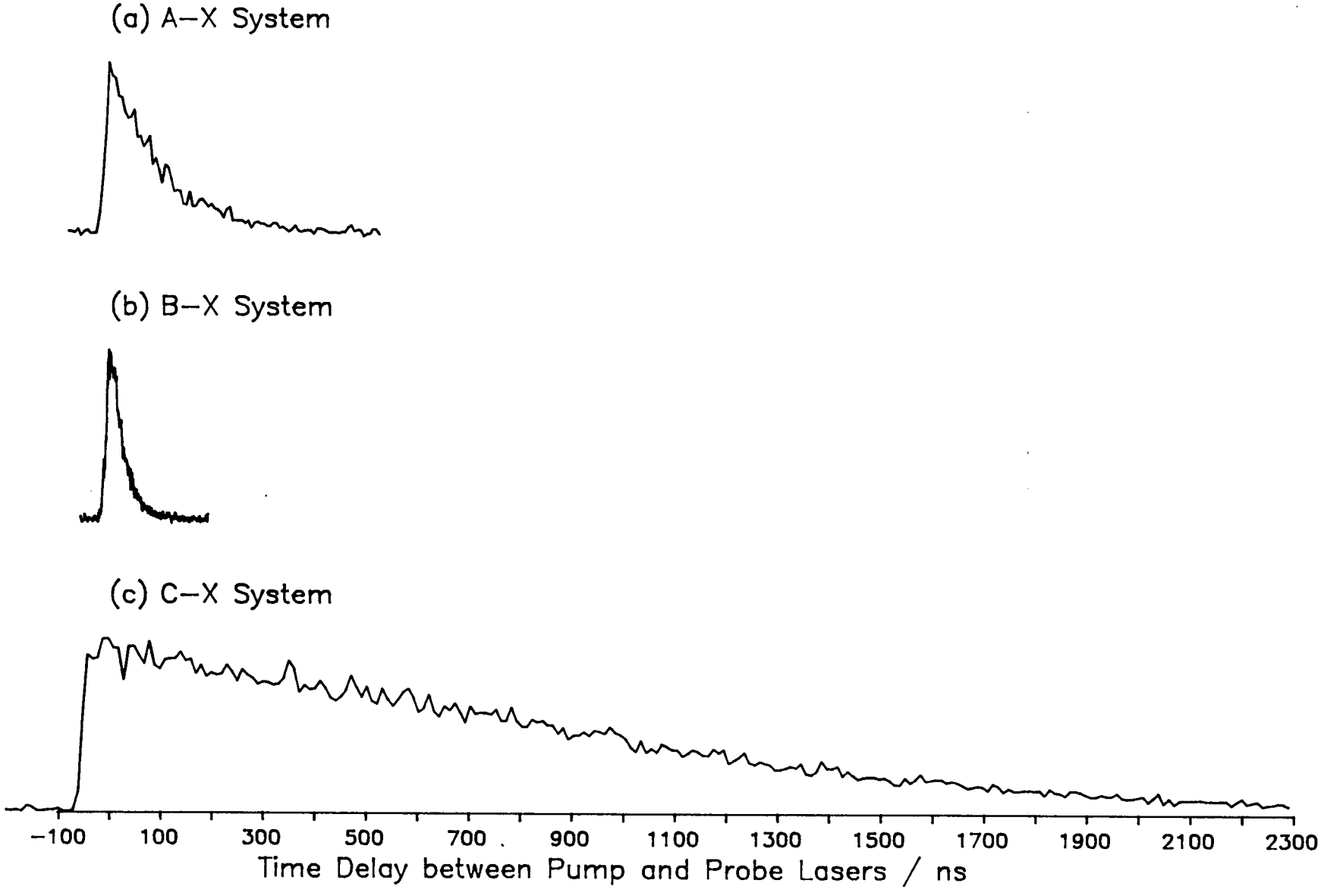

Table 4.14 : Collision-free lifetimes for selected vibrational levels of the A-, B- and C-states of Cu_2

STATE	v'	Lifetime / ns	Error / ns
A	0	105	5
B	0	32	2
B	2	26	4
C	0	746	27
C	1	783	50
C	2	682	96

Notes :

1) The errors quoted are derived purely from the numerical fit and take no account of the finite width of the laser pulses. They should be viewed as conservative estimates.

Figure 4.15 : Fitted curves to the lifetime data of the A-, B- and C-states of Cu_2. The figures display the experimental data points and curves generated from the least squares fit. To aid clarity, a symbol has been plotted for only every third data point in the case of the B-state. In the other two cases every data point is plotted. The line joining the flat baseline to the peak of the decay curve (i.e. the rising edge) was not fitted; it is merely a straight line joining the two portions of the curves.

Figure 4.15 : Fitted Lifetime Data for the v' = 0 Levels of the A–, B– and C–States of $^{63}Cu_2$

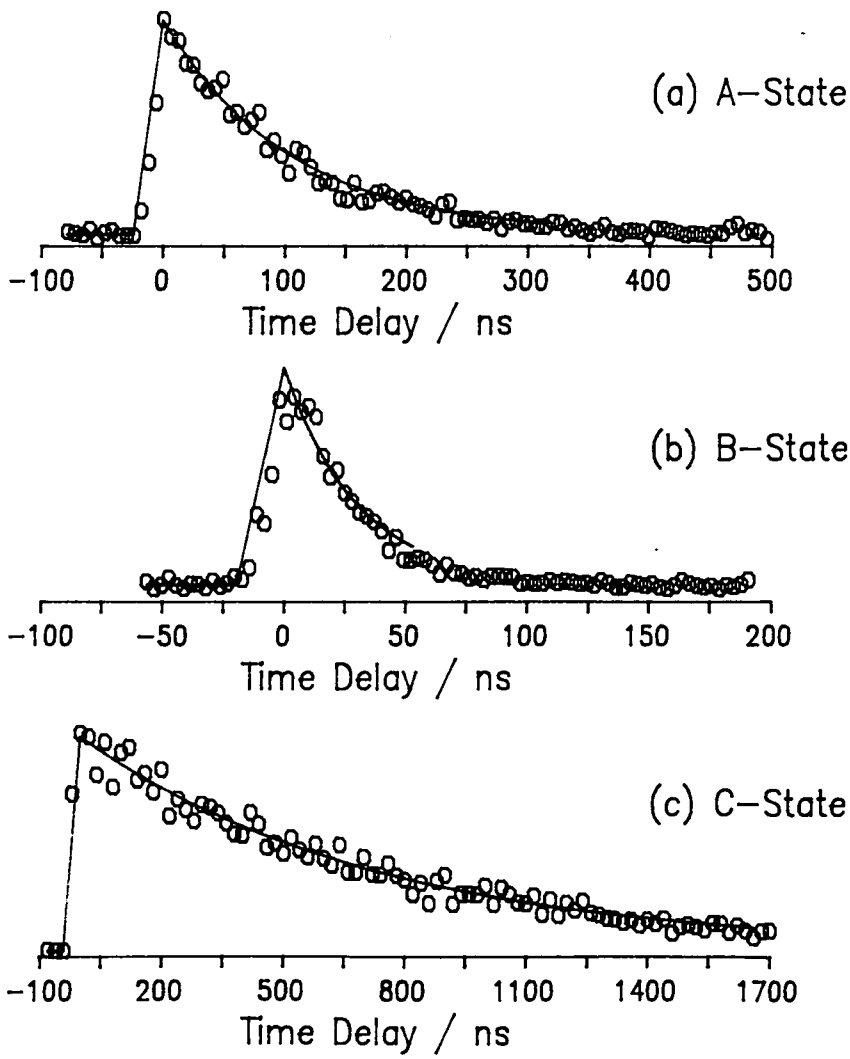

Extraction of Collision-Free Excited State Lifetimes

The experimentally observed ion signal can be described by the equation,

$$I_{exp}(t) = I_{nr}(t) + I_r(t) \qquad -(6)$$

where,

$I_{exp}(t)$ = time dependent experimentally observed ion signal

$I_{nr}(t)$ = non-resonant ion signal

$I_r(t)$ = resonantly enhanced ion signal

If one considers an ensemble of N molecules and a timescale with its origin when the pump and probe lasers are triggered simultaneously, equation (6) can be described by the equations,

$$I_{exp}(t) = K_{nr}\ N \quad (t < 0) \qquad -(7)$$

$$I_{exp}(t) = K_{nr}\ N_0 + K_r\ N_1 \quad (t > 0) \qquad -(8)$$

where,

K_{nr} = rate of non-resonant photoionisation

K_r = rate of resonantly-enhanced photoionisation

$N_0(t)$ = population of the ground state

$N_1(t)$ = population of the intermediate resonant state

If one further assumes that the excited state decays according to first-order kinetics, then the state populations for $t > 0$ are given by,

$$N_0(t) = N \ (1 - P_{exc} \ e^{-kt}) \qquad -(9)$$

$$N_1(t) = N \ P_{exc} \ e^{-kt} \qquad -(10)$$

where,

P_{exc} = proportion excited to the resonant intermediate state

k = first-order decay constant of the excited state

Substituting (9) and (10) into (8)

$$I_{exp}(t) = K_{nr} \ N + N \ P_{exc} \ (K_r - K_{nr}) \ e^{-kt} \qquad -(11)$$

A plot of ln ($I_{exp}(t)$ - K_{nr} N) against t will yield a straight line with a gradient of -k. The value of K_{nr} N can be determined from the ion signal recorded at negative times.

The above treatment implicitly assumes that the ion signal recorded at time t_i ($t > 0$) is due solely to molecules which were excited at time $t = 0$ and ionised at time $t = t_i$. This is an approximation since both laser pulses had finite widths. The extent to which the approximation holds depends on the lifetime of the excited state compared to the temporal widths of the laser pulses and can be estimated from the sharpness of the rising edge of the ion signal. With reference to figures 4.15 a-c, it is readily seen that the rising edges of the timescans of the C-state is effectively vertical whereas the rising edges of the A- and B-state spectra show distinct curvature due to the convolution of the laser pulses with the decay curve. To extract more accurate lifetime in such cases, the experimentally observed decay curves should be deconvoluted from the laser pulse. However, the quality of the experimental data did not merit any attempt at deconvolution, and

all the lifetimes reported in this work were obtained by plotting ln (I_{exp} - $K_{nr}N$) against t, for t > 0. The error bounds quoted in Table 4.14 are derived purely from the numerical method [27] used to analyse the data. They take no account of the finite widths of the laser pulses. They should therefore be treated as being rather conservative.

In extracting the lifetimes from the decay curves, the data were inspected for points which belonged to the flat baseline at the start of the curve, points which belonged to the rising edge and for points which were part of the true decay curve. Those points selected as belonging to the flat baseline were averaged. Those belonging to the rising edge were ignored and the origin of the decay curve, i.e. when there was no delay between the pump and probe lasers, was chosen by inspection to ensure none of the points belonging to the rising edge were included in the decay curve. Although the point chosen as the origin was not necessarily the true origin, the choice would not have affected the value of the lifetime extracted from the data.

4.4.6 Isotope Shifts of the Rotationless Origins

At a late stage in the thesis, McCaffrey *et al* [29] published a paper concerning the isotope shifts of the A- and B-states of Cu_2. They noted that the isotope shifts measured from their data differed from the values predicted from the known vibrational constants. The values of the isotope shifts extracted from the data in this work were re-examined. They were found to agree with the results from McCaffrey *et al.* This work was also able to furnish an isotope shift for the C-state.

Table 4.16 lists the isotope shifts in the rotationless origins extracted from the experimental data for various bands of the A-X, B-X and C-X systems. Also listed in the Table are the isotope shifts predicted from known vibrational constants.

It can be seen from Table 4.16 that whilst the discrepancies in the isotope shifts for the A- and B-states are approximately equal, the discrepancy in the isotope shift for the (0-0) band of the C-state is only approximately half of that in the A- and B-states.

Table 4.16A : Isotope shifts between $^{63}Cu_2$ and $^{63}Cu^{65}Cu$ for selected transitions from the ground state

STATE	v'	v"	Pred. / cm^{-1}	Obs. / cm^{-1}	Pred. - Obs. / cm^{-1}
A	0	0	-0.283	-0.216	-0.067
A	1	0	+1.191	+1.240	-0.049
B	0	0	-0.0894	-0.0205	-0.069
C	0	0	-0.177	-0.145	-0.032
C	1	0	+1.479	+1.518	-0.039

Notes :

1) The isotope shifts are defined as ν ($^{63}Cu_2$) - ν ($^{63}Cu^{65}Cu$)

Table 4.16B : Isotope shifts between $^{63}Cu_2$ and $^{65}Cu_2$ for selected transitions from the ground state

STATE	v'	v"	Pred. / cm^{-1}	Obs. / cm^{-1}	Pred. - Obs. / cm^{-1}
A	0	0	-0.568	-0.433	-0.135
B	0	0	-0.172	-0.0437	-0.128
C	0	0	-0.355	-0.288	-0.067

Notes :

1) The isotope shifts are defined as ν ($^{63}Cu_2$) - ν ($^{65}Cu_2$)

4.5 Conclusions

The R2PI studies on the A-X and B-X systems of Cu_2 have confirmed the assignments of the electronic symmetry of the B-state given by Aslund and the assignment of the electronic symmetry of the A-state given by Lochet. Both are of $^1\Sigma_u^+$ (0_u^+) symmetry and the uncertainty regarding the A-state assignment has thus been removed. The rotationally resolved spectrum of the C-X system has been shown to exhibit P, Q and R branches and hence the previously unknown electronic symmetry of the C-state can be assigned as Π_u (1_u).

The collision-free lifetimes of the lowest vibrational levels of the A-, B- and C-states have been measured by time resolved R2PI techniques. The lifetimes of the zero-point vibrational levels of the three states agree with previous experimental work and the lifetime data on the C-state has been extended to higher vibrational levels. The state lifetimes span a wide range from 32 ns for the B-state through 105 ns for the A-state and to 750 ns for the C-state.

The following chapter discusses the electronic structure of the low lying excited state of Cu_2 in the light of the experimental results on the electronic symmetries and lifetimes presented in this thesis and previous experimental and theoretical work.

REFERENCES

1. M.D. Morse, Chem. Rev., **86**, 1049 (1986)

2. J.O. Noell, M.D. Newton, P.J. Hay, R.L. Martin, and F.W. Bobrowicz, J. Chem. Phys., **73**, 2360 (1980)

3. B. Kleman and S. Lindkvist, Ark. Fys., **8**, 333 (1954)

4. J.C.R. Ruamps, Comptes. Rendus., **238**, 1489 (1954)

5. D.E. Powers, S.G. Hansen, M.E. Geusic, A.C. Puiu, J.B. Hopkins, T.G. Dietz, M.A. Duncan, P.R.R. Langridge-Smith, and R.E. Smalley, J. Phys. Chem., **86**, 2556 (1982)

6. V.E. Bondybey and J.H. English, J. Phys. Chem., **87**, 4647 (1983)

7. S.S.S. Rao and S.V.K. Rao, Indian J. Pure Appl. Phys., **16**, 923 (1978)

8. V.E. Bondybey, J. Chem. Phys., **77** 3771 (1982)

9. D.E. Powers, S.G. Hansen, M.E. Geusic, D.L. Michalopoulos, and R.E. Smalley, J. Chem. Phys., **78**, 2866 (1983)

10. E.A. Rohlfing and J.J Valentini, J. Chem. Phys., **84**, 6560 (1986)

11. N. Aslund, R.F. Barrow, W.G. Richards, and D.N. Travis, Ark. Fys., **30**, 4171 (1965)

12. D.S. Pesic and S. Weniger, Comptes. Rendus. Ser. B, **273**, 602 (1971)

13. J. Lochet, J. Phys. **B**, **11**, L55 (1978)

14. N.L. Singh, Phys. Rev., **99**, 1624 (1955)

15. D.R. Preuss, S.A. Pace, and J.L Gole, J. Chem. Phys., **71**, 3553 (1979)

16. J.L Gole, J.H. English, and V.E. Bondybey, J. Phys. Chem., **86**, 2560 (1982)

17. G.A. Ozin, S.A. Mitchell, and J. Garcia-Prieto, J. Phys. Chem., **86**, 473 (1982)

18. H. Wiggenhauser, D.M. Kolb, H.H. Rotermund, W. Schrittenlacher, and W. Schroder, Chem. Phys. Lett., **122**, 71 (1985)

19. R.E. Steele, J. Mol. Spectrosc. **61**, 477 (1976)

20. V.E. Bondybey, G.P. Schwartz, and J.H. English, J. Chem. Phys., **78**, 11 (1983)

21. Lambda Physik, FL3001/2 Instruction Manual, Gottingen, FRG (1986)

22. D.H. Levy, Ann. Rev. Phys. Chem., **31**, 197 (1980)

23. J.F. Ready, *Effects of High Power Laser Radiation*, Academic Press (1971)

24. G. Herzberg, *Molecular Spectra and Molecular Structure I. Spectra of Diatomic Molecules*, Van Nostrand Reinhold, New York (1950)

25. J.A. Salthouse and M.J. Ware, *Point Group Character Tables and Related Data*, Cambridge University Press (1972)

26. A. Savitzsky and M.J.E. Golay, Anal. Chem., **36**, 1627 (1964)

27. P.R. Bevington, *Data Reduction and Error Analysis for the Physical Sciences*, McGraw-Hill, (1969)

28. M.A. Duncan, T.G. Dietz, M.G. Liverman, and R.E. Smalley, J. Phys. Chem., **85**, 7 (1981)

29. J.G. McCaffrey, R.R. Bennett, M.D. Morse, and W.H. Breckenridge, J. Chem. Phys., **91**, 92 (1989)

CHAPTER FIVE

The Electronic Structure of the Lower Electronic States of Copper Dimer

5.1 Introduction

The data on the lower excited states of Cu_2 is neither complete nor self-consistent. There is evidence for the predissociation of the A- and B-states in matrix work and some evidence for gas-phase predissociation. However, strong emission has been observed from many vibrational levels of these upper states, suggesting that fluorescence competes efficiently against any predissociation.

The relationship between the A-, B-, C- and D-states is not obvious. The lifetimes of the states span a range from approximately 30 ns to greater than 6.5 μs. The short lifetimes of the A- and B-states with respect to the C- and D-states could be indicative of either predissociation of the former two states or of fundamental differences in electronic structure between the A- and B-states, and the C- and D-states.

This chapter attempts to find an explanation for the observed energetic ordering of the excited molecular states, for their symmetries and for their lifetimes. In attempting to account for the properties of the low-lying excited states of copper dimer, one must know the number and types of the molecular states derivable from the appropriate atomic limits. The following section discusses the atomic structure of Cu.

5.2 Atomic Structure of Copper

The ground state of the copper atom has the electronic configuration $[Ar]3d^{10}4s^1$, where [Ar] corresponds to the electronic configuration of an argon atom, $1s^2 2s^2 3s^2 2p^6 3p^6$. This configuration yields one atomic term, ^2S. Excitation of a single 3d electron to the 4s orbital yields the first excited term, ^2D, with electronic configuration $[Ar]3d^9 4s^2$. Spin-orbit coupling in the ^2D term is quite large with the $^2D_{3/2}$ state lying 2,043 cm^{-1} above the $^2D_{5/2}$ state. The $^2D_{5/2}$ state lies 11,202 cm^{-1} above the $^2S_{1/2}$ ground state [1].

The next higher term is the $^2P^o$ arising from excitation of the 4s electron to a 4p orbital. The corresponding electronic configuration is $[Ar]3d^{10}4p^1$. This term suffers a relatively small spin-orbit splitting (248 cm^{-1}) with the lower energy component, $^2P^o_{1/2}$ lying 30,535 cm^{-1} above the ground state. Several quartet states lie a further 9,000 cm^{-1} higher in energy.

The dissociation energy of copper dimer in its ground state has been measured as 16,760 cm^{-1} [2]. On a molecular energy scale, (measuring energies relative to T_e of the molecular ground state) the ^2D atomic states lie between 28,000 - 30,000 cm^{-1} and the $^2P^o$ states lie at approximately 47,500 cm^{-1}.

The term values of the atomic states up to and including the $^2P^o$ term and those of the A-, B-, C-, D- and E-states are shown in Figure 5.1. The energy scale on the figure is referenced to the T_e value for the ground state of Cu_2.

Figure 5.1: Lowest lying electronic states of Cu and Cu_2

Figure 5.1 : Schematic Energy Level Diagram for the Lowest Electronic States of Cu and Cu_2

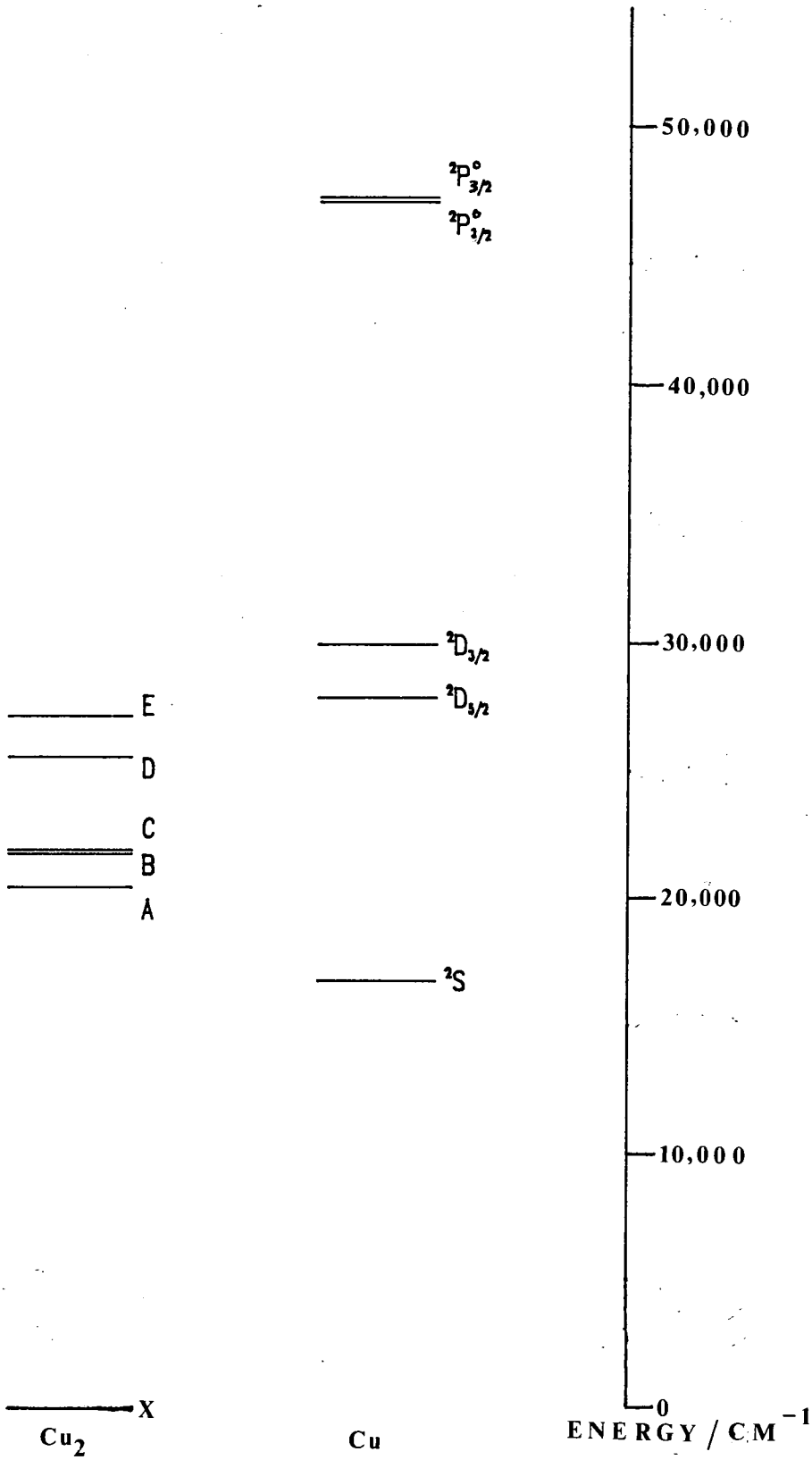

5.3 Correlation to the First Excited Atomic Limit, $^2S + {}^2D$

With reference to Figure 5.1, it can be seen that, on energetic grounds, the A-, B-, C-, D- and E-states of the dimer could all correlate to an asymptotic limit consisting of one ground state atom (^2S) and one excited state atom (^2D). A reasonable starting point is to limit discussion of the nature of the excited molecular states of copper dimer to those states correlating to the first excited atomic limit ($^2S + {}^2D$). These states can be considered as the " basis set " of pure molecular states from which the real states derive their principal characteristics. Although a highly approximate method, it is justified by extreme difficulty in obtaining good theoretical calculations on transition metal dimers, especially in excited electronic configurations.

The $^2S + {}^2D$ limit can give rise to three types of states, Σ^+, Π and Δ, each of which can exist as singlet or triplet, and gerade or ungerade [3]. In total, there are twelve molecular states which correlate to this limit. Only those states optically accessible via one photon transitions from the $^1\Sigma_g^+$ ground state, i.e. only the ungerade states, need be considered further. The electronic configurations corresponding to these states are listed in Table 5.2.

A satisfactory description of the electronic structure of the low-lying excited states of Cu_2 must meet certain criteria. It must qualitatively account for the number of states of each electronic symmetry and for their energetic ordering. It must also provide qualitative agreement with the observed relative transition strengths, and account for the observed vibrational frequencies and equilibrium bondlengths.

Table 5.2 : Electronic configurations of the one-photon accessible molecular states of Cu_2 derived from the $^2S + {}^2D$ atomic limit

State	Configuration
$^{1,3}\Sigma_u^+$	$[3d\sigma_g]^1 \ldots [4s\sigma_u^*]^1$
$^{1,3}\Pi_u$	$[3d\pi_g]^3 \ldots [4s\sigma_u^*]^1$
$^{1,3}\Delta_u$	$[3d\delta_g]^3 \ldots [4s\sigma_u^*]^1$

Note :

1) All molecular orbitals up to and including the $4s\sigma_u^*$ orbital that are not explicitly listed are completely filled.

It is possible to derive enough states of the correct symmetry from the first excited atomic limit. However, in order to account for the observed transitions, it is not possible to treat the excited states in Hund's case (a) [3] coupling scheme with the assumption that the spin-selection rule, $\Delta S = 0$, is strongly obeyed. The presence of two 0_u^+ states can only be accounted for by assigning one state as the $^1\Sigma_u^+$ state and one as the 0_u^+ component of the $^3\Pi_u$ state. The C-, D- and E-states would then have to be assigned as either the $^1\Pi_u$ state or 1_u components from either the $^3\Pi_u$, $^3\Delta_u$ or $^3\Sigma_u^+$ states. As suggested from the lifetime data in this study and supported by the previous time-resolved fluorescence emission studies [4] [5], the B-X transition carries most of the oscillator strength. Therefore, it is reasonable to assume that, in this model, it should be assigned as the fully allowed transition to $^1\Sigma_u^+$ state, forcing the A-state to be assigned to the $^3\Pi_{0u}^+$ state.

To proceed further with the description of the states, three reasonable assumptions must be made :

1) The bonding due to the molecular orbitals derived from the 3d-orbitals on the copper atoms is negligible compared to that from the molecular orbitals derived from the atomic 4s-orbitals.

2) The strength of bonding due to the molecular orbitals, as expected from elementary overlap considerations, decreases in the order, $\sigma > \pi > \delta$

3) The energy associated with electronic restructuring when an electron is promoted from a 3d-based molecular orbital to the $4s\sigma_u^*$ orbital is independent of the symmetry of the d-based molecular orbital.

With these assumptions, it is possible to qualitatively rank the molecular states according to energy. This is shown in Figure 5.3.

Figure 5.3 : Schematic energy level diagram for the ungerade electronic excited states of copper dimer correlating to the $^2S + {}^2D$ atomic limit. Within each manifold the order is predicted from the three assumptions listed previously in the text. The relative spacing of the triplet and singlet manifolds, determined by the electron exchange energy, is schematic.

Figure 5.3 : Schematic Energy Level Diagram for the ungerade states of Cu_2 correlating to $^2S + ^2D$

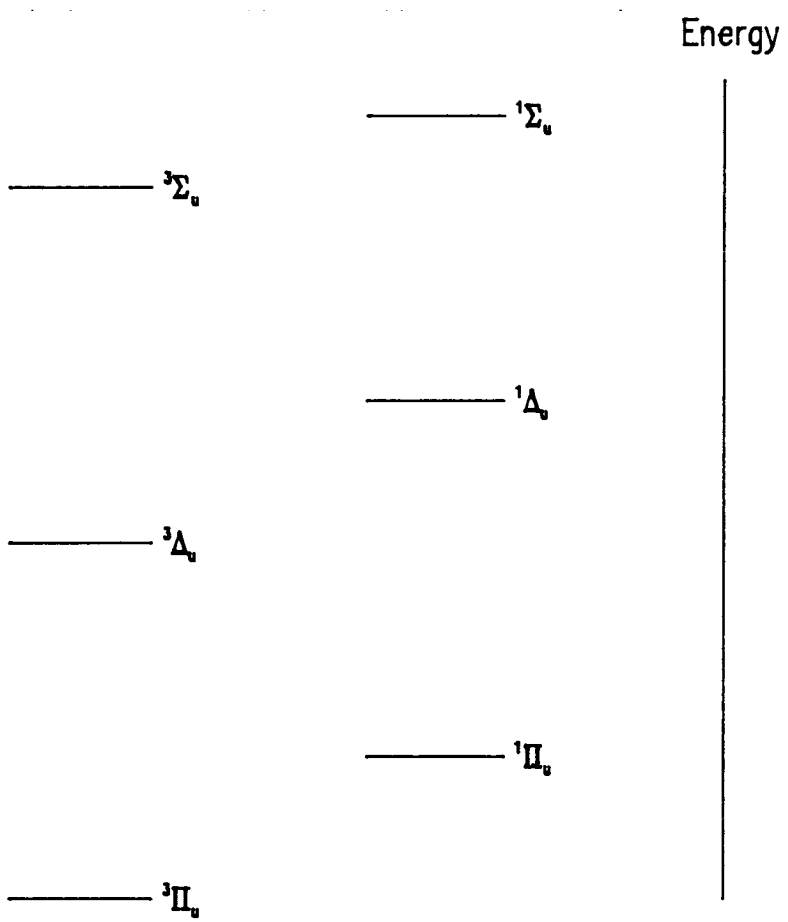

From Figure 5.3, it can be seen that the lowest 1_u state is the 1_u component from the $^3\Pi_u$ state. Within the triplet manifold , the $^3\Sigma_u^+$ state lies at highest energy and the $^3\Delta_u$ state lies between the $^3\Pi_u$ and $^3\Sigma_u^+$ states. The only other 1_u state is the $^1\Pi_u$ state itself. This state is known to lie higher than the $^3\Pi_u$ state, due to the exchange energy of the latter [6]. Whether it lies above or below the $^3\Delta_u$ and $^3\Sigma_u^+$ states depends on the relative magnitudes of the exchange energy and the energy separation between the states within the triplet manifold.

The $^3\Pi_u$ state arising from the $^2S + ^2D$ atomic limit is an inverted multiplet [3], meaning that the component with zero angular momentum lies at highest energy. Therefore the 1_u component of the $^3\Pi_u$ state will lie below the A-state and the assignments given to the C-, D- and E-states can therefore be limited to the $^1\Pi_u$ state and the 1_u components from the $^3\Delta_u$ and $^3\Sigma_u^+$ states.

On comparing the observed energetic ordering of the states to the predicted order based on the assignments of the A- and B- states given previously, it is seen that agreement is poor. The B-state, which is known experimentally to lie below the C-, D-, and E-states, is assigned to the state of highest energy. The lifetime data is even more conflicting. The lifetimes of the A- and C-states are markedly different and it is difficult to reconcile a shorter lifetime, ignoring predissociation, applying to the $^3\Pi_{0u}^+$ state than to the $^1\Pi_u$ state. Therefore, the C-state would have to be assigned to the 1_u component of a triplet state. The D-state, which has an even longer lifetime than that of the C-state, would then have to be assigned to the 1_u component of the remaining triplet state. By default, the E-state, for which no lifetime data exists, would have to be assigned as the $^1\Pi_u$ state. However, this still leaves unexplained the fact that three states that are formally components of the triplet states exhibit lifetimes ranging from 100 ns through 750 ns to greater than 6.5 μs.

Even arguing that the D-X and E-X transitions have not been definitively assigned to Cu_2, the discrepancy between the lifetimes of the A- and C-states still remains and the energy of the B-state is still low with respect to the other states. The state assignments possible using this simplistic model provide a poor description of the observed spectroscopic data.

The failings of the model can be broken down into two separate factors. Firstly, the three assumptions on which the predicted energetic ordering of the states was based may be invalid. Secondly, the model itself may be too simple and the assumption that the states can be considered as derived purely from the $^2S + {}^2D$ atomic limit could be invalid due to the intrusion of states from higher asymptotic limits. To address these factors requires recourse to theoretical calculations.

Most of the theoretical work on copper dimer has concentrated on the ground state [7-15]. The bonding has been shown to be predominantly through 4s orbital interactions, with the 3d orbitals remaining essentially atomic in nature [9] [12-15]. The 3d-electrons do play a significant role in determining the bond-dissociation energy through increased correlation in the molecule with respect to the atom. The correlation energy increases the depth of the potential well with respect to the value calculated by assuming that the 3d electrons are frozen in the atomic cores. For example, Dixon and Robertson [7] calculated a dissociation energy which was only 45 % of the experimental value when the d-electrons were treated as a frozen core, but which rose to 85 % of the experimental value upon relaxing the d-electrons.

Several sets of calculations have tackled the ordering of the molecular orbitals in the ground state of copper dimer [14-15] [17-18]. Although the absolute energies vary from one calculation to another, a clear and consistent pattern emerges as to the ordering of the molecular energy levels: this is shown in Figure 5.4. In order

of decreasing energy, one finds first the $4s\sigma_g$ bonding orbital, and lying a further 5 eV lower in energy the 'non-bonding' band of 3d-electrons, which is approximately 1 eV in width. The energetic ordering of the orbitals within the d-band is as expected from basic atomic overlap considerations. Therefore, there appears to be strong theoretical support for the first and second assumptions used in the simple model describing the electronic structure of the excited states, at least if bonding nature and ordering of the orbitals for the ground state can be transferred to the excited state. It thus appears valid to treat the 3d electrons as essentially non-bonding.

Figure 5.4: Molecular orbital energies of the ground state of Cu_2 calculated by *ab initio* methods.

Figure 5.4 : Molecular Orbital Energies of the Cu_2 Ground State

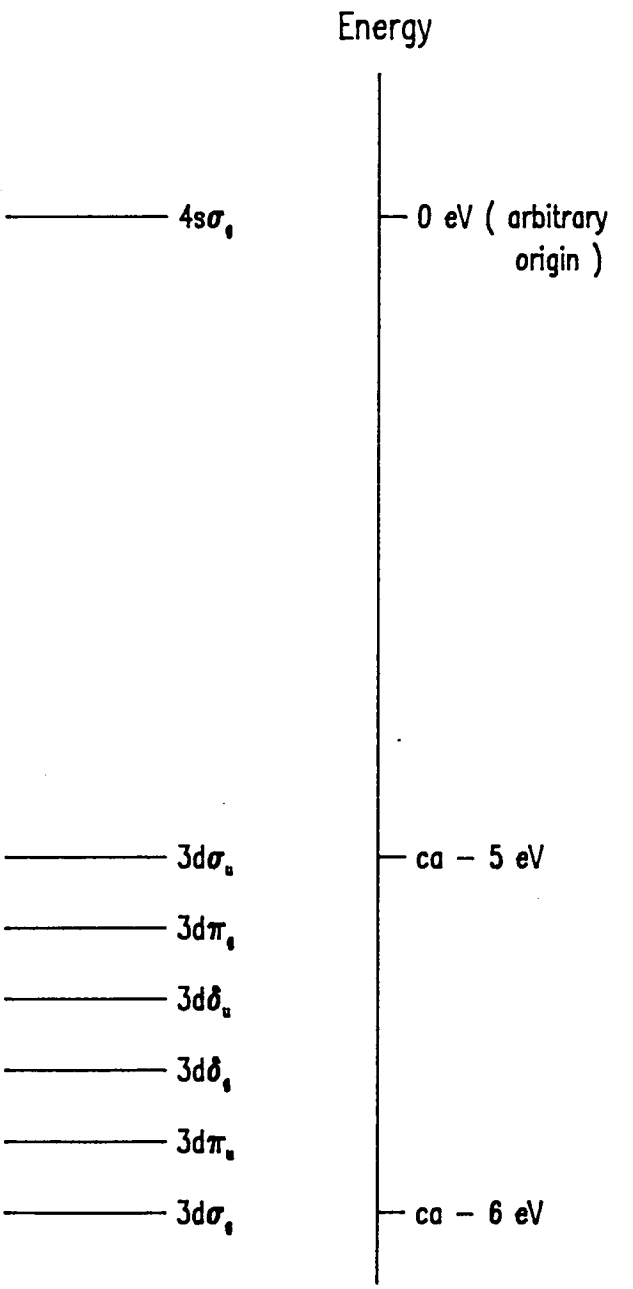

The third assumption in the model regards the degree of electronic reorganisation of orbitals not directly involved in the transition. Miyoshi *et al* [19] have calculated the extent of reorganisation upon ionisation of Cu_2. They obtained a value of 0.4 eV for removal of a 4s electron and a value of 5.7 - 6.2 eV for removal of a 3d electron. They argued that d-electron ionisation resulted in a high degree of electronic reorganisation because the d-orbitals should be thought of as localised on individual atoms. The creation of a hole on either atom would then result in significant d-level reconstruction. With regard to electronic transitions, the absolute magnitude of d-electron relaxation energy is not important. Rather, the important factor is whether the energy remains constant regardless of the orbital from which the electron has been promoted. Perhaps the most useful calculations that provide data on which to test this assumption are those of Witko and Beckmann [17]. These authors carried out *ab initio* multi-reference double excitation configuration-interaction (MRD CI) calculations on the ground and excited states of copper dimer. They calculated the adiabatic transition energies for the promotion of an electron from a 3d-based orbital to the $4s\sigma_u^*$ molecular orbital. They also listed the energies for the various molecular orbitals. A discrepancy in the energy gap between the molecular orbitals involved in the transition and the adiabatic transition energy would indicate that some electronic restructuring had accompanied the transition. If the relaxation energy is defined by,

Relaxation Energy = Adiabatic Transition Energy - Energy Gap Between Orbitals

then the relaxation energy measures the extent of electronic reorganisation associated with the transition. For transitions to triplet states, an "effective" relaxation energy can be defined by the above equation, differing from the normal relaxation energy by the inclusion of the core-valence exchange integral for the triplet state.

Table 5.5 : Relaxation energies accompanying electronic transitions from the d-based Molecular orbitals on Cu_2 to the $4s\sigma_u^*$ Orbital.

Orbital Vacated	Relaxation Energy / hartrees Singlet State	Triplet State
$3d\sigma_u$	-0.3422	-0.3624
$3d\pi_g$	-0.3484	-0.3808
$3d\delta_u$	-0.3463	-0.3584
$3d\delta_g$	-0.3469	-0.3539
$3d\pi_u$	-0.3618	-0.3342
$3d\sigma_g$		-0.3796

Notes :

1) The above values were calculated using the expression described in the text. Orbital and adiabatic transition energies were taken from [17].

2) 1 hartree = 2.19462×10^5 cm^{-1}

Table 5.5 lists the relaxation energy for the promotion of a single electron from a 3d derived molecular orbital into the $4s\sigma_u^*$ orbital. Energies for the formation of singlet and triplet states are quoted.

It can be seen that the relaxation energies for the transitions generating singlet states are consistent to approximately ± 700 cm^{-1}. Unfortunately, the energies for the triplet states are only consistent if given an order of magnitude more latitude. The authors do not quote the accuracy of their calculations and although the consistency between the relaxation energies for the singlet states is (probably) within their accuracy, the spread for the triplet states suggests that the assumption of equal relaxation energies is not necessarily valid.

In the light of this conclusion, the importance of the discrepancy between the experimental energetic ordering of the states and the order predicted, based on the three assumptions listed previously, should be relaxed.

The simplistic approach to the assignment of the lower excited states of Cu_2 as essentially pure states correlating with the $^2S + {}^2D$ limit, however, remains unsatisfactory because it cannot readily account for the observed lifetimes and the energetic ordering of the states. It is evident that a satisfactory description of these states will only be possible by considering the likelihood of 'intruder states' from higher atomic limits penetrating into the region of the A-, B- and C-states and mixing with them. The next section develops this theme.

5.4 Molecular States of Cu_2 Correlating to Higher Asymptotic Limits

5.4.1 $^2D + {}^2D$ Atomic Limit

This limit gives rise to 30 molecular states in Hund's case (a) coupling scheme. All the states possess the electronic configuration $[3d]^{18}(4s\sigma_g)^2(4s\sigma_u^*)^2$ i.e. the molecular orbitals derived primarily from the atomic 4s orbitals are completely filled. Any bonding in the molecule will therefore be through the d-shell and will be essentially negligible due to the highly contracted nature of the shell [20]. Since, even in Hund's case (c) coupling, only 12 out of the 59 states derived from the $^2D + {}^2D$ limit are optically accessible via one-photon transitions from the ground state, these states can be thought of as forming an essentially transparent, non-bonding band that has little effect on the spectroscopically accessible states lying below it.

5.4.2 $^2S + {}^2P^o$ Atomic Limit

The electronic configurations of the states of interest in one-photon transitions from the ground state which correlate to this atomic limit are listed in Table 5.6. The asymptotic limit lies at approximately 47,500 cm^{-1} on the molecular energy scale, suggesting that for the states to play a significant role in the spectroscopy of the lower excited states, they would have to be very strongly bound, with dissociation energies in the region of 25,000 - 30,000 cm^{-1}. This is almost double the binding energy of the ground state. The limited theoretical calculations available tend to suggest that transitions to the states derived from this limit lie at higher energy than the transitions to the A-, B- and C-states.

Table 5.6 : Electronic configurations of the one-photon accessible molecular states of Cu_2 correlating to the $^2S + ^2P^o$ atomic limit.

State	Configuration
$^{1,3}\Sigma_u^+$	$[4s\sigma_g]^1 \ldots [4p\sigma_u]^1$
$^{1,3}\Pi_u$	$[4s\sigma_g]^1 \ldots [4p\pi_u]^1$

Note :

1) All molecular orbitals up to and including those derived from the 3d atomic orbitals are filled. All other orbitals not explicitly listed are empty.

Hare *et al* [18] have performed an extended Hückel calculation on Cu_2 and predicted that electronic transitions to orbitals due to the 4p-4p interactions lie at considerably higher energy than the experimentally observed energy of the A-, B- and C-states. The authors suggested that mixing between the molecular orbital derived from the $4p_z$ atomic orbitals and the $4s\sigma_u^*$ orbital would serve to lower the energy of the latter.

Anderson [21], also using extended Hückel theory, has predicted the $3d\pi_g \rightarrow 4s\sigma_u^*$ transition to occur at 2.18 eV and the $3d\sigma_g \rightarrow 4s\sigma_u^*$ to occur at 2.85 eV. The lowest lying transition involving 4p orbitals occurred at 4.24 eV. This was the transition $4s\sigma_g \rightarrow 4p\pi_u$. The agreement between experiment and calculations is quite good for the lower excited states, though this may be due to the use of relatively accurate experimental data as part of the input required in this type of calculation. The validity of the calculations on the higher excited states must remain questionable due to the lack of correspondingly good experimental data on which to base the higher state energetics.

Ozin *et al* [22] have also performed calculations on molecular states derived from the $^2S + {}^2P^o$ atomic limit. They used the SCF-Xα-SW method and assigned the A-X transition to the promotion $3d\pi_g \rightarrow 4s\sigma_u^*$ and the B-X transition as $4s\sigma_g \rightarrow 4s\sigma_u^*$. The transitions from the 3d-orbitals or the $4s\sigma_g$ orbital to the $4p_\pi$ orbitals were calculated to occur between 260 - 220 nm. It must be noted, however, that the results of their calculations on the orbital energies are in disagreement with the more rigorous *ab initio* calculations and, in contrast to the *ab initio* work, the authors calculated the $4s\sigma_g$ orbital to lie below the $3d\pi_g$ and $3d\sigma_u$ orbitals.

The quality of the theoretical work on the molecular states of Cu_2 correlating to the $^2S + {}^2P^o$ limit is not high. The methods used are semi-empirical and are influenced by the experimental data input into the calculations. Hence, although

the studies tend to suggest that the states correlating to the $^2S + ^2P^o$ atomic limit lie at too high an energy to be considered in the assignment of the lower excited molecular states of Cu_2, this evidence must be treated with caution.

5.4.3 ^1S (Cu^+) + ^1S (Cu^-) Ion Pair Limit

The final limit which deserves inclusion amongst the set that should be considered as possible asymptotic limits for the low-lying excited states of Cu_2 is the ion pair limit Cu^+ (^1S) + Cu^- (^1S). This limit gives rise to two molecular states, one of $^1\Sigma_g^+$ symmetry and one of $^1\Sigma_u^+$ symmetry. Only the ungerade state need be considered since the gerade state will not interact with the ungerade states that are one-photon accessible from the ground state. This ionic limit lies at 69,166 cm^{-1} on the molecular energy scale, but due to the strong Coulombic attraction at large internuclear distance, the energy of the state drops to that of the $^2S + ^2P^o$ atomic limit when the ions are still 5.37 Å apart. It appears reasonable to treat the ion pair state as having an "effective" asymptotic limit at a considerably lower energy than its true value.

Many theoretical calculations have assigned the B-state as arising from the electronic promotion $4s\sigma_g \rightarrow 4s\sigma_u^*$ which formally correlates to the ion pair limit [7] [19] [22]. Miyoshi *et al* [19] calculated a transition energy of 2.4 eV for the electronic promotion $7\sigma_g$ (4s) $\rightarrow$ $7\sigma_u^*$ (4s) generating the singlet state and a transition energy of 4.07 eV for the promotion $3\pi_g$ (3d) $\rightarrow$ $7\sigma_u^*$ (4s) generating the triplet state. The first result is in good agreement with the experimental data and supports the assignment of either the A-X or B-X systems to the $7\sigma_g$ (4s) $\rightarrow$ $7\sigma_u^*$ (4s) transition. The second result, however, argues against the assignment of the remaining state (A or B) to the 0_u^+ component of the $^3\Pi_u$ state. However, the calculation was performed in $D_{\infty h}$ symmetry and the authors showed that if the hole in the d-orbitals was localised on one atom or the other, then under the lower

symmetry ($C_{\infty v}$), the transition energy for the promotion $3\pi_g$ (3d) → $7\sigma_u^*$ (4s) dropped to 2.4 eV, in much better agreement with experiment.

Witko and Beckmann's [17] calculations also support the hypothesis that the state corresponding to the $7\sigma_g$ (4s) → $7\sigma_u^*$ (4s) promotion lies at an energy close to the A-, B-, and C-states. They found the $4s\sigma_g$ → $4s\sigma_u^*$ transition had an adiabatic transition energy of 23,600 cm^{-1}, whilst the $^3\Pi_u$ state corresponding to the $3d\pi_g$ → $4s\sigma_u^*$ transition had an energy of 19,600 cm^{-1}. Although the calculated energies do not agree with the experimental ones, they are similar and the order matches that observed experimentally. It is significant that the authors quote the energy of the $^3\Sigma_u^+$ state correlating to the $^2S + {}^2D$ limit substantially higher at 27,150 cm^{-1}, which is very close to the reported transition to the E-state. Although they have not published the transition energy for excitation to the complementary $^1\Sigma_u^+$ state, one can expect it to lie at higher energy than its $^3\Sigma_u^+$ counterpart. The calculations thus support the argument against the $^1\Sigma_u^+$ state from the $^2S + {}^2D$ limit playing a major role in the A- or B-states.

Joyes and Leleyter [23] have also performed *ab initio* work on copper dimer. They found the $^1\Sigma_u^+$ state arising from the ion pair limit to lie approximately 6 eV above the ground state, considerably higher than the value calculated in other studies.

The remaining theoretical work on the ion pair state is semi-empirical in nature. Ozin's [22] SCF-Xα calculations lead him to suggest that the B-state arises from the electronic promotion $4s\sigma_g$ → $4s\sigma_u^*$, whereas Anderson's [21] extended-Hückel calculations suggested that the bonding → antibonding transition is dissociative in nature. The results from the theoretical work are therefore contradictory although the weight of evidence is in favour of the ion pair state, rather than one of the states from the $^2S + {}^2P^o$ atomic limit, playing a role in the spectroscopy of the low-lying excited states of Cu_2.

There is also circumstantial experimental evidence to support the presence of a deeply descending intruder state. In 1983, Powers *et al* [24] located five band systems of Cu_2 lying in the UV between 300 - 260 nm. One of the band systems, named system II in their nomenclature and subsequently renamed the G-X system [20], had a low vibrational frequency of only 116 cm^{-1} (compared to the ground state frequency of 266 cm^{-1}). This state was later studied in more detail by Rohlfing and Valentini [2] who monitored fluorescence emission. The latter authors noted that the state had a transition dipole moment that was strongly dependent on the internuclear separation, r, a feature that is characteristic of a state formed by an avoided crossing. The transition dipole moment was greater at larger separations and the authors suggested one possible avoided crossing could occur between a repulsive state from the $^2S + {}^2D$ asymptote and a strongly bound curve from the $^2S + {}^2P^o$ asymptote. In this case, the G-state has $^2S + {}^2D$ character at small internuclear separation and $^2S + {}^2P^o$ character at large internuclear separation, with the latter carrying much more oscillator strength to the ground state.

Figure 5.7 shows the potential curves for the lower excited electronic states of Cu_2.

At present, the origin of the intruder state which might be involved in an avoided crossing forming the G-state has not been investigated. The nature of the state formed by the avoided crossing may favour the suggestion that it is the $^1\Sigma_u^+$ state from the ion pair limit rather than a state from the $^2S + {}^2P^o$ limit that interacts with a state from the $^2S + {}^2D$ limit. Both the low vibrational frequency and large internuclear separation (2.73 Å) are characteristic of an ion pair state. The other state generated from the suspected avoided crossing which forms the G-state could descend further and intrude into the lower lying excited electronic states of Cu_2.

Figure 5.7 : Potential curves for the lower excited electronic states of Cu_2

Figure 5.7 : RKR Potential Energy Curves
for the X–, A–, B– and C–states of Cu_2

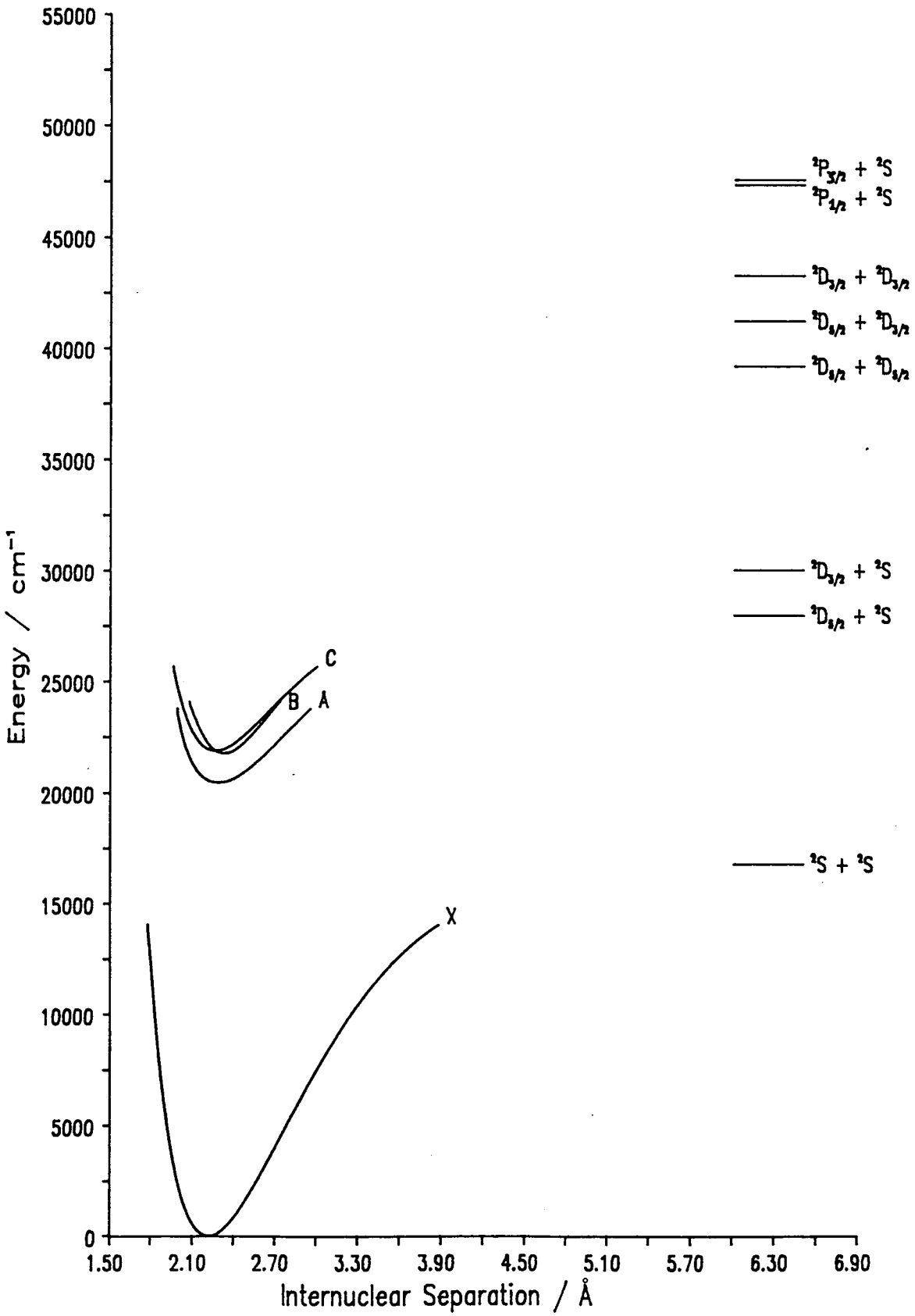

It remains to be answered whether the inclusion of an intruder state from a higher atomic asymptotic limit provides a better explanation of the experimental observations on the lower excited electronic states of Cu_2 than did the simple model presented earlier, which assumed the states correlated purely to the $^2S + {}^2D$ limit. The states correlating to the $^2S + {}^2P^o$ or ^1S (Cu^-) + ^1S (Cu^+) asymptotic limits are expected to carry more oscillator strength to the ground state than states correlating to the $^2S + {}^2D$ atomic limit. If the intruder state is from one of these two higher limits, then the effect of it mixing with states from the $^2S + {}^2D$ limit would be to increase their transition strength to the ground state. Since the B-X system carries the greatest oscillator strength of the lowest excited states of Cu_2 [25], it is likely that it is the B-state that is most influenced by the intruder state. It is therefore believed that the symmetry of the intruder state is 0_u^+ . The A-state, which shares the same symmetry as the B-state would also pick up some character from the intruder state. The candidate states for the intruder state can therefore be limited to the $^1\Sigma_u^+$ and the $^3\Pi_{0u}^+$ states from the $^2S + {}^2P^o$ limit, or the $^1\Sigma_u^+$ from the ion pair limit. Whilst both $^1\Sigma_u^+$ states should be strongly radiatively coupled to the ground state, transitions from the ground state to the $^3\Pi_u$ state are formally forbidden. Intensity may be gained through spin-orbit coupling.

One hypothesis that may be proposed is that the A-state arises from the 0_u^+ component of the $^3\Pi_u$ state correlating to the $^2S + {}^2D$ atomic limit with a little character from the intruder state. The B-state would then arise mainly from the intruder state, and the C-state would be the $^1\Pi_u$ state correlating to the first excited atomic limit. The D-state would be a 1_u component of a triplet state correlating to the $^2S + {}^2D$ atomic limit. The E-state could then either be the 1_u component from the remaining triplet state or the $^1\Sigma_u^+$ state itself, with both states correlating to the first excited atomic limit. Since the E-state has been observed

in gas-phase emission, it is likely to be the singlet state since the triplet state would probably have a similar lifetime to the D-state and would not be readily observed in gas-phase emission.

If one uses the C-state as a model for a pure, unperturbed singlet molecular state arising from the $^2S + {}^2D$ limit and the D-state as a model for a triplet state, then the energetic ordering, lifetimes and equilibrium bondlengths of the states can be rationalised. The C-state has a relatively long lifetime which is to be expected since the atomic transition from which it derives its oscillator strength is strongly forbidden. It also has a longer equilibrium bondlength than the ground state, in keeping with the assumed electronic promotion of a non-bonding / weakly antibonding electron to a strongly antibonding orbital. The D-state has an even longer lifetime than that of the C-state, in keeping with the spin forbidden nature of the transition.

The shorter lifetimes and longer equilibrium bondlengths of the A- and B-states compared to the C-state would then be due to the influence of the intruder state. Experimentally, properties of the A-state such as its equilibrium bondlength and its lifetime are seen to lie between those of the B- and C-states. This is expected, since it lies between the two extremes of a state correlating to the $^2S + {}^2D$ atomic limit and one correlating to a higher atomic limit. The mixing-in of character from the intruder state into the $^3\Pi_{0u}^+$ would therefore appear to lengthen the bond and shorten the lifetime with respect to the "pure" $^2S + {}^2D$ derived C-state.

The final experimental results that merit discussion are the observed photoprocesses such as predissociation and relaxation mechanisms within matrix cages. The $^3\Sigma_u^+$ state correlating to the lowest $^2S + {}^2S$ atomic asymptote is the only state that can induce predissociation. In Hund's case (c), this state splits into 1_u and 0_u^- components, and from symmetry considerations [3] only the first component

can predissociate 0_u^+ states. With reference to Figure 5.7, it is very hard to visualise a state which can simultaneously predissociate the lower vibrational levels of both the A- and B-states. Hence, Powers *et al* [26], who invoked predissociation of the B-state to explain its short lifetime, Bondybey *et al* [5] who suggested predissociation of the A-state to explain the marked vibrational dependence of its lifetime and Gole *et al* [27] who used predissociation of the C-state to explain the observation of a curtailed vibronic progression from the ground state cannot all have been correct.

The strongest evidence for gas-phase predissociation is that on the A-state. Although far from conclusive, it does attempt to pin down the $^3\Sigma_u^+$ state as having a perturbative effect on the low vibrational levels of A-state, though none was observed during these studies on the zero-point vibrational level. The suggestion that the shorter lifetime of the B-state compared to that of the C-state was evidence of predissociation is probably then due to an error in assuming that the B- and C-states were of the same origin. Similarly, the suggestion of predissociation of the C-state was made before its bondlength had been established. The low intensity of the vibronic bands from the zero point level in the ground state to $v' = 3$ or higher in the C-state are in fact due to poor Franck-Condon factors.

The matrix cage recombination data can also be addressed. Excitation of the A- and B-states isolated within a matrix provided strong evidence for predissociation of both states by the $^3\Sigma_u^+$ state. The observation of predissociation in both states in a matrix is more easily rationalised through the perturbations introduced by the matrix environment. Excitation of the D-state also yields emission from the B-state, emission from the $^3\Sigma_u^+$ state but none from the A-state. This suggests that the B-state is predissociated directly by the $^3\Sigma_u^+$ and not through the A-state and

that the A-state does not interact with the D-state. The non-interaction between the A- and D-states can be understood because the A- and B-states are of the same symmetry and would then not cross the D-state potential curve in the same region.

The hypothesis presented above appears to fit the experimental data. The exact origin of the intruder state remains unclear, however. The low vibrational frequency and large internuclear separation of the G-state can be taken as evidence that that the ion pair state undergoes an avoided crossing with one of the states from the $^2S + {}^2D$ atomic limit forming the G-state. The B-state could then be the other state generated from this avoided crossing. If this were the case, it would agree with the results of many calculations that assign the B-X transition as the promotion $4s\sigma_g \rightarrow 4s\sigma_u^*$. The electronic promotion is from a bonding to an antibonding orbital and this would account for the observed lengthening of the bond. However, the B-state has a high vibrational frequency and, although it has the longest bondlength of the lowest states of Cu_2, the bondlength is not significantly longer than that of the ground state. Neither observation is characteristic of a state derived from an ion pair limit.

The B-state could also be the 0_u^+ component of the $^3\Pi_u$ state correlating to the $^2S + {}^2P^o$ atomic limit. However, the spin-orbit splitting in the $^2P^o$ atomic state is quite small and it might be supposed that the molecular state would tend more to Hund's case (a) coupling. The B-X system would not then be expected to be as strong as is experimentally observed. The electronic promotion generating the $^3\Pi_u$ state also involves the promotion of a bonding electron to a different bonding orbital and one would intuitively expect the bondlength of the B-state derived from the $^3\Pi_u$ state to be shorter than that of the C-state, which is believed to be generated by the promotion of an electron from a non-bonding orbital to an

antibonding orbital. This is not observed experimentally.

A third possibility would be to assign the B-state to the $^1\Sigma_u^+$ state correlating to the $^2S + ^2P^o$ atomic limit. This would account for the observed bondlengths , as the electronic promotion is from a bonding to an antibonding orbital. However, it is difficult to justify the high dissociation energy required for the state to influence the low-lying excited states since it is generated from a bonding → antibonding transition.

The B-state probably takes some character from all three states and some from the $^1\Sigma_u^+$ state correlating to the $^2S + ^2D$ limit. The major contribution probably comes from the $^1\Sigma_u^+$ state correlating to the ion pair limit. Alternatively, states from even higher atomic limits may be responsible for the intruder state. Excitation of a 3d electron in the copper atom to the 4p orbital yields a group of atomic quartet states 9,000 cm^{-1} higher than the $^2P^o$ states, and a group of doublet states 4,000 cm^{-1} higher than the quartet states. Although these states are energetically further from the lower excited electronic states, theoretical calculations have suggested that if the d-hole present in these states was localised, then the state would be relaxed through greater molecular correlation energy. This may compensate for the higher asymptotic limit.

5.5 Conclusions

When the energetic ordering, transition strengths and lifetimes of the low-lying excited state of Cu_2 are considered together, simply assigning them as pure states correlating to the first excited atomic limit is unsatisfactory. Better agreement with experimental data is obtained if a state of 0_u^+ symmetry from a higher asymptotic limit is assumed to mix with the A- and B-states. The mixing is thought to occur predominantly with the latter. The prime candidate for the intruder state is the $^1\Sigma_u^+$ state correlating to the ion pair limit. The A- and B-states will ultimately dissociate to the first excited atomic limit, however, near to their potential minima, they may have more character from a different configuration.

The C- and D-states are thought to represent relatively pure singlet and triplet states correlating to the $^2S + {}^2D$ atomic limit, respectively. The greater lifetime of the D-state compared to the C-state may suggest that the spin selection rule, $\Delta S = 0$, is still quite valid and the molecule is not best described by Hund's case (c) coupling scheme.

To conclude this chapter, it must be reiterated that the state assignments presented are speculative though not, I believe, at odds with the experimental observations or with theoretical calculations. Clearly, much more work will be required, both theoretically and experimentally, before a full understanding of the electronic structure of the low-lying excited states of Cu_2 is acquired.

High quality calculations are required on the molecular states correlating to atomic limits above the $^2S + {}^2D$ limit to obtain a better picture of any that are deeply bound and could mix with the low-lying excited electronic states. As illustrated by the difficulties encountered in calculations on the ground state, correlation

effects between the 3d-electrons are important and are likely to become even more important with the excited states, many of which are formed by the promotion of an electron out of the 3d-based molecular orbitals thus opening up the d-shell.

More experimental data is also required to put the low-lying excited states into context. The electronic symmetry of the G-state should be determined. Since the G-X transition is a one-photon transition, the G-state is of either of 1_u or 0_u^+ symmetry. If it were found to be of 1_u symmetry then it could not be the resultant state from the avoided crossing between the ion pair state and a weakly bonding / non-bonding state from the $^2S + {}^2D$ atomic asymptotic limit. Finding it of 0_u^+ symmetry would only add circumstantial evidence to the hypothesis that the G-state is formed by an avoided crossing involving the ion pair state.

The longer lifetime of the C-state compared to the A- and B-states is thought to be indicative of a relatively small transition dipole moment between the ground state and a singlet state arising from the $^2S + {}^2D$ limit. It cannot be ruled out, however, that the longer lifetime is due to the C-state being a 1_u component of a triplet state. Determination of the state symmetries and gas-phase transition strengths to the D- and E-states from the ground state would help to clarify the position. The D-state is known to have a much longer lifetime than the C-state and if the transition coupling it to the ground state were shown to be typical of that for a triplet state correlating to the $^2S + {}^2D$ limit, then this would support the view that the C-state is a singlet state from this limit. The E-state was observed in gas phase emission and could possibly be the $^1\Sigma_u^+$ state from the $^2S + {}^2D$ limit, or it could be the other state generated by the avoided crossing thought to generate the G-state. If the latter were the case, then the B-state could not be the result of the same avoided crossing. Knowledge of the electronic symmetries of the D-, E- and G-states would help to clarify their relationship, if any, to the A-,

B- and C-states.

Similarly, more information on the higher electronic states (systems I - V) can only help elucidate which, if any, states are intruding into the lower states. These experiments are all to be performed and progress is being made in this laboratory.

Much remains uncertain about the electronic spectroscopy and structure of Cu_2. Opening the d-shell results in a large number of states in which electron correlation is important and spin-orbit couplings can be large. It is clear that we are a long way from theoretically understanding and experimentally characterising the effects of open d-shells on the electronic structure of molecules.

And to think, Cu_2 is probably the simplest transition metal cluster !

REFERENCES

1. C.E. Moore, Natl. Bur. Stand. Circ. 467 (1949)

2. E.A. Rohlfing, and J.J Valentini, J. Chem. Phys., **84**, 6560 (1986)

3. G. Herzberg, *Molecular Spectra and Molecular Structure I. Spectra of Diatomic Molecules*, Van Nostrand Reinhold, New York (1950)

4. R.E. Steele, J. Mol. Spectrosc., **61**, 477 (1976)

5. V.E. Bondybey, G.P. Schwartz, and J.H. English, J. Chem. Phys., **78**, 11 (1983)

6. J.N. Murrell, S.F.A. Kettle, and J.M. Tedder, *Valence Theory*, Wiley (1970)

7. R.N. Dixon and I.L. Robertson, Mol. Phys., **36**, 1099 (1978)

8. H. Tatewaki, E. Miyoshi, and T. Nakamura, J. Chem. Phys., **76**, 5073 (1982)

9. C.W. Bauschlicher, S.P. Walch, and P.E.M. Siegbahn, J. Chem. Phys., **78**, 3347 (1983)

10. H.J. Werner and R.L. Martin, Chem. Phys. Lett., **113**, 451 (1985)

11. K. Raghavachari, K.K. Sunil, and K.D. Jordan, J. Chem. Phys., **83**, 4633 (1985)

12. C.W. Bauschlicher, S.P. Walch, and P.E.M. Siegbahn, J. Chem. Phys., **76**, 6015 (1982)

13. C.W. Bauschlicher, Chem. Phys. Lett., **97**, 204 (1983)

14. H. Tatewaki, and S. Huzinaga, J. Chem. Phys., **72**, 399 (1970)

15. I. Shim and K.A. Gingerich, J. Chem. Phys., **79**, 2903 (1983)

16. M. Pelissier, J. Chem. Phys., **75**, 775 (1981)

17. M. Witko and H.O. Beckmann, Mol Phys., **47**, 945 (1982)

18. C.R. Hare, T.P. Sleight, W. Cooper, and G.A. Clarke, Inorg. Chem., **7**, 699 (1968)

19. E. Miyoshi, H. Tatewaki, and T. Nakamura, J. Chem. Phys., **78**, 815 (1983)

20. M.D. Morse, Chem. Rev., **86**, 1049 (1986)

21. A.B. Anderson, J. Chem. Phys., **68**, 1744 (1978)

22. G.A. Ozin, H. Huber, D. McIntosh, S. Mitchell, J.G. Norman, and L. Noodlemann, J. Am. Chem. Soc., **101**, 3504 (1979)

23. P. Joyes, and M. Leleyter, J. Phys. B, **6**, 150 (1973)

24. D.E. Powers, S.G. Hansen, M.E. Geusic, D.L. Michalopoulos, and R.E. Smalley, J. Chem. Phys., **78**, 2866 (1983)

25. B. Kleman and S. Lindkvist, Ark. Fys., **8**, 333 (1954)

26. D.E. Powers, S.G. Hansen, M.E. Geusic, A.C. Piui, J.B. Hopkins, T.G. Dietz, M.A. Duncan, P.R.R. Langridge-Smith, and R.E. Smalley, J. Chem. Phys., **86**, 2556 (1982)

27. J.L Gole, J.H. English, and V.E. Bondybey, J. Phys. Chem., **86**, 2560 (1982)

Appendix A : Simulation of Mass Spectral Peaks

a) Analytical

The method applied is similar to the described by Opsal [1]. The flight time of an ion of mass m in a TOFMS can be described by equation A.1,

$$T_1 = g\ (\ s_1,\ v_1,\ t_1\ ) \qquad \text{-(A.1)}$$

where,

T_1 = flight time of the ion

s_1 = initial position of the ion

v_1 = initial velocity component parallel to the TOFMS axis

t_1 = time of ionisation relative to the centre of the photoionisation pulse

If the probability of an ion occupying position s_1 with velocity v_1 and being ionised at time t_1 is known, then the probability of an ion having flight time T_1 can be calculated for that particular set of variables. However, there are many ways in which s, v and t can combine to give the same overall flight time T_1 and the total probability of an ion having flight time T_1 must be calculated by summing the contributions from all combinations of variables s, v and t which yield flight time T_1.

If the probability density functions (pdf's) of the three distributions, f_s (s), f_v (v) and f_t (t), are uncorrelated, then the probability that the ion will simultaneously take all three values is the product of the pdf's, that is,

$$P\ (\ s_1,\ v_1,\ t_1\ ) = f_s\ (s_1)\ f_v\ (v_1)\ f_t\ (t_1) \qquad \text{-(A.2)}$$

If the variables are altered by small amounts, Δs, Δv and Δt such that the flight time changes by a small amount, ΔT, then the probability, P, of an ion having a flight time between T_1 and ΔT is given by,

$$P = \int_{s1}^{s+\Delta s} f_s(s)\, ds \int_{v1}^{v+\Delta v} f_v(v)\, dv \int_{t1}^{t+\Delta t} f_t(t)\, dt \qquad -(A.3)$$

An approximation to ΔT can be obtained by expanding A.1 as a Taylor series,

$$T_1 + \Delta T = g\,(\,s_1,\, v_1,\, t_1\,) + \Delta s\, \partial g\,(s_1) / \partial s + \Delta v\, \partial g\,(v_1) / \partial v + \Delta t\, \partial g\,(t_1) / \partial t \qquad -(A.4)$$

that is,

$$\Delta T = \Delta s\, \partial g\,(s_1) / \partial s + \Delta v\, \partial g\,(v_1) / \partial v + \Delta t\, \partial g(t_1) / \partial t \qquad -(A.5)$$

The method for simulating the mass peaks makes use of equations A.3 and A.5.

The total ion intensity, I, at any flight time T_1, is given by,

$$I_{T1} = \int_{-\infty}^{\infty} \int_{-\infty}^{\infty} \int_{-\infty}^{\infty} f_s(s)\, f_v(v)\, f_t(t)\, ds\, dv\, dt \qquad -(A.6)$$

subject to the constraint that,

$$T_1 = g\,(\,s,\, v,\, t\,) \qquad -(A.7)$$

Computationally, the integrals were replaced by sums and the differential operators by a finite step size. It was also simpler to systematically scan through the variables, calculate the flight time and then put the probability for that flight time in an appropriate "box" than to attempt to weave a path through the variable space maintaining a constant flight time. It is the width of the box that determines the resolution to which a peak was simulated. At the start of the simulation, boxes were generated with widths ΔT and corresponding to the expected flight times of the ions. The process of simulation involved stepping

through all three variables s, v and t in small steps Δs, Δv and Δt respectively, such that the combined effect of all the changes on the flight time was less than $\Delta T / 2$. The probability of ions having flight times between T and $T \pm \Delta T / 2$ could then be calculated from the pdf's of the three distributions. This probability was then added to the box corresponding to the flight time T.

Each individual contribution to ΔT was assigned a ceiling value for the change it could induce in one step. The step size for the parameter was then calculated by dividing the differential term into the ceiling value. Calculation of the step size for the time of ionisation was the simplest since the differential multiplier is constant and equal to unity (that is, a 1 ns change in the time of ionisation will be mapped to a 1 ns change in the flight time). The temporal step size had need only to be be calculated once and because the step size was independent of the variables s and v, the probabilities for different times of ionisation also had only to be calculated once. They were then stored and reused. It is because of these properties that stepping through t occupied the inner loop of the algorithm.

The calculation of step size, Δs, made use of the Wiley and McLaren focusing condition. For a TOFMS focusing to a maximum, it is known that the absolute value of $\partial g(s) / \partial s$ approaches zero as s tends to s_0. Hence, if Δs was chosen so that s approached s_0, the small change in $\partial g / \partial s$ as s varies did not result in $\Delta s \times \partial g / \partial s$ becoming greater than its ceiling. By calculating $\partial g / \partial s$ at the point furthest from s_0, it was ensured that $\Delta s \times \partial g / \partial s$ never broke through its ceiling.

In calculating Δv, it should be noted that $\partial g / \partial v$ is approximately constant and that it can be shown numerically that when s is greater than s_0, the $\partial g / \partial v$ increases as v is scanned from negative to positive values and when s is less than s_0, $\partial g / \partial v$ decreases as v is scanned from negative to positive. The direction of scanning of v was therefore altered to suit the value of s and $\Delta v \times \partial g / \partial v$ could

be contained below its ceiling.

A little more must be said about the boxes into which the probabilities are added. The boxes were ΔT wide, and except in the unlikely case that the calculated flight time for the probability element lay exactly on the box axis, the element straddled two boxes. In these cases the probability element was approximated by a trapezium of width ΔT and with heights that were the products of the pdf's. The probability element was then split proportionally between the two adjacent boxes.

b) Monte Carlo Simulation of Mass Spectral Peaks

Generation of a Potential Map

The equilibrium electrical potential at a point in two dimensions is given by the Laplace equation [2],

$$\partial^2 V / \partial x^2 + \partial^2 V / \partial y^2 = 0 \qquad \text{-(A.8)}$$

where,

V = electrical potential at a point in (x, y) Cartesian space.

Equation A.8 is readily solved numerically by a relaxation technique with fixed boundary conditions [3]. Briefly, the area within the boundary was divided into small cells by a mesh of unit length and width. Each vertex of the cells was assigned an initial potential. The vertices were divided into two classes. The first class consisted of those points where the potential was held constant by some external influence. These were not relaxed. The second class consisted of those points which were not held constant and these points were relaxed.

For each relaxable point in turn, the potential at the point was compared to the potential calculated from the average of its four nearest neighbours. If the

potentials differed, the potential at the point was not fully relaxed and it was replaced by that calculated from its neighbours. Relaxation of each point in turn was repeated and eventually the potentials converged such that the potential at a particular point was equal to the average potential of its four nearest neighbours.

The number of iterations required depended on the latitude given to the equality between the potential at a point and that calculated from its neighbours and on the initial approximate potential. The potential maps generated in this work were taken to be fully relaxed when the difference between the potentials was less than 5 mV for all points. In general, between 200 - 800 relaxations of each point were required for convergence, the exact number depending on the quality of the initial potential.

Experimentally, and in the simulations, the boundary conditions were imposed by the copper box surrounding the TOFMS acceleration region and by the plates constituting the ion extraction optics. For the simulations the box was approximated as being fully closed and the apertures through which the molecular beam passed were ignored. The box was held at earth potential. The unit length of the mesh was 2 mm with the result that the area defined by the box was mapped with a 60 × 65 grid of points. The points lying on the copper box or along the plates of the ion extraction optics were not relaxed as external supplies maintained their potentials.

Calculation of Ion Trajectories

The potential within a cell of the mesh can be approximated by,

$$V = a_0 + a_1 x + a_2 y + a_3 xy \qquad \text{-(A.9)}$$

If two new Cartesian coordinates are defined such that,

$$\eta = (x + y) / \surd 2 \qquad \text{-(A.10)}$$

$$\xi = (x - y) / \surd 2 \qquad \text{-(A.11)}$$

then a separation of variables can be achieved and the potential can be described by,

$$V = b_0 + b_1\eta + b_2\xi + b_3 (\eta^2 - \xi^2) \qquad \text{-(A.12)}$$

The coefficients a_i can be obtained from the known potential at each of the vertices of the cell and the coefficients b_i can be related to them through equations A.10 and A.11. The equations of motion of an ion in the (η, ξ) coordinate system can therefore be established. The actual form of the equations depends on the sign and magnitude of b_3.

Following the trajectory of an ion involved using the equations of motion within a cell to calculate where the ion would leave a cell and enter an adjacent one. The equations of motion for the next cell were then derived and the ion tracked until it left that cell. This was repeated until the ion crossed-out from one of the cells at the boundary of the ion extraction optics.

Except in the case where b_3 was equal to zero, it was not possible to invert the equations of motion to make time a function of the coordinates. In the cases where inversion was not possible, a time step size was selected such that the ion would move through 0.1 of the cell if its velocity remained constant. After each step, the position of the ion was tested to see if it lay within the cell or if a wall had been breached. When the latter applied, the exact time at which the ion left the particular cell and the position at which it entered the adjacent cell was obtained using a Newton - Raphson [4] iterative method. The criterion for convergence of the iteration was that the calculated time to exit the cell differed

from the time calculated on the previous iteration by less than 0.1 ns. It was found to be computationally quicker to step through the cell in small steps than to take one large step and iterate backwards. In the case when b_3 was equal to zero or the cell was an equipotential plane, then the equations of motion could be inverted and the exact time and position of the ion leaving the cell could be calculated directly.

Simulation of Mass Spectral Peaks

The mass spectral peaks were generated by repeatedly calculating the trajectories and total flight times of ions for different initial distributions. As in the analytical case, boxes were set up to store the accumulating ion signal. Unlike the analytical case, however, there was no ambiguity over where to place the ion since it had a definite flight time and could be assigned to a specific box.

To obtain realistic mass spectral peaks, a random sample of all distributions had to be selected as trial trajectories. This was achieved through the use of NAG library routines for generating series of "random" numbers from specified distributions. In addition to the spatial, velocity and temporal distributions considered in the analytical case, a further variable was required to define the problem with relaxed electric potentials. Relaxation of the potentials meant that ions formed in the same plane parallel to the plates of the ion extraction optics did not necessarily occupy equipotential positions or that they would follow similar trajectories through the electric potential. This extra variable is referred to as the lateral distribution of the ions and is denoted by the symbol "l".

REFERENCES

1. R.B. Opsal, K.G. Owens, and J.P. Reilly, Anal. Chem., **57**, 1884 (1985)

2. W. Kaplan, *Advanced Mathematics for Engineers*, Addison-Wesley p431, (1981)

3. W. Kaplan, *Advanced Mathematics for Engineers*, Addison-Wesley p793, (1981)

4. E. Kreyszig, *Advanced Engineering Mathematics*, p765, Wiley (1979)

Appendix B : Extraction of Rotational Constants

(a) Peak Finding Routines

The method for locating the bin number of a spectral peak is a modification of that described by Savitzsky and Golay [1] and makes use of a moving origin across the data. The method requires data equally spaced along the abscissa. If one considers n-sequential data (where n is an odd number) to which the best possible cubic function is to be fitted, then the problem can be described as finding the best fit to the following system of equations

$$\begin{bmatrix} 1 & x_{-n/2} & x^2_{-n/2} & x^3_{-n/2} \\ . & . & . & . \\ . & . & . & . \\ . & . & . & . \\ 1 & x_{+n/2} & x^2_{+n/2} & x^3_{+n/2} \end{bmatrix} \begin{bmatrix} a_0 \\ a_1 \\ a_2 \\ a_3 \end{bmatrix} = \begin{bmatrix} y_{-n/2} \\ . \\ . \\ . \\ y_{+n/2} \end{bmatrix}$$

that is,

$$\mathbf{X\,a = y} \qquad \text{-(B.1)}$$

The best linear least squares solution is obtained by left-multiplying both sides of the equation by the transpose of $\mathbf{X}$, $\mathbf{X^T}$, and then solving the new system of equations,

$$\mathbf{X^T X\,a = X^T\,y} \qquad \text{-(B.2)}$$

Calling $\mathbf{A = X^T X}$, $\mathbf{b = X^T\,y}$, the best least squares solution can be obtained from the following equation

$$\mathbf{a} = A^{-1}\,\mathbf{b} \qquad -(B.3)$$

The numerical computation required in solving this set of equations can be greatly reduced by using a moving origin method. It is then necessary to calculate only once the matrices X, X^T, and A^{-1} and solution of the equations can be calculated by the computationally cheap multiplications of A^{-1} and X^T on to each new $\mathbf{y}$ vector.

The result of the least squares fit is to represent the data by a cubic polynomial of the form

$$y_n = a_0 + a_1 n + a_2 n^2 + a_3 n^3 \qquad -(B.4)$$

where n is the index of the data point relative to the moving origin. Differentiation of equation (B.4) yields

$$dy_n / dn = a_1 + 2a_2 n + 3a_3 n^2 \qquad -(B.5)$$

Equation (B.5) was solved to determine the value of n corresponding to a stationary point. If the modulus of n is less than 1, then the cubic polynomial had been fitted to the data with the moving origin located near to the stationary point. If, however, n was greater than 1 then a stationary point had been located at the peripheral of the data used to define the polynomial. Such a stationary point was ignored and the moving origin stepped on a further data point. Ignoring stationary points that were further from the moving origin than one step ensured

that the data points through which the polynomial was fitted were the ones which best defined the peak.

A further refinement implicit in the method is that the stationary point was located with the moving origin on both sides of it. The two, generally different values for the peak position were averaged.

The uncertainty in the peak position was calculated from the uncertainties in the coefficients a_1 to a_3 using the following equation:

$$\sigma_{sp} = (\partial y / \partial a_i)^T \; A^{-1} \qquad -(B.6)$$

(b) Approximate Least Squares

The least squares method used to extract rotational constants from the data approximated the relationships [2],

$$B_e^i = \rho^2 \; B_e \qquad -(B.7)$$

$$\alpha_e^i = \rho^3 \; \alpha_e \qquad -(B.8)$$

by the relationship,

$$B_n^i = \rho^2 \; B_n \qquad -(B.9)$$

where n is the vibrational quantum number.

The error introduced by this approximation is given by,

$$Err = 0.5 \; \rho^2 \; (1 - \rho) \; ((n' + 1) \; \alpha'_e \; J' \; (J' + 1) - (n'' + 1) \; \alpha''_e \; J'' \; (J'' + 1)) \qquad -(B.10)$$

Table B1 contains the results of calculation using equation (B.10) and realistic

parameters for Cu_2. It can be seen from the table that all the discrepancies are smaller than the experimental errors in the line positions and are unlikely to cause any error.

REFERENCES

1. A. Savitszsky and M.J.E. Golay, Anal. Chem., **36**, 1627 (1964)

2. G. Herzberg, *Molecular Spectra and Molecular Structure I. Spectra of Diatomic Molecules*

Table B1 : Errors in lines positions caused by the approximation in isotopic relationships

J″	R / cm^{-1}	P / cm^{-1}	Q / cm^{-1}
0	7.6×10^{-6}		
1	1.8×10^{-5}	-4.6×10^{-6}	3.0×10^{-6}
2	3.2×10^{-5}	-6.1×10^{-6}	9.1×10^{-6}
3	4.9×10^{-5}	-4.6×10^{-6}	1.8×10^{-5}
4	6.8×10^{-5}	0.0	3.0×10^{-5}
5	9.1×10^{-5}	7.6×10^{-6}	4.6×10^{-5}
10	2.5×10^{-4}	9.1×10^{-5}	1.7×10^{-4}
15	4.9×10^{-4}	2.5×10^{-4}	3.7×10^{-4}
20	8.0×10^{-4}	4.9×10^{-4}	6.4×10^{-4}
25	1.2×10^{-3}	8.0×10^{-4}	9.9×10^{-4}
30	1.7×10^{-3}	1.2×10^{-3}	1.4×10^{-3}

Notes :

1) The figures were calculated using equation (B.10) and the following values were used for the parameters :

$n'' = 0$; $n' = 0$

$\alpha_e'' = 6.0 \times 10^{-4}$ cm^{-1}

$\alpha_e' = 1.0 \times 10^{-3}$ cm^{-1}

$\rho^2 = 0.992276$

Table B2 : Value of monitor etalon free spectral range on normalising the ground state rotational constant to the literature value

STATE	v'	v"	FSR / cm^{-1}	Error / cm^{-1}
A	0	0	0.10002	0.00017
A	0	0	0.09965	0.00014
A	0	0	0.09964	0.00007
A	0	0	0.10153	0.00050
A	0	0	0.10125	0.00065
A	0	0	0.10024	0.00026
A	0	0	0.10028	0.00008
A	0	0	0.09984	0.00014
A	1	0	0.09985	0.00022
B	0	0	0.10036	0.00031
B	0	0	0.09953	0.00061
C	0	0	0.10008	0.00008
C	0	0	0.10003	0.00006
C	0	0	0.09926	0.00015
C	0	0	0.09986	0.00006
C	0	0	0.09990	0.00007
C	1	0	0.10004	0.00007

Free spectral range = 0.10008 ± 0.00060 cm^{-1}

Notes :

1) The figures listed in the table were calculated from the values required to normalise the ground state rotational constants extracted from the data in units of etalon free spectral ranges to the literature value in wavenumbers.

Appendix C

In accordance with the regulations of the Department of Chemistry, University of Edinburgh, I attended the the following lectures and courses during my period of study:

1. Mass Spectroscopy
2. Molecular Electronics
3. Micro Computing
4. Fortran 77
5. Signal Processing
6. Laser Physics
7. RKR Method
8. Least Squares Method
9. Theoretical Chemistry
10. Scientific German

In addition, all the regular departmental seminars and research group meetings were attended.

Conferences Attended

1. Faraday Division, High Resolution Spectroscopy Group, Reading, 1984
2. Faraday Division, High Resolution Spectroscopy Group, York, 1985
3. Scottish Quantum Chemistry Group, Dundee, 1985
4. Scottish Quantum Chemistry Group, Strathclyde, 1986
5. XIth International Symposium on Molecular Beams, Edinburgh, 1987